

2  $\mu\text{m}$  PULSED FIBER LASER SOURCES AND THEIR APPLICATION IN  
TERAHERTZ GENERATION

by  
Qiang Fang

---

Copyright © Qiang Fang 2012

A Dissertation Submitted to the Faculty of the  
DEPARTMENT OF OPTICAL SCIENCES  
In Partial Fulfillment of the Requirements

For the Degree of  
DOCTOR OF PHILOSOPHY

In the Graduate College  
THE UNIVERSITY OF ARIZONA  
2012

THE UNIVERSITY OF ARIZONA  
GRADUATE COLLEGE

As members of the Dissertation Committee, we certify that we have read the dissertation prepared by Qiang Fang entitled 2  $\mu\text{m}$  Pulsed Fiber Laser Sources and Their Application in Terahertz Generation and recommend that it be accepted as fulfilling the dissertation requirement for the Degree of Doctor of Philosophy

\_\_\_\_\_  
Nasser Peyghambarian Date: 06/05/2012

\_\_\_\_\_  
Mahmoud Fallahi Date: 06/05/2012

\_\_\_\_\_  
Khanh Kieu Date: 06/05/2012

\_\_\_\_\_  
Wei Shi Date: 06/05/2012

Final approval and acceptance of this dissertation is contingent upon the candidate's submission of the final copies of the dissertation to the Graduate College.

I hereby certify that I have read this dissertation prepared under my direction and recommend that it be accepted as fulfilling the dissertation requirement.

\_\_\_\_\_  
Dissertation Director: Nasser Peyghambarian Date: 06/05/2012

## STATEMENT BY AUTHOR

This dissertation has been submitted in partial fulfillment of requirements for an advanced degree at the University of Arizona and is deposited in the University Library to be made available to borrowers under rules of the Library.

Brief quotations from this dissertation are allowable without special permission, provided that accurate acknowledgement of source is made. Requests for permission for extended quotation from or reproduction of this manuscript in whole or in part may be granted by the copyright holder.

SIGNED: Qiang Fang

## ACKNOWLEDGEMENTS

I would like to express my sincere gratitude to my academic advisor, Dr. Nasser Peyghambarian, who provided me the opportunity to conduct such an interesting research for this dissertation.

I also would like to express the special appreciation to Dr. Wei Shi and Dr. Khanh Kieu for their enthusiastic support and elaborate advice on my research. Without their thoughtful guidance and encouragement, this dissertation cannot be completed.

My gratitude also extends to Dr. Mahmoud Fallahi for serving as my dissertation committee member and giving me the continued support.

Thanks also go to Dr. Xiushan Zhu, Dr. Eliot Petersen, Dr. Arturo Chavez, Dr. Zhidong Yao, Dr. Jie Zong, Dr. Jianfeng Wu, Dr. Huai Wei, Dr. Ping Lu, Dr. Rajesh Thapa, Yevgeniy merzlyak, Khawlah Al Yahyaei, Nick Moor, Dmitriy Churin, Gongwen Zhu and Chen Wei for their generous help and useful discussion.

I also would like to express my thanks to Tianquan Su, Wenrui Cai, Qian Li, Liang Gao, Yuhao Wang, Xinda Hu, Run Huang, Han Zhang, Ming Zhao, Xiaoyin Zhu, Yubo Jiao and Feng Jiang for their help in the past four years in Tucson.

The immeasurable thanks go to my parents for their deepest love, support and sacrifice. I really appreciate every single piece of it. You always back me up whenever I need help.

## **DEDICATION**

To my parents  
whose love and support bring me where I am

## TABLE OF CONTENTS

LIST OF FIGURES .....	10
LIST OF TABLES .....	16
ABSTRACT .....	17
CHAPTER 1 – INTRODUCTION .....	19
1.1 History and rapid growth of fiber lasers .....	19
1.1.1 Fiber lasers operating at different wavelength band.....	21
1.1.2 Single frequency fiber laser.....	22
1.1.3 Ultrafast fiber laser.....	23
1.1.4 High power & high energy fiber lasers.....	25
1.2 Two-micron lasers.....	28
1.2.1 Introduction to two-micro lasers .....	28
1.2.2 History of two-micro thulium-doped fiber lasers.....	30
1.2.3 Applications of two-micro thulium-doped fiber lasers .....	31
1.3 Terahertz (THz) Technology.....	32
1.3.1 Properties and applications of THz waves.....	33
1.3.2 Terahertz generation.....	34
1.4 Outline of the dissertation.....	36

## TABLE OF CONTENTS - Continued

CHAPTER 2 –HIGH POWER AND HIGH ENERGY ALL-FIBER-BASED SINGLE	
FREQUENCY NANOSECOND PULSED LASER SYSTEM	
OPERATING IN 2 $\mu\text{m}$ REGIME.....	38
2.1 Introduction.....	38
2.2 Thulium doped germanate glass and fiber.....	40
2.3 Continuous wave (CW) single frequency seed operating in 2 $\mu\text{m}$ regime .....	48
2.4 2 $\mu\text{m}$ single frequency nanosecond pulse seed and pulse pre-shaping technique.....	51
2.5 Road-blocks for energy and power scaling of the single frequency nanosecond laser pulses in fiber amplifier.....	54
2.5.1 Gain depletion over nanosecond period .....	55
2.5.2 Nonlinearities .....	55
2.5.3 Optical damage limit .....	56
2.6 Energy scaling of the 2 $\mu\text{m}$ single frequency nanosecond pulses.....	57
2.7 Power scaling of the 2 $\mu\text{m}$ single frequency nanosecond pulses.....	66
2.8 Modeling the pulsed double-cladding thulium doped germanate fiber amplifier.....	70
2.8.1 Rate equations and Propagation equations.....	70

## TABLE OF CONTENTS - Continued

2.8.2	Pulse energy and average power calculation in the LC-TG-DC-FA.....	74
2.8.3	Pulse shape evolution in the LC-TG-DC-FA.....	77
2.8.4	Stored energy in the LC-TG-DC-FA.....	79
2.8.5	Dependence of ASE power on the pump power, seed power and repetition rate.....	84
2.9	Summary.....	86
CHAPTER 3 –TERAHERTZ GENERATION USING 2 $\mu\text{m}$ HIGH POWER AND HIGH ENERGY SINGLE FREQUENCY NANOSECOND PULSES.....		
3.1	Introduction .....	87
3.2	Galium Arsenide (GaAs) crystal.....	87
3.3	Terahertz generation using difference frequency generation (DFG)..	91
3.4	Modeling a collinear singly resonated parametric terahertz oscillator..	93
3.5	THz parametric oscillator pumped by cavity enhanced 2 $\mu\text{m}$ nanosecond pulses.....	100
3.5.1	Design.....	100
3.5.2	Bow-tie cavity stability condition.....	101
3.5.3	Pulse enhancement in the bow-tie cavity.....	103
3.5.4	Implementation of the pulse enhancement in the bow-tie cavity..	105

## TABLE OF CONTENTS - Continued

CHAPTER 4- ALL FIBER WAVELENGTH TUNABLE MODE-LOCKED LASER OPERATING IN 2 $\mu\text{m}$ REGIME.....	109
4.1 Introduction.....	109
4.2 Configuration of the mode-locked laser.....	110
4.3 Wavelength tuning element.....	111
4.4 Mode-locking element.....	113
4.5 Results and discussion.....	114
4.6 Summary.....	116
CHAPTER 5 SUMMARY AND PROSPECT .....	117
5.1 Summary.....	117
5.2 Prospect.....	118
REFERENCES .....	119

## LIST OF FIGURES

Figure 1.1:	Typical fiber geometry .....	20
Figure 1.2:	fiber laser operating at different wavelength .....	22
Figure 1.3:	The concept of cladding-pumped fiber technology. ....	26
Figure 1.4:	Configuration of the master oscillator-power amplifier (MOPA)...	26
Figure 1.5:	Progress in the output power from Yb-doped fiber lasers (from ref. 69).....	27
Figure 1.6:	Electromagnetic spectrum. ....	33
Figure 2.1:	Diagram of energy level of thulium ions.....	42
Figure 2.2:	Cross-relaxation energy transfer between two nearby trivalent thulium	44
Figure 2.3:	(a) Emission spectra and (b) absorption cross-section of thulium ions in germanate glass (pumped at $\sim 800$ nm) with different doping concentration(from ref. 144).....	45
Figure 2.4:	(a) Fiber drawing facility in NP Photonics Inc. ; (b) Cross-section of large core highly thulium doped germanate fibers.....	47
Figure 2.5:	The setup of the scanning FP cavity.....	49
Figure 2.6:	Spectrum of the CW single frequency laser seed .....	50
Figure 2.7:	Output power of the CW single frequency laser seed.....	50

## LIST OF FIGURES - Continued

Figure 2.8:	Diagram of 2 $\mu\text{m}$ single frequency nanosecond pulse seed system.....	52
Figure 2.9:	Initial and amplified pulses (after the filter) for 30 ns (a) rectangular pulse, (b) shaped pulse.....	53
Figure 2.10:	output pulses of pulse generation system (shown in Fig. 2. 8) with different pulse duration.....	54
Figure 2.11:	Schematic of the pulsed MOPA-based system. AWG, arbitrary wave generator; FG, function generator.....	58
Figure 2.12:	Laser system in the lab.....	59
Figure 2.13:	Large-core highly thulium-doped germanate fiber fixed in a copper plate.....	60
Figure 2.14:	Pulse energy and average power versus repetition rate when the pump is fixed at $\sim 8$ W.....	61
Figure 2.15:	Measured pulse energy and peak power for the final power amplifier at different pump level when the repetition rate is fixed at 5kHz. The pump power shown here is the power after the combiner.....	62
Figure 2.16:	The typical pulse shape of the amplified pulses after the final amplifier. Insets: Initial pulse (EOM Modulated) shape; spectrum and the beam profile of the final amplified pulses.....	63
Figure 2.17:	Interference pattern for high energy $\sim 15$ ns pulses ( $> 300 \mu\text{J}$ ).....	64

## LIST OF FIGURES - Continued

Figure 2.18:	Pulse energy at different repetition rate when the pump power is fixed at 6.936 W pump and fixed at 9.95 W, respectively.....	65
Figure 2.19:	Pulse energy at different pump level for ~ 15 ns pulses at 1 kHz repetition rate.....	66
Figure 2.20:	(a) Average power of the pulse under different pump level. Inset: Pulse shape and spectrum when the power is ~16.01 W; (b) Peak power of the pulse under different pump level. Inset: Fabry-Perot scanning spectra of the ~2 ns pulses (over 10 W average power); (C) $M^2$ measurement and beam profile for amplified output pulses.....	67
Figure 2.21:	Energy levels and transitions taken into account in the presented model for $Tm^{3+}$ in germanate glass. ....	72
Figure 2.22:	Energy levels and transitions taken into account in the presented model for $Tm^{3+}$ in germanate glass.....	75
Figure 2.23:	Calculated and measured pulse energy.....	75
Figure 2.24:	The measured and calculated average power of 2 ns pulses at 500 KHz repetition rate.....	76

## LIST OF FIGURES - Continued

Figure 2.25:	(a) Pulse evolution in the amplifier for rectangular pulse; (b) Pulse evolution in the amplifier for gaussian pulse; (c) Rectangular pulse output from the amplifier .....	77
Figure 2.26:	The stored energy in the active fiber for seed pulses at different repetition rate under (a) 20 W and (b) 35 W pump when the seed energy is fixed at 20 $\mu$ J; (c) Stored pulse energy in the active fiber for different seed energy when the pump and repetition rate are fixed at 20 W and 5 KHz, respectively; (d) The stored energy for 1 $\mu$ s and 15 ns seed pulses with 20 $\mu$ J pulse energy .....	80
Figure 2.27:	(a) ASE for pulses at different repetition rate; (b) ASE at different pump level; (c) ASE for different seed power.....	83
Figure 3.1:	Concept of quasi-phase-matching technique.....	89
Figure 3.2:	Pictures of the QPM-GaAs with different periods (1, 2, 5 periods). .....	90
Figure 3.3	Transmission spectra of the QPM-GaAs with different periods.....	90
Figure 3.4	Diagram of the two all fiber nanosecond pulsed laser system. EOM: electro-optical modulator; AOM: acousto-optical modulator; LDs: Laser diodes; SM TDF: single mode thulium doped fiber.....	91
Figure 3.5	Terahertz generation using DFG in QPM-GaAs. PBC: polarization beam combiner; QPM-GaAs: quasi-phase-matched gallium arsenide.....	92

## LIST OF FIGURES - Continued

Figure 3.6	Power of the THz wave for different QPM-GaAs under different pump level.....	93
Figure 3.7:	Configuration of the singly resonated THz parametric oscillator...	94
Figure 3.8:	Threshold of THz OPO for different length of crystal.....	96
Figure 3.9:	Generated THz energy under different pump level.....	97
Figure 3.10:	pulse shapes of residual pump and extracted Idler wave (THz) for different initial pump. ....	98
Figure 3.11:	Configuration of the pump enhanced THz parametric oscillator....	101
Figure 3.12:	Diagram of the bow-tie ring cavity. R is the radius of the curvature mirror; d is the distance between the two curvature mirrors.....	101
Figure 3.13	Stability condition as a function of distance between the two curvature mirrors for different cavity length. The red curves violate $L > 2d$ and are not physical.....	103
Figure 3.14	Enhancement factor as a function of the pulse duration for different cavity length.....	104
Figure 3.15	Enhancement factor as a function of the pulse duration for different transmission of the coupler.....	105
Figure 3.16	Bow-tie ring cavity in the lab.....	106
Figure 3.17	Laser resonances in the bow-tie cavity when its length is adjusted by a piezo.....	106

## LIST OF FIGURES - Continued

Figure 4.1:	Schematic diagram of the all-fiber mode-locked tunable ring laser.....	110
Figure 4.2:	The fiber taper was fixed at two stages used for wavelength tuning element. ....	112
Figure 4.3:	Spectral response of the fiber taper filter and its shift upon stretching.....	113
Figure 4.4:	The CNT based absorber (from <a href="http://www.kphotonics.com">www.kphotonics.com</a> ).....	114
Figure 4.5:	Tuning characteristic of the mode-locked ring laser using an intracavity fiber taper tunable filter.....	115
Figure 4.6:	Output power and pulse duration versus wavelength; the inset is the interferometric autocorrelation trace when the laser wavelength is at 1882.5 nm.....	116

## LIST OF TABLES

Table 2.1:	Parameters used in modeling for LC-TG-DC-FA.....	74
Table 3.1:	linear, nonlinear optical properties, and figures of merit (normalized to LiNbO <sub>3</sub> ) of several popular crystals.....	88
Table 3.2:	Important parameters used in the simulation for singly resonated THz parametric oscillator.....	95

## ABSTRACT

In this dissertation, an all-fiber-based single frequency nanosecond pulsed laser system at  $\sim 1918.4$  nm in master-oscillator-power-amplifier (MOPA) configuration is present. The nanosecond pulse seed is achieved by directly modulating a continuous wave (CW) single frequency fiber laser using a fast electro-optical modulator (EOM) driven by an arbitrary waveform generator (AWG). One piece of single mode, large core, polarization-maintaining (PM) highly thulium-doped (Tm-doped) germanate glass fiber (LC-TGF) is used to boost the pulse power and pulse energy of these modulated pulses in the final power amplifier. This laser system can work in both high power and high energy regime: in high power regime, to the best of our knowledge, the highest average power 16 W and peak power 78.1 kW are achieved for single frequency transform-limited  $\sim 2.0$  ns pulses at 500 kHz and 100 kHz repetition rate, respectively: In high energy regime, nearly 1 mJ and half mJ pulse energy is obtained for  $\sim 15$  ns pulses at 1 kHz repetition rate and 5 kHz repetition rate, respectively.

Theoretical modeling of the large-core highly Tm-doped germanate glass double-cladding fiber amplifier (LC-TG-DC-FA) is also present for 2  $\mu\text{m}$  nanosecond pulse amplification. A good agreement between the theoretical and experimental results is achieved. The model can simulate the evolution of pump power, signal energy, pulse shape and the amplified stimulated emission (ASE) in the amplifier. It can also be utilized to investigate the dependence of the stored energy in the LC-TGF on the pump

power, seed energy and repetition rate, which can be used to design and optimize the LC-TG-DC-FA to achieve higher pulse energy and average power.

Two channel of high energy nanosecond pulses (at 1918.4 nm and 1938 nm) are utilized to generate THz wave in a quasi-phase-matched (QPM) gallium arsenide (GaAs) based on difference frequency generation. THz wave with  $\sim 5.4 \mu\text{W}$  average power and  $\sim 18 \text{ mW}$  peak power has been achieved. Besides, one model is built to simulate a singly resonated THz parametric oscillator. The threshold, the dependence of output THz energy on pump energy has been investigated through this model. One pump enhanced THz parametric oscillator has been proposed. The enhancement factor of the nanosecond pulses in a bow-tie ring cavity has been calculated for different pulse duration, cavity length and the transmission of the coupler. And the laser resonances in the ring cavity have been observed by using a piezo to periodically adjust the cavity length.

We also build an all-fiber thulium-doped wavelength tunable mode-locked laser operating near  $2 \mu\text{m}$ . Reliable self-starting mode locking over a large tuning range ( $> 50 \text{ nm}$ ) using fiber taper based carbon nanotube (FTCNT) saturable absorber (SA) is observed. Spectral tuning is achieved by stretching another fiber taper. To the best of our knowledge, this is the first demonstration of an all-fiber wavelength tunable mode-locked laser near  $2 \mu\text{m}$ .

## CHAPTER 1

### INTRODUCTION

#### 1.1 History and rapid growth of fiber lasers

The laser is often grouped with the transistor and the computer as landmark inventions of the mid-20th century [1]. The birth of the laser triggered the explosion of activities in optics, opened several entirely new scientific fields including nonlinear optics, fiber optics, and opto-electronics and regained revolutionary vigor of this "ancient science". The development of the laser physics and devices has been affecting almost every aspect of our lives and has been pushing forward the progress of other scientific fields, such as medical research, information technology, biological science, etc..

In 1917, Albert Einstein described the theory of "stimulated emission" in which, the matter may lose energy by emitting an exactly same photon when it encounters a photon. This is the initial idea for the laser operation. However, it was not until 1960 that the first laser was demonstrated in a flash lamp pumped ruby crystal by Theodore H. Maiman at Hughes Research Laboratories in Malibu, California [2]. After the birth of this first laser, a large variety of lasers were built using different materials including helium-neon (HeNe) [3], neodymium crystal [4], semi-conductor [5], Nd:YAG [6], CO<sub>2</sub> [7], Argon Ion [8], dye [9], quantum well [10], titanium sapphire [11], etc. The earliest form of fiber laser was also developed by E. Snitzer and his colleagues in 1964 [12]. In this introduction, we will limit our review to the history and rapid growth of the fiber lasers.

A fiber laser is an oscillator using an optical fiber as active medium in the cavity. The core of the fiber is doped with rare-earth elements such as erbium (Er), ytterbium (Yb), neodymium (Nd), dysprosium (Dy), praseodymium (Pr), thulium (Tm), holmium (Ho), and different synthesizers of these elements. Compared with other lasers, fiber laser has a lot of attractive advantages, including outstanding heat-dissipating capability, good beam quality, compactness, robust operation and free of alignment, etc. Fiber lasers have been investigated and developed for more than fifty years. Laser researchers have always been working on building and developing better and cheaper fiber lasers: new operating wavelength, narrower linewidth (single frequency), shorter pulse duration, higher power/energy, etc. The following sections review several of these research efforts in fiber lasers.

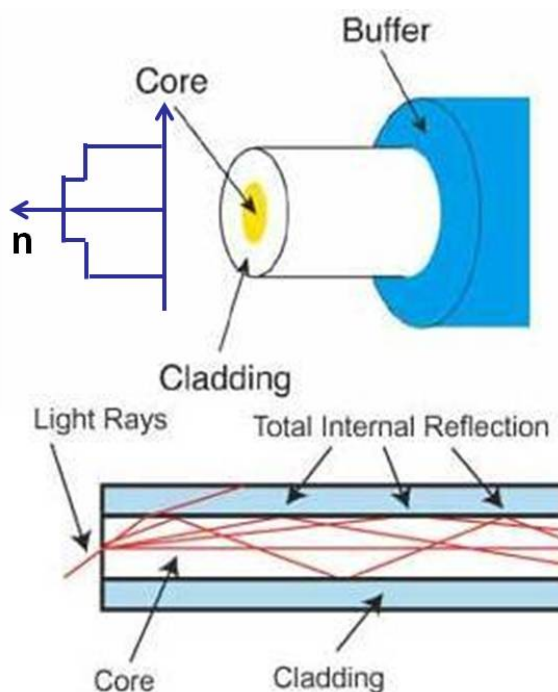


Fig. 1.1 Typical fiber geometry (from Internet)

### 1.1.1 Fiber laser operating at different wavelength band

Fig.1.1 shows the structure of a typical fiber, which consists of a core and a cladding whose refractive index is slightly lower than that of the core so that the light can be guided in the core by total internal reflection. For fiber lasers, the active medium is a piece of fiber whose core is doped with rare earth elements. The operating wavelength band depends on both the doped rare earth elements and the host materials. To date, the spectrum range of the fiber lasers can cover from ultra-violet to mid-infrared. Fig.2 demonstrates some laser wavelength for different rare earth elements doped in certain host materials. Emissions ranging from ultra-violet to visible wavelengths were achieved using Nd-, Tm-, Ho-, Er- or Pr-doped fluorozirconate glass fibers through up-conversion effect[13-19]. Nd- or Yb-doped silica fiber could provide emission around 1  $\mu\text{m}$  [20, 21]. Yb-doped silica fiber is a promising platform for high power applications due to the high optical to optical conversion efficiency. Er-doped silica fiber lasers and amplifiers are operating around 1.55  $\mu\text{m}$  [22, 23], which is located in the communication window. The Er-doped fiber amplifiers have been promoting the development of the optical communications. 2  $\mu\text{m}$  emission can be achieved by thulium or holmium-doped silica or germanate fibers [24, 25]. These fiber lasers will be extensively discussed in this dissertation. Er-doped ZBLAN fiber can provide emission around 2.7  $\mu\text{m}$  [26, 27].

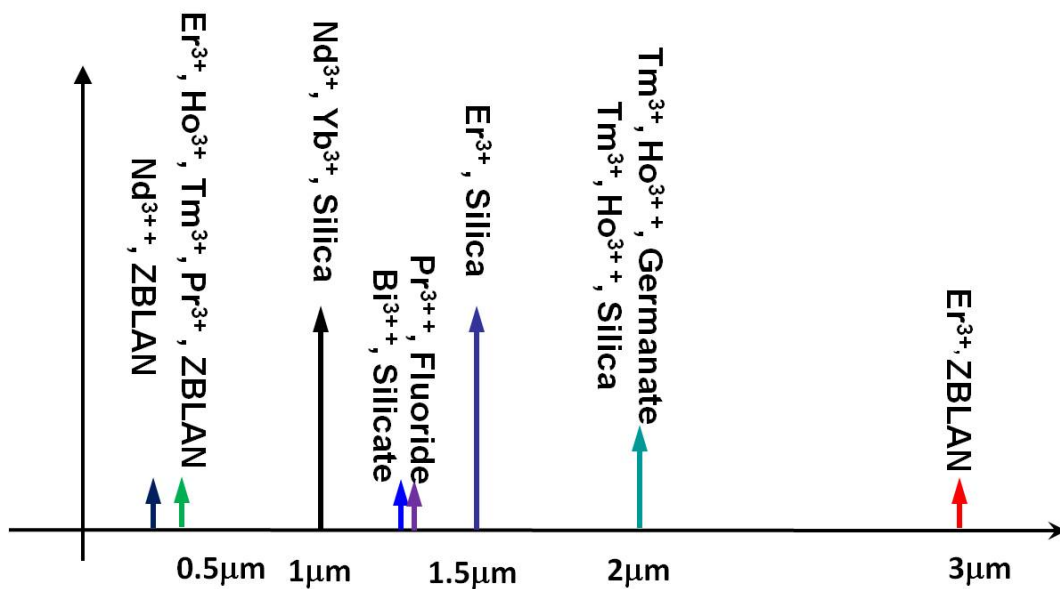


Fig. 1.2 fiber laser operating at different wavelength

### 1.1.2 Single frequency fiber laser

A single-frequency laser is a laser with a single longitudinal mode operation and thus can emit quasi-monochromatic radiation with a very narrow linewidth and low phase noise. Such kind of lasers have been intensively investigated due to their diverse applications in interferometric sensing [28, 29], coherent Light Detection and Ranging (LIDAR) [30], laser spectroscopy [31] and laser nonlinear frequency conversions [32]. A lot of single frequency fiber lasers have been reported using different design. Distributed-feedback (DFB) fiber laser has a fiber Bragg grating (FBG) with a phase change in the middle, which is directly written into a rare-earth-doped fiber. This kind of DFB fiber

lasers can provide single frequency operation and have been already demonstrated in the 1- $\mu\text{m}$  region for  $\text{Yb}^{3+}$  lasers [33], in the 1.55- $\mu\text{m}$  region for the  $\text{Er}^{3+}$  lasers [34] and also in the 2- $\mu\text{m}$  region for the  $\text{Tm}^{3+}$  lasers [35]. The linewidths of the order of a few kilohertz was demonstrated for DFB fiber laser [36]. Another typical design of single frequency fiber lasers is based on a short laser cavity (a short highly doped active fiber) in combination with narrowband FBG. This kind of fiber laser can provide robust single-frequency operation and have already been commercialized [37-39]. There are also some other methods to get narrow linewidth laser performance. For example, Kieu etl. reported a narrow linewidth fiber laser using a microsphere resonator as reflecting "mirror" [40]. The linewidth of this laser is below  $\sim 100$  kHz [40]. Some applications, such as nonlinear frequency conversion, benefit from pulsed single-frequency lasers, which are able to provide high peak powers. Often single-frequency laser pulses are achieved by Q-switching a continuous wave (CW) single-frequency laser oscillator [41, 42]. The other way to get single-frequency laser pulse is to use an electro-optic or acousto-optic (EOM or AOM) to directly modulate a CW single-frequency laser oscillator. And the pulse parameters (duration, repetition rate, pulse shape, etc.) can be free adjusted [43, 44] in this case. This dissertation will discuss in detail a pulsed single frequency laser and its power & energy scaling.

### 1.1.3 Ultrafast fiber laser

After the first demonstration of ultrafast pulse generation in optical fiber in 1990 [45, 46], fiber based ultrafast pulse sources have been intensively investigated. A myriad of mode-locking mechanisms have been developed and the ultrafast pulse generation

have been demonstrated in different active medium and thus in different wavelength bands. Here we review some important mode-locking mechanisms and some reported ultrafast fiber oscillator.

Kerr-type mode-locking techniques are utilized to mode-locking the fiber laser, where Kerr-type saturable absorbers are a nonlinear interferometer inside the fiber cavity [47, 48]. This method is the so-called nonlinear polarization evolution (NPE), which rely on nonlinear interference between two polarization modes. Ref. 47 is the first all-fiber mode-locked lasers using nonlinear interferometer in a figure-eight-cavity configuration.

A semiconductor saturable absorber mirror (SESAM) is a mirror structure with an incorporated saturable absorber. Typically, a SESAM consists a semiconductor Bragg mirror and a single quantum well absorber layer [49]. It has been extensively used for the generation of ultrashort pulses [49]. Fiber laser can also be mode-locked by the implementation of SESAM [50-52]. Compared with the system based on NPE, the achievable pulse duration from fiber lasers mode-locked with SESAM are typically a few times longer due to the slower response time of the SESAM [52].

Single wall carbon nanotubes (SWNTs) and graphene are ideal saturable absorbers due to their low saturation intensity and low cost. They have facilitated easy fabrication of mode-locked fiber lasers [53, 54]. These materials can be directly deposited on the cross-section of the fiber [55] or be designed to interact with the fiber mode via evanacent coupling [56]. Compared with SESAM, they have shorter recovery time [57-59], which can be utilized to phase-lock cavity modes to get shorter pulse. Ref. [60] reviewed the ultrafast fiber lasers mode-locked by carbon nanotubes and graphene.

Soliton fiber lasers are simple and reliable short-pulse sources constructed at anomalous dispersion wavelength region [47, 56]. In the cavity, the nonlinear and anomalous dispersive phase shifts are balanced to form the pulses. A saturable absorber is used to promote the formation of a pulse from noise and to stabilize the pulse against perturbations as it traverses the cavity [61]. Soliton lasers are compatible with Kerr-type mode-locking [47], SESAM [50], SWNTs [56] as well as graphene [54]. There are also some other pulse forming regime including self-similar pulse evolution [62], dispersion managed soliton [63], all normal dispersion pulse evolution (dissipative soliton) [64, 65]. There are several review papers to discuss ultrafast fiber lasers [66, 67].

In this dissertation, a wavelength tunable 2  $\mu\text{m}$  all fiber mode-locked laser will be discussed. It is mode-locked using a carbon nanotube based saturable absorber.

#### 1.1.4 High power & high energy fiber lasers

A fiber oscillator usually can only provide limited power. But high power lasers are required in a myriad of applications, such as material processing, nonlinear frequency conversion, etc. Therefore, power of one fiber oscillator should be scaled to certain power level to satisfy the requirement of applications.

Cladding-pumped fiber technology has revolutionized fiber laser and make power scaling of one fiber oscillator feasible and easy. Fig. 1. 3 demonstrates the concept of this technology. Multimode pump lights is effectively coupled into the inner cladding and then is gradually absorbed by the doped core over the entire fiber length and is converted into the high brightness laser radiation. The power scaling of one fiber oscillator is typically based on master oscillator-power amplifier (MOPA) configuration as shown in

Fig. 1. 4. Several stage of optical amplifier are utilized to scale the power of the laser oscillator.

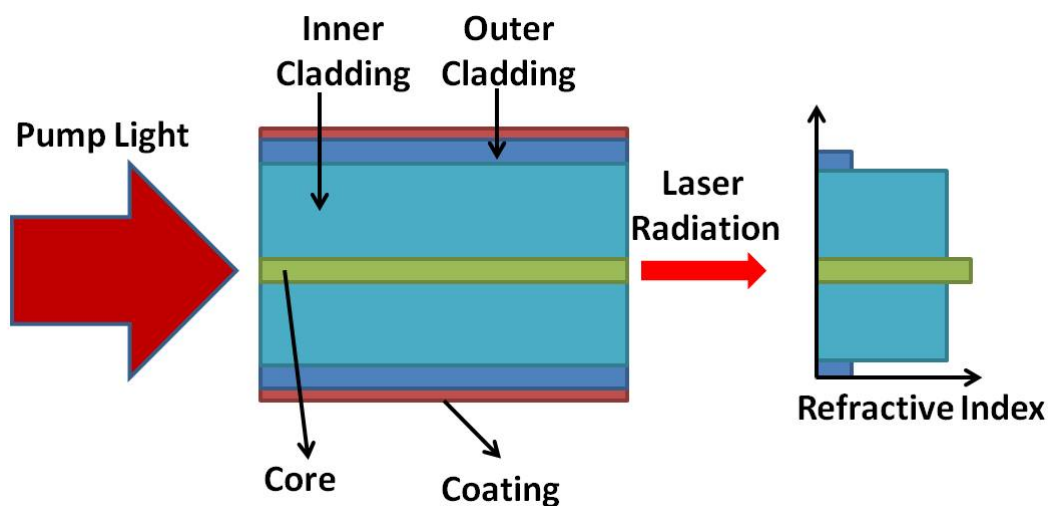


Fig. 1. 3 The concept of cladding-pumped fiber technology.

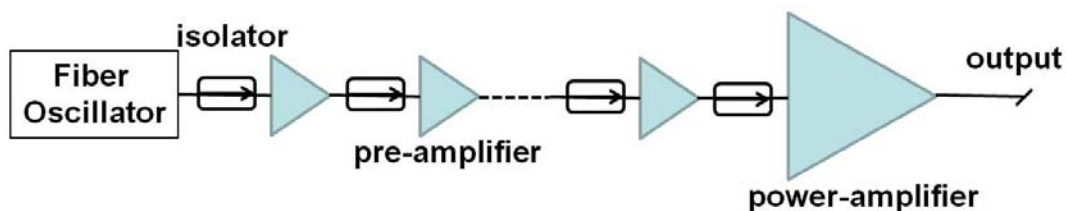


Fig. 1. 4 Configuration of the master oscillator-power amplifier (MOPA).

Ytterbium-doped fiber is a promising medium for high power applications. It has broad absorption band extending from 900 to 980 nm, covering wavelengths at which high power pump laser diodes are at their best. It also has a broad gain bandwidth operating from 975 nm to 1180 nm. The low quantum defect leads to high optical to optical transfer efficiency, which facilitates the power scaling. The power of the Yb-

doped silica fiber lasers reached 10 kW in the single-mode (SM) regime [68]. Fig. 1. 5 demonstrates the progress in output power from diffraction-limited and near-diffraction-limited fiber lasers [69]. All results are with Yb-doped fibers.

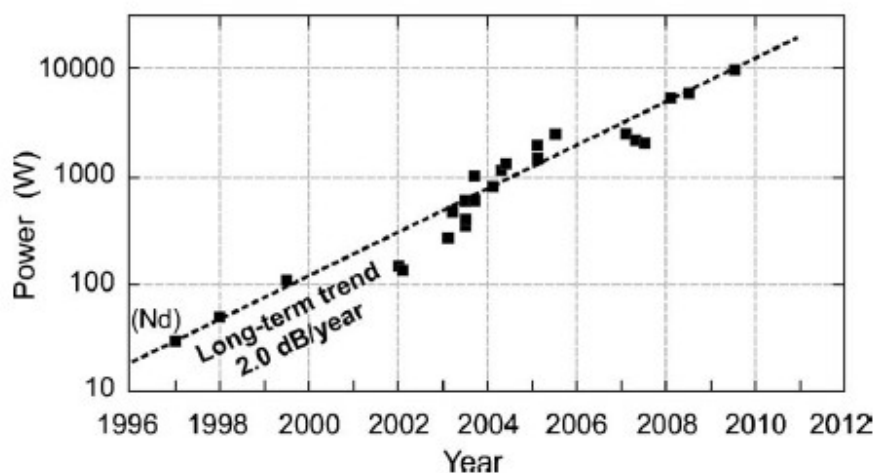


Fig. 1. 5 Progress in the output power from Yb-doped fiber lasers (from ref. [69]).

In addition to the high average power fiber laser sources, high energy and high peak power pulsed fiber laser sources are also desired for a lot of applications. The energy scaling is usually limited by the nonlinearities including stimulated Brillouin scattering (SBS), stimulated Raman scattering (SRS) and self-phase modulation (SPM). The strengths of these nonlinear effects scale linearly (for SPM) or exponentially (for SRS and SBS) in proportion to the fiber length and power, and in inverse proportion to the mode area. Therefore, a variety of active fibers providing large-mode-area and high gains per unit length have been designed and fabricated for pulse energy scaling applications. Here, several significant results in this area are reviewed. Rare-earth-doped single-mode photonic crystal fiber with a mode-field-area of  $\sim 1000 \mu\text{m}^2$  was developed

and used to amplify 10 ps pulses to a peak power of 60 kW [70]. One Yb-doped, 100  $\mu\text{m}$ -core rod-like photonic crystal fiber was used as the final amplifier in a gain-staged MOPA system to boost the energy and the peak power of 1-ns pulses to be  $> 4.3$  mJ and  $\sim 4.5$  MW respectively [71]. A piece of 80  $\mu\text{m}$ -core photonic crystal fiber was used to achieve millijoule level 800 fs pulses at 100 kHz repetition rate [72]. A large-pitch fiber with a core diameter of 135  $\mu\text{m}$  was developed and allowed for single-mode operation. Using it in final amplifier, sub-60 ns pulses with 26 mJ pulse energy and near diffraction-limited beam quality were obtained [73]. NP Photonics Inc. has developed a lot of large core highly rare-earth element doped phosphate and germanate fibers and they have been utilized to scale the energy of single frequency laser pulses in C band [74-76] and also in 2  $\mu\text{m}$  regime [77-79]. This dissertation will discuss the large-core highly thulium doped germanate fibers and their applications in energy scaling and power scaling of single frequency nanosecond pulses in 2  $\mu\text{m}$  regime.

## 1.2 Two-micron lasers

The 2  $\mu\text{m}$  spectral range is part of the so called "eye safe" wavelength region which begins from about 1.4  $\mu\text{m}$ . Recently, a great deal of researches on 2  $\mu\text{m}$  lasers have been conducted in solid-state laser, diode laser and fiber laser field due to its wide applications in medicine, remote sensing, lidar, range finder, and molecular spectroscopy. Here we will review the history and development of 2  $\mu\text{m}$  lasers including solid-state laser, diode laser and especially the fiber laser. Then we will discuss the applications of 2  $\mu\text{m}$  lasers in detail.

### 1.2.1 Introduction to two-micron lasers

Thulium and Holmium are the most well-known rare-earth elements providing emissions around 2  $\mu\text{m}$  wavelength region. Using  $\text{Tm}^{3+}$  and  $\text{Ho}^{3+}$ , laser emissions were achieved in many different host crystals and glass fibers. For both ions the relevant laser transition for the 2  $\mu\text{m}$  emission ends in the upper Stark levels of the ground state. Therefore, both lasers can be described as quasi three level lasers with a thermally populated ground state [80, 81].

Johnson et al. demonstrated the first Tm:YAG laser at 2  $\mu\text{m}$  in 1965 [82]. It was a flash lamp pumped laser operating at 77 K. It is not until 1975 that the first pulsed laser operation at room temperature was built using Cr, Tm: YAG pumped by one 800 nm diode laser [83]. Until now thulium and holmium laser emission around 2  $\mu\text{m}$  was demonstrated in a lot of different host materials, such as Tm: YLF [84], Tm:  $\text{YAlO}_3$  [84], Tm:  $\text{Y}_2\text{O}_3$  [85], Tm:  $\text{Sc}_2\text{O}_3$  [86], Tm: LuAG [87] and Tm:  $\text{Lu}_2\text{O}_3$  [88], Ho: YAG [89, 90].

Apart from the crystal lasers, laser researchers developed 2  $\mu\text{m}$  laser diodes based on the GaSb. Caneau et al. built a double-heterostructure laser operating at 2.2  $\mu\text{m}$  [91]. This laser can work at room temperature but can only deliver very low output power. In 1992, Choi et al. developed the first quantum-well-structured GaSb-based laser diodes and this laser can provide output power up to 190 mW, which is a breakthrough with respect to the upscaling of the laser output power for 2  $\mu\text{m}$  diodes [92]. In 2002, Rattunde et al. designed a direct gap band-edge profile of a laser structure with an emission wavelength around 2  $\mu\text{m}$ . This laser provided a maximum output power of up to 1.7 W at room temperature due to its reduced differential and thermal resistance [93]. The first linear array with this type of diodes was developed by Shterengas et al. in 2004 and it

could provide 10 W output power [94]. In 2007, a multi-bar stack was built with ten linear arrays and could provide up to 158 W. These laser diodes are compact and can provide high power. However, the spatial quality of these laser output are usually very poor and thus limits their applications.

### 1.2.2 History of two-micro thulium-doped fiber lasers

Compared with crystal based lasers and laser diodes, fiber lasers have varieties of advantages, such as easy heat management, better beam quality, easy maintenance, etc. . Here, we will review the history and development of 2  $\mu\text{m}$  thulium-doped fiber lasers.

In 1988, Hanna et. al built the first thulium fiber laser, which was pumped with a dye laser at 790 nm and achieved a few tens of milliwatts of power [95]. They also reported the first wavelength tunable thulium-doped fiber laser with over 276 nm tuning range, from 1780 nm to 2056 nm [96]. This group also demonstrated the first watt-level Tm-doped fiber laser pumped by a readily available Nd: YAG laser at the band of 1064 nm [97]. And the thulium fiber was single clad silica fiber with direct core pumping [97]. In the mid of 1990s, the first mode-locked thulium fiber lasers were reported [98, 99]. Sub-500 fs soliton was achieved tunable from 1798 nm to 1902 nm [98]. Ref. [99] reported 190 fs pulses with 20-pJ energy and the mode-locking threshold of this laser was only 18 mW. One 5.4 W double-cladding thulium-doped fiber laser was reported in 1998 [100]. This laser represents the earliest incarnation of a high power thulium-doped fiber laser scheme that resembles the current state of technology. In 2000, Hayward et. al demonstrated a 14 W efficient cladding pumped highly thulium-doped silica fiber laser [101]. The slope efficiency of this laser was over 46%, which is greater than the quantum

defect. This high slope efficiency resulted from the so called energy cross relaxation, which is a long understood process known to exist in thulium doped crystals [102]. The basic idea of this effect is that two laser photons can be produced from a single pump photon, thus leading to twice the potential slope efficiency compared to the quantum effect. The strength of the cross relaxation highly depends on the thulium doping concentration, which was further studied by Jackson in [103, 104]. The theory behind the process of cross relaxation will be discussed in detail in this dissertation later. The demonstration of this effect in highly thulium-doped fiber and the increase in available diode power lead to the rapid advance in output power for Tm-doped fiber lasers from 12 W in the year 2000 to kilo-watts levels currently achievable [105].

In this period, large-core highly thulium doped germanate fiber were also fabricated and utilized to scale the pulse energy [77-79]. They will be discussed in detail in this dissertation.

### 1.2.3 Applications of two-micro thulium-doped fiber lasers

As mentioned above, the 2  $\mu\text{m}$  wavelength range is called "eye safe" due to the fact that laser radiation of this wavelength is absorbed in the vitreous body of the eye and cannot reach the retina. Applications, including free space communications, remote sensing, LIDAR, standoff chemical detection, all involve propagation through the atmosphere. Consequently, use of lasers in such applications pose a risk for human exposure to laser beams. Therefore, "eye-safe" lasers are highly desired for these applications. Besides, in the wavelength range at 2  $\mu\text{m}$ , there are absorption lines of a

number of atmospheric gases including H<sub>2</sub>O, CO<sub>2</sub> and N<sub>2</sub>O. Therefore, 2 μm lasers can be utilized to detect and analyze these gases.

2 μm laser is also a promising candidate for highly precise surgical applications for both soft and hard tissue. Because the laser at this wavelength range has high absorption in water combined with minimal penetration depth within human tissue. The superficial mid-infrared tissue ablation effects lead to submicron ablation rates which results in minimal damage around the exposed area. Another important thing is that 2 μm laser radiation can induce the coagulation effect, suppressing the bleeding during operations.

2 μm laser is also a promising laser source used for processing some kinds of materials including biological or other organic materials with significant water content, as well as plastics and glasses, which are not transparent in this spectral region.

High power 2 μm laser sources can also be utilized for nonlinear frequency conversion. For example, thulium doped fiber lasers is well suited for nonlinear frequency conversion to obtain mid-IR and THz generation [106, 107]. The longer wavelength gives it an advantage in efficiency over systems pumped by Yb based lasers. And compared with 1 μm lasers, 2 μm lasers have lower absorption in some crystals, such as GaAs, used for nonlinear frequency generation [107].

### 1.3 Terahertz (THz) Technology

Terahertz (THz) wave , also known as T-rays, occupy a large portion of the electromagnetic spectrum (see Fig. 1. 6) between the infrared and microwave bands (from 0.1 to 10 THz) that is rich in science and is unexplored technology. Intensive

researches on THz science have been conducted since the first demonstration of coherent detection of THz waves by Auston and Smith in 1983 [108].

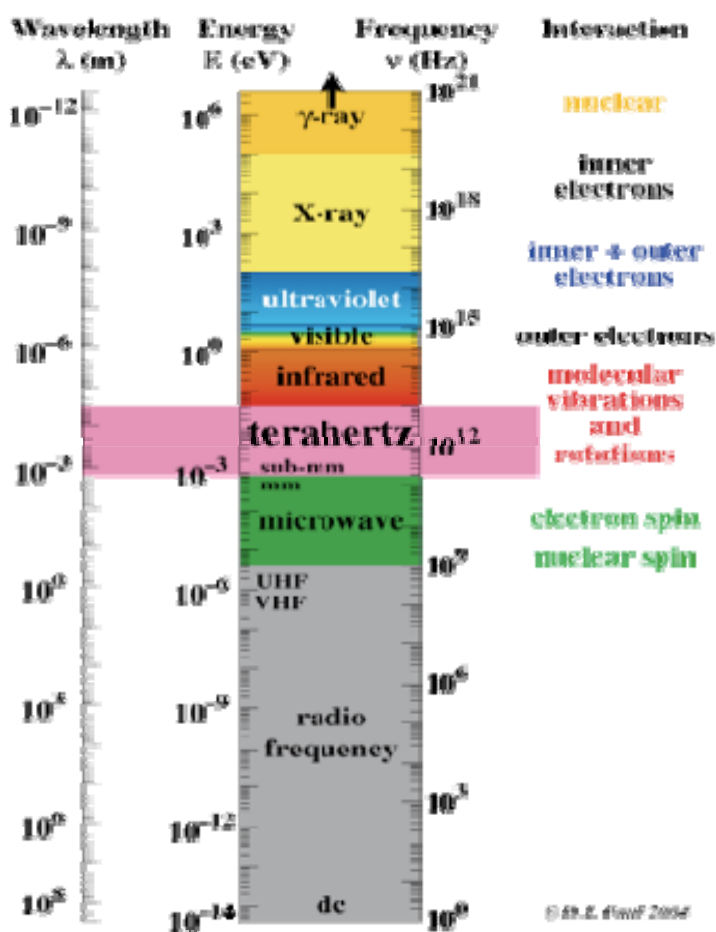


Fig. 1. 6 Electromagnetic spectrum (from C. D. J. Paul, 2004).

### 1.3.1 Properties and applications of THz waves

Compared with electromagnetic waves at other frequency region, THz waves have a lot of special properties leading to many potential applications.

One of the attractive properties of THz waves is that a myriad of non-polar, dry, and nonmetallic materials are transparent or translucent to terahertz radiation, just as many substances are relatively transparent to radio waves and x-rays. This transparency motivates the application of T-rays in quality control and security applications [109, 110]. For example, it can be used to see the weapons concealed beneath clothing or products contained in plastic packages.

Another interesting properties of T-rays is that most polar molecules including solid and liquid phase absorb unique T-ray energies for their intermolecular vibrational transitions [111-113]. And polar molecules in the gas phase have their rotational transition energies spanning the microwave and T-ray frequencies [114-116]. So T-rays can be used for material characterization, classification or recognition by spectroscopy.

THz technology and imaging also has many potential medical applications, because T-rays are highly sensitive to the hydration level in biological tissue. The significance is that T-rays are non-ionizing and thus harmless to the human tissue [117, 118]. It is a promising replacement of X ray in medical imaging.

### 1.3.2 Terahertz generation

Radio frequency (RF) is a rate of oscillation in the range of about 3 kHz to 300 GHz. Microwaves are radio waves with frequencies between 0.3 GHz and 300 GHz. Radio frequency (RF) sources can be easily generated through electronic method [119]. Ultraviolet waves, infrared waves and mid-IR waves can be achieved by lasers. However, it has proven difficult to create efficient and powerful sources of radiation in THz band. And there is more room to do the research to achieve efficient and powerful THz sources.

There are a lot of techniques to generate THz radiation including electronics related techniques and optical related techniques. Electronic techniques includes free electron lasers [120], photoconductive switching [121] and dipolar antennas. These methods are usually complicated and expensive. Here we prefer to introduce optical methods to generate THz radiation.

One method is to build quantum cascade lasers (QCLs) to produce THz waves [122]. QCLs are similar to typical diode lasers to be made by depositing semiconductor layers in multiple quantum well structures. The main problem of the QCLs is their requirement for a low operating temperature.

There are also some nonlinear optical techniques to generate THz waves including optical rectification, the difference frequency generation (DFG) and the parametric generation. They are all based on nonlinear second order processes, which occur in all non-centrosymmetric materials. Optical rectification is a process in which a laser pulse traveling through a nonlinear crystal induces a time-dependent polarization change that radiates an electromagnetic wave [123]. Femto-second pulses are usually utilized in this method and thus the generated THz wave has very broad bandwidth limiting effectiveness in spectrally resolved imaging. Narrow-band THz waves can be achieved by mixing two high peak power nanosecond pulses in one nonlinear crystal through DFG. Shi et al. demonstrated a continuously tunable (0.18-5.27 THz) and coherent THz radiation in the wide range based on collinear phase-matched DFG in a GaSe crystal [124]. Apart from the DFG, THz parametric oscillator was also demonstrated in ref. [125]. Continuous THz waves tunable from 1.2 to 2.9 THz with

output power level between 0.3 and 3.9  $\mu\text{W}$  were generated in this THz parametric oscillator.

#### 1.4 Outline of the dissertation

In this dissertation, I report recent development of an all-fiber-based high power and high energy single frequency nanosecond pulsed laser system operating in 2  $\mu\text{m}$  regime, and its application in THz generation.

In chapter 2, the basics of the thulium ions doped in germanate glass and the theory of the cross-relaxation are reviewed. Then we report a single frequency nanosecond pulse seed at 2  $\mu\text{m}$  and pulse pre-shaping techniques. Then the power and energy scaling of this pulse seed are presented. This chapter also reports a numerical model for the pulsed double-cladding highly thulium doped germanate fiber amplifier.

Chapter 3 reports the THz generation using the single frequency high energy and high power 2  $\mu\text{m}$  nanosecond pulses. Firstly, difference frequency generation (DFG) are used to generate THz waves by mixing two pulsed laser beam in a quasi-phase-matched GaAs crystal. Then we describe a model to simulate a collinear THz parametric oscillator. At last, one pump enhanced THz parametric oscillator are proposed.

Chapter 4 reports an all-fiber 2  $\mu\text{m}$  wavelength-tunable mode-locked laser using a fiber taper embedded in single wall carbon-nanotube & polymer composite as the absorber in the laser cavity. The wavelength tuning element is a home-made adiabatic fiber taper. The wavelength of this mode-locked laser can be continuously tuned over 50 nm by stretching this fiber taper and the pulse duration is around  $\sim 1$  ps.

In chapter 5, the summary of my dissertation and the prospect of my work are given.

## CHAPTER 2

### HIGH POWER AND HIGH ENERGY ALL-FIBER-BASED SINGLE FREQUENCY NANOSECOND PULSED LASER SYSTEM OPERATING IN 2 $\mu\text{m}$ REGIME

#### 2.1 Introduction

Single frequency fiber lasers have been receiving intense interests due to their diverse applications in interferometric sensing, coherent LIDAR, spectroscopy and nonlinear conversion. Such kinds of fiber lasers at 1, 1.55 and 2  $\mu\text{m}$  have been well developed and commercialized with a typical design of a very short laser cavity in combination with narrowband fiber Bragg gratings for robust single-frequency operation [37-39]. Pulsed single-frequency lasers, which are able to provide high peak powers, are achieved by Q-switching a continuous wave (CW) single-frequency laser oscillator [41, 42]. An electro-optic or acousto-optic modulator (EOM or AOM) can also be utilized to directly modulate a CW single-frequency laser. And this allows the pulse parameters (duration, repetition rate, pulse shape, etc.) to be freely adjusted [43, 44].

Single-frequency fiber oscillators usually can only provide limited power or pulse energy. In the high power or high pulse energy regime, a single-frequency fiber laser source is typically configured as a high-gain master oscillator power amplifier (MOPA) seeded by a low power laser for both CW regime [126-130] or pulsed regime [74-79, 131]. Power and energy scaling for these lasers is more challenging due to their narrow bandwidth, which leads to lower threshold of the Stimulated Brillouin Scattering (SBS).

So, usually a large-core gain fiber is used in the final power amplifier to mitigate the SBS [74-79]. G. D. Gooden et al. reports a 608 W CW single frequency fiber laser source at 2040 nm, which is the highest reported average power achieved from any single-frequency, single-mode fiber laser [129]. C. D. Brook et al. reported a single frequency pulse laser at 1062 nm with >1 mJ pulse energy and > 1 MW peak power [131]. However, these systems contain a lot of bulk components, which to some extent sacrifices the benefits of fiber laser sources.

Thulium (Tm)-doped fibers are a promising medium for building high power fiber laser sources due to the availability of commercial efficient high power 790 nm diode pumps and the 200% theoretical quantum efficiency because of the energy cross-relaxation process (two Tm ions can be excited by one pump ion) [103]. And the transition ( $^3F_4 \rightarrow ^3H_6$ ) of trivalent thulium provides radiation near 2  $\mu\text{m}$ , which is eye-safe and has wide applications including remote sensing, LIDAR, military and medical applications. It also provides higher conversion efficiency to be used in nonlinear frequency generation for mid-IR and THz sources [107, 132]. Therefore, it is significant to build a high power and high energy all-fiber based single frequency pulsed laser source in the 2  $\mu\text{m}$  regime using thulium doped active fiber. Here, we report a such kind of high power and high energy single frequency monolithic nanosecond pulsed laser system by using a large core, highly Tm-doped germanate glass fiber. All fiber-based construction of this pulsed fiber laser system in MOPA configuration enables robust, maintenance-free and high performance operation. A theoretical model has also been developed to simulate

the performance of the LC-TG-DC-FA. The simulated results can provide guidance to optimize the germanate fiber amplifier.

## 2.2 Thulium-doped germanate glass and fiber

The highest power record of fiber laser is held by Ytterbium-doped lasers at 1  $\mu\text{m}$  region: IPG Inc. is able to provide up to  $\sim 50$  kW Ytterbium fiber laser system [133]. Although Ytterbium fiber laser is still the workhorse of high power fiber laser application, a lot of attention starts to focus on the thulium doped fiber laser system for high power and high energy application. Compared with Ytterbium, thulium has a myriad attractive features. For example, it provides very broad emission spectrum for the  $^3F_4$ -  $^3H_6$  transition, spanning the wavelength range from  $\sim 1700$  to  $2100$  nm [134] located in the "eye safe" region. Another very important feature is that thulium doped fibers are able to be scaled to much larger mode areas while maintaining single-mode performance due to the longer operating wavelength. The larger mode areas can enable higher threshold of nonlinearities including SBS, Raman, self-phase-modulation etc. in the amplifier. Besides, when the thulium ions is pumped at  $\sim 790$  nm, the cross-relaxation effect can be induced if the doping concentration is high enough and this effect can lead to theoretical 200% quantum efficiency (one pump photon excite two laser photon) [103].

A lot of high power high efficient thulium-doped fiber laser system have been reported. In 1990, D. C. Hanna et al. built the first watt-level continuous-wave (CW) thulium-doped silica fiber laser operating at  $2 \mu\text{m}$  in University of Southampton [97]. The thulium fiber was core-pumped by a Nd: YAG laser at  $1.064 \mu\text{m}$ .  $1.35$  W output power and 37% slope efficiency were achieved [97]. In 1998, S. D. Jackson and T. A. King

demonstrated a 790-nm-diode-cladding-pumped thulium-doped silica fiber laser with over 5 W output power and ~31% slope efficiency [100]. The active fiber is a double-clad silica fiber with a 17- $\mu\text{m}$ -diameter core and a  $300\ \mu\text{m} \times 110\ \mu\text{m}$  rectangular inner cladding. The  $\text{Tm}^{3+}$ -ion concentration in the core is ~ 1.85 wt.% [100]. In 2000, R. A. Hayward et al. demonstrated a cladding-pumped Tm-doped silica fiber laser providing 14 W CW single mode output power and ~46% slope efficiency. This slope efficiency is higher than the quantum defect and thus firstly experimentally verify the cross-relaxation effect. As the development of double cladding fiber with high thulium doping concentration, the output power and the efficiency of the Tm-doped fiber laser have steadily risen. The output power of the thulium-doped fiber laser operating at 2  $\mu\text{m}$  has been rising from tens of watts to kilowatts level [105, 129, 135-139]. In all the above lasers, the active fibers are thulium-doped silica fiber. In 2007, J. Wu et al. reported a highly thulium doped germanate fiber laser, which provided a record slope efficiency of 68% [140]. In the next section, highly thulium doped glass and fiber will be discussed.

Thulium, the atomic number is 69, was discovered by Per Theodor Cleve (a Swedish chemist), while looking for impurities in erbia in 1879. The energy level of thulium ion in germanate glass is demonstrated in Fig. 2. 1. The electrical transition ( ${}^3\text{F}_4$ - ${}^3\text{H}_6$ ) of thulium ions shown in Fig. 2. 1 is a well-known transition utilized as 2  $\mu\text{m}$  light source. Thulium ions have several absorption bands located at ~793 nm ( ${}^3\text{H}_6$ - ${}^3\text{H}_4$ ), ~1210 nm ( ${}^3\text{H}_6$ - ${}^3\text{H}_5$ ) and ~ 1570 nm (resonated absorption) (see Fig. 2. 3 (b)). The absorption band around the 1210 nm is very broad and several thulium fiber lasers pumped at this absorption band were reported [97, 141]. The pump sources are Nd : YAG lasers emitting

at 1064 nm [97] and 1319 nm [141]. The resonant pumping at 1570 nm is also extensively used to build thulium doped fiber laser [138]. Single mode 1570 nm pump sources can be easily achieved by erbium-doped fiber lasers or amplifiers. Ref. [138] reported a 415 W thulium fiber laser which is resonated pumped at 1567 nm. One piece of double cladding single mode thulium-doped fiber was used, which was end pumped by an assembly of eighteen erbium-doped fiber lasers. However, Tm-doped fiber laser, which provided highest output power, was pumped by 793 nm commercial GaAlAs laser diodes [105].

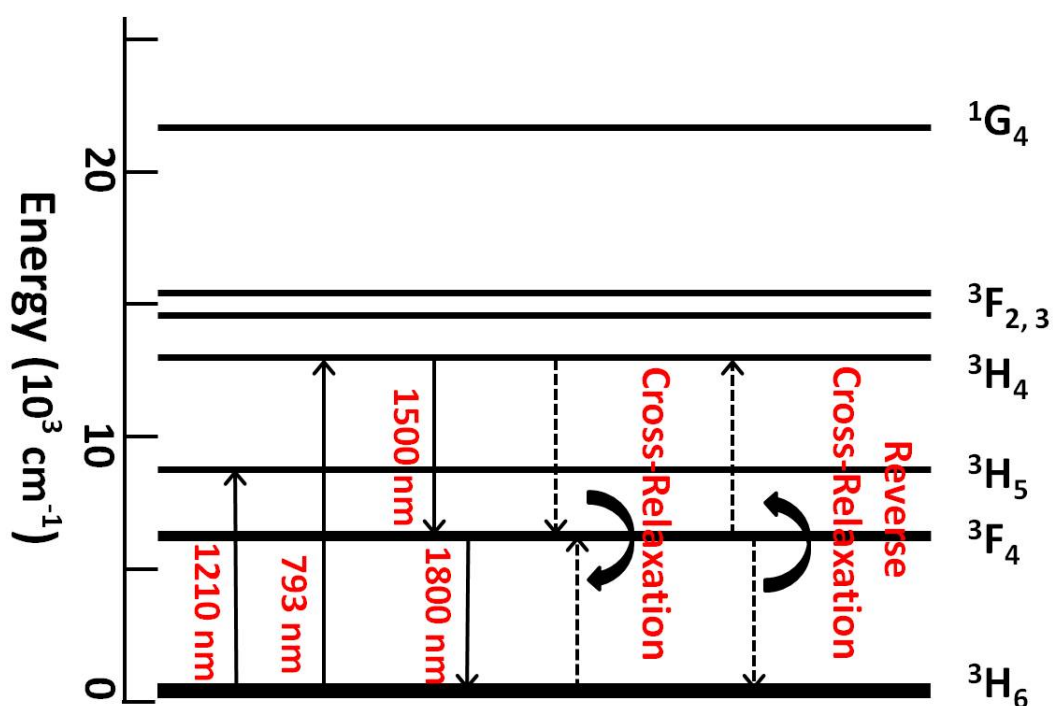


Fig. 2. 1 Diagram of energy level of thulium ions.

The most attractive pumping band for thulium is the 793 nm band due to the cross-relaxation energy transfer between one excited (at  ${}^3\text{H}_4$ ) and one ground state thulium ions (at  ${}^3\text{H}_6$ ). Cross-relaxation is a process in which an excited ion transfers part of its energy to a neighboring ion. Dexter and Forster first developed the theory of energy transfer in solid state based on ion-ion interaction produced by electric multi-polar interaction rather than emission and re-absorption of fluorescence [142, 143]. As Fig. 2.2 shown, when two thulium ions are close enough, the cross-relaxation energy transfer ( ${}^3\text{H}_4$ ,  ${}^3\text{H}_6$ - ${}^3\text{F}_4$ ,  ${}^3\text{F}_4$ ) will be triggered: One thulium ions at ground state ( ${}^3\text{H}_6$ ) can be excited to the upper laser level ( ${}^3\text{F}_4$ ) by absorbing the energy released from another nearby excited thulium ions that decays from  ${}^3\text{H}_4$  state to the  ${}^3\text{F}_4$  state during the cross-relaxation energy transfer process. In the cross-relaxation energy transfer between thulium ions, phonons are necessary to bridge the energy gap between the two transitions. In this process, two thulium ions at ground state are excited to the upper laser level by absorbing only one pumping photon at  $\sim 793$  nm that overlaps the ground absorption band of  ${}^3\text{H}_4$ . The cross-relaxation energy transfer rate heavily dependent on the thulium doping concentration. Therefore the doping concentration is an essential character defining the efficiency of thulium doped fiber laser & amplifier operating at 2  $\mu\text{m}$  region.

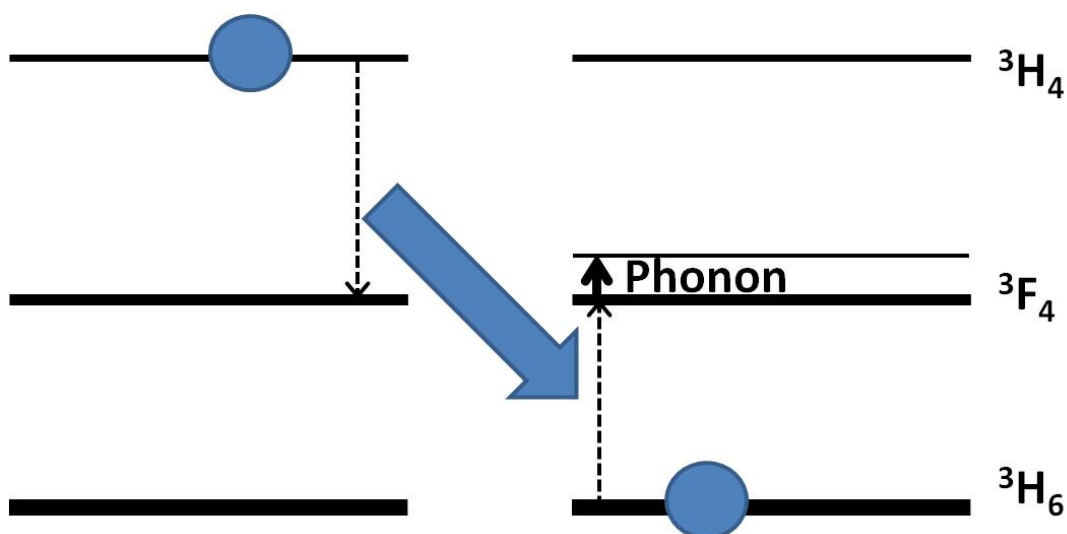


Fig. 2. 2 Cross-relaxation energy transfer between two nearby trivalent thulium.

Fig. 2. 3 (a) demonstrates the emission spectra of thulium doped germanate glass (pumped at  $\sim 800$  nm) with different doping concentration, fabricated in NP photonics Inc. [144]. The spectra were normalized at  $1.8 \mu\text{m}$  in order to illustrate the effect of cross-relaxation energy transfer on emission spectrum of thulium ions. When the doping concentration is low, the emission spectrum has strong emission spectrum near  $1.5 \mu\text{m}$  induced by multi-phonon relaxation. As the increase of thulium ions doping concentration from 0.5 wt% to 4 wt%, the fluorescence intensity ratio between  $1.8 \mu\text{m}$  band and  $1.5 \mu\text{m}$  band keeps a rapid increase. Afterward the ratio does not change as rapidly as it does in small doping concentration range. This enhancement of ratio results from the enhanced cross relaxation energy transfer. Because according to the multi-polar interaction theory, the closer thulium ions are, the higher transfer rate they get. Therefore, the cross-relaxation energy transfer rate becomes so large that most thulium ions at  $^3H_4$

state would irradiatively decay to  $^3F_4$  state through cross-relaxation energy transfer rather than radiatively decay to  $^3H_4$  state by emitting 1.5  $\mu\text{m}$  photons.

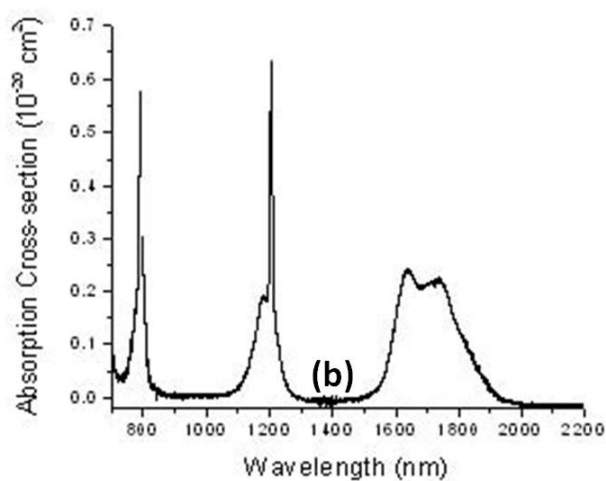
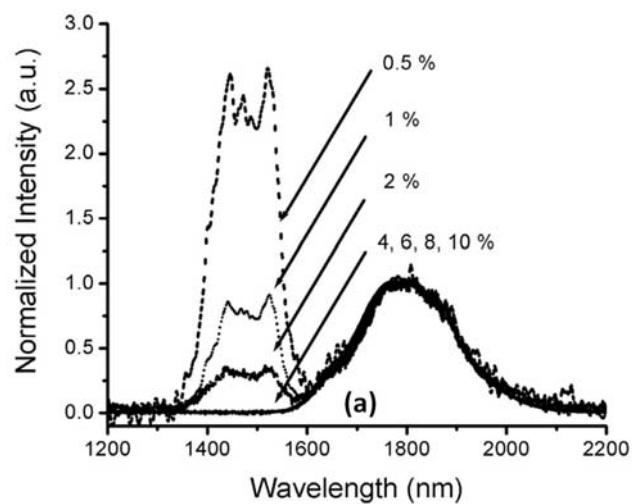


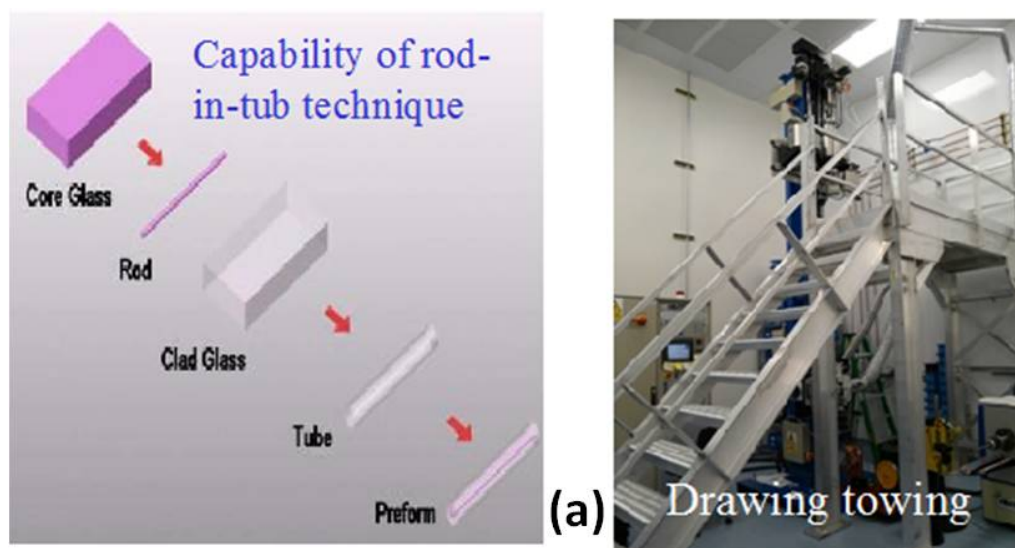
Fig. 2. 3 (a) Emission spectra and (b) absorption cross-section of thulium ions in germanate glass (pumped at  $\sim 800$  nm) with different doping concentration (from ref.

144).

Here, we discuss several host materials: silica glass, silicate glass, fluoride glass and germanate glass. Silica glass is the most popular material for fabricating optical fibers. The strong electron bond which exists between the silicon and oxygen atoms gives silica glass very good mechanical strength and thermal stability. However, silica glass cannot accommodate many rare earth ions before clustering occurs due to the strong electron bond. Silicate glass is a multi-component glass and usually contains  $\text{SiO}_2$  with some other components, such as  $\text{Na}_2\text{O}$ ,  $\text{Al}_2\text{O}_3$ , etc. The  $\text{Na}_2\text{O}$ ,  $\text{Al}_2\text{O}_3$ , or some other components work as network-modifiers. These modifiers act to break the bridging oxygen of  $\text{SiO}_2$  to form non-bridging oxygen which can be used to co-ordinate the rare earth ions to improve the doping capability. Ref. [145] reported the measured Raman spectra for silica glass and for silicate glass with different concentration of  $\text{Na}_2\text{O}$ . We could find that the Raman spectra of the silica glass has a strong band around  $400\text{ cm}^{-1}$  and a relatively weak band around  $1100\text{ cm}^{-1}$ . Silicate glasses has strong bands at both  $400\text{ cm}^{-1}$  and  $1100\text{ cm}^{-1}$ . This measured Raman spectra verifies that the phonon energy of silica and silicate glass can extend to  $1100\text{ cm}^{-1}$ . This high phonon energy makes them not ideal host materials for thulium ions due to the fact that fast multi-phonon relaxation can be induced to decrease the quantum efficiency of thulium fiber lasers. In contrast, the fluoride glass and germanate glass has relatively low phonon energy ( $500\text{ cm}^{-1}$  for fluoride glass [146],  $900\text{ cm}^{-1}$  for germanate glass [147]). And both materials have high doping capability for thulium ions. But fluoride glasses have weak mechanical strength, making them difficult to handle. Based on these discussions, germanate glass is chosen as the host material for

our thulium doped active fiber due to its high doping capability, low phonon energy and good mechanical stability.

Using rod-in-tube technique, large core highly thulium-doped germanate fibers are fabricated in NP Photonics Inc.. The preforms are made by using mechanical method rather than by a vapor deposition process. Specifically, cladding tube is fabricated by ultrasonic drilling on a bulk glass made by melt-casting method. The rod is made by polishing a thulium-doped germanate glass. The preform is made by typical rod-in-tube technique (see Fig. 2. 4 (a)). Two stress rods are fabricated in the cladding near the core to make the fiber polarization-maintained. The refractive index of the glasses can be accurately controlled to make the numerical aperture (NA) to be  $\sim 0.054$ . We make two kinds of active fibers with the core and cladding diameter of 25/250  $\mu\text{m}$ , 30/300  $\mu\text{m}$ , respectively (see Fig. 2. 4 (b)). So the V-number can be calculated to be  $\sim 2.120$ ,  $\sim 2.544$  respectively. So for 25/250  $\mu\text{m}$  fiber, it is a strictly single-mode fiber. For the other fiber, it can also provide single-mode performance by handling the active fiber carefully.



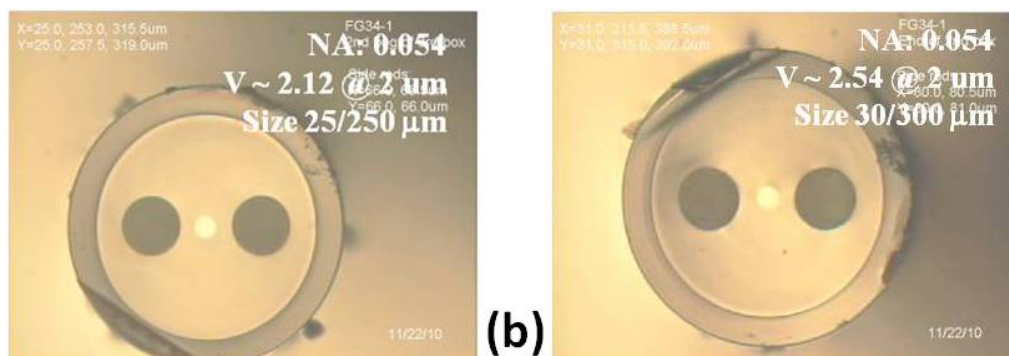


Fig. 2. 4 (a) Fiber drawing facility in NP Photonics Inc. ; (b) Cross-section of large core highly thulium doped germanate fibers.

### 2.3 Continuous wave (CW) single frequency seed operating at 2 $\mu\text{m}$ region

The 2  $\mu\text{m}$  CW single-frequency seed laser is one of the products in NP Photonics Inc. The active fiber is a piece of highly Tm-doped (5% wt) germanate fiber with  $\sim 7 \mu\text{m}$  core.  $\sim 2 \text{ cm}$  active fiber was fusion spliced between two fiber Bragg gratings (FBGs). One was fabricated on a non-Polarization-maintained (PM) silica fiber and has large reflectivity. The other one (output coupler) has lower reflectivity and was imprinted on a PM silica fiber, creating two different reflection peaks for the two different polarizations. The laser can provide linearly polarized laser radiation.

We built a scanning Fabry-Perot (FP) monochromator to measure the spectrum of the single frequency laser. Fig. 2. 5 shows the home-built FP monochromator. The linear cavity consists a mirror with 250 mm curvature radius and a plane mirror. Both of the mirror have  $\sim 99\%$  reflectivity for the laser wavelength. The plane mirror is placed in a piezo, driven by a tunable voltage source. The length of the FP cavity is  $\sim 5 \text{ cm}$ .

Therefore, the FSR can be calculated to be  $\sim 3$  GHz. The finesse of the FP cavity can be calculated to be  $\sim 312.8$  by using the Eq. 2. 1,

$$F = \frac{\pi\sqrt{R}}{1-R} \quad (2.1)$$

Where F is the finesse and R is the reflectivity of the cavity mirror. So the bandwidth of the FP cavity can be calculated to be  $\sim 9.6$  MHz.

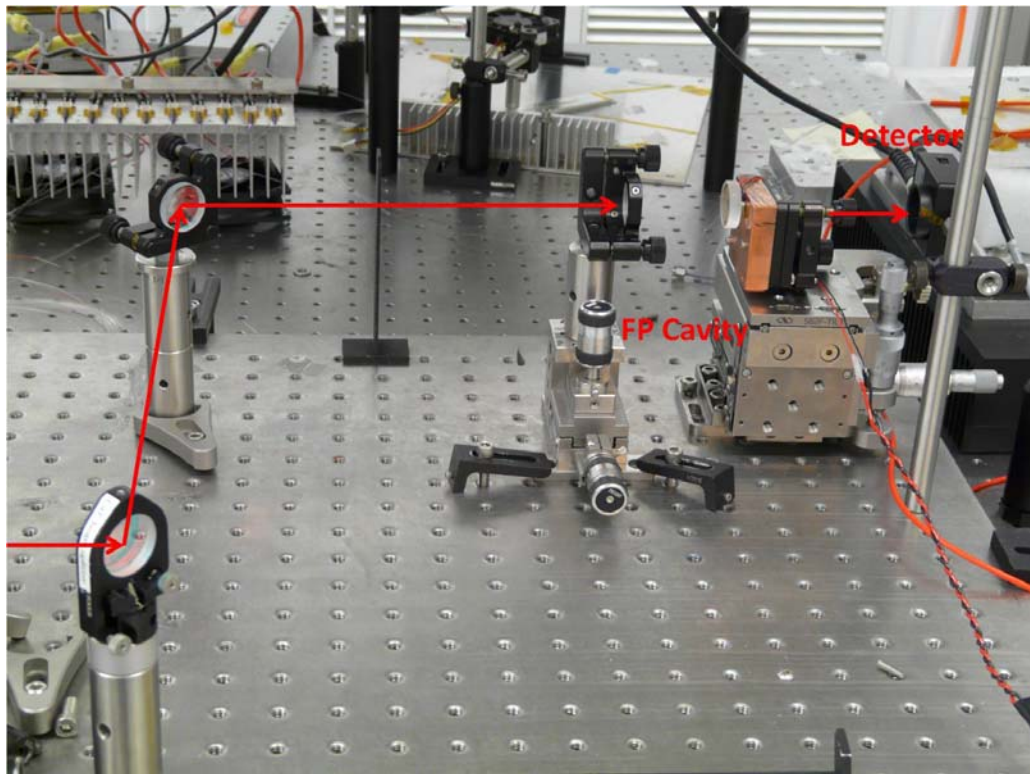


Fig. 2. 5 The setup of the scanning FP cavity

Fig. 2. 6 demonstrates the spectra of the  $2\ \mu\text{m}$  CW single frequency laser seed and also its zoomed-in spectrum. From the spectrum, the single frequency performance of the CW laser seed is verified.

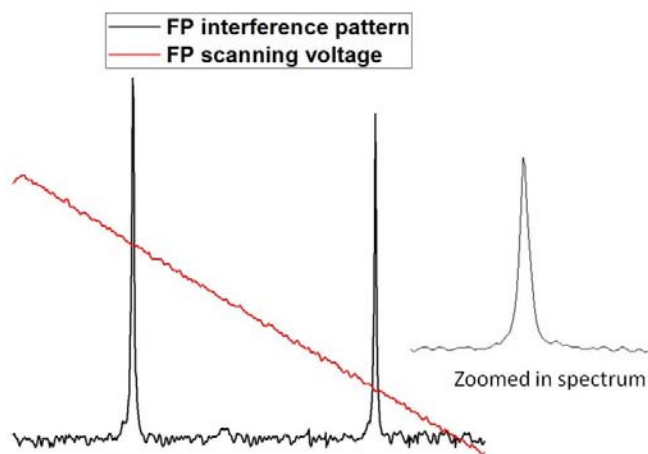


Fig. 2. 6 Spectrum of the CW single frequency laser seed

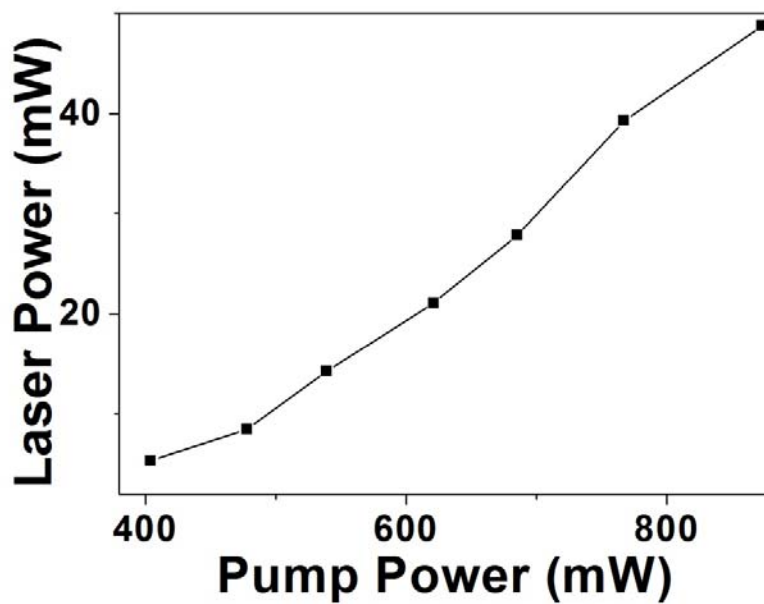


Fig. 2. 7 Output power of the CW single frequency laser seed.

The laser was pumped by a  $\sim 1570$  nm single mode laser source. The seed can provide up to  $\sim 50$  mW linearly polarized laser radiation (see Fig. 2. 7).

#### 2.4 $2 \mu\text{m}$ single frequency nanosecond pulse seed and pulse pre-shaping technique

As mentioned in the introduction, we report a high power and high energy single frequency monolithic nanosecond pulsed laser system by using a large core, highly Tm-doped germanate glass fiber based on the master oscillator power amplifier (MOPA) configuration. From this section, we will introduce this laser system in detail.

Fig. 2. 8 demonstrates the diagram of our  $2 \mu\text{m}$  single frequency nanosecond pulse seed system, which consists of an electro-optic modulator (EOM) to directly modulate the CW fiber laser, a Tm-doped fiber pre-amplifier to boost the power of these pulses, an acousto-optic modulator (AOM) (time synchronized to the EOM) to remove the in-band amplified stimulated emission (ASE) and increase the extinction ratio, another Tm-doped fiber preamplifier to further boost the power of these pulses, and a narrow band-pass filter (combining a PM circulator and a fiber Bragg grating) for removing out-of-band ASE generated by the amplifier. The gain fiber used in the two pre-amplifiers is 2 m of commercial PM Tm-doped fiber (from Nufern Inc.) with a  $\sim 9 \mu\text{m}$  core. The pump for the two pre-amplifiers are two  $1570$  nm single mode laser sources.

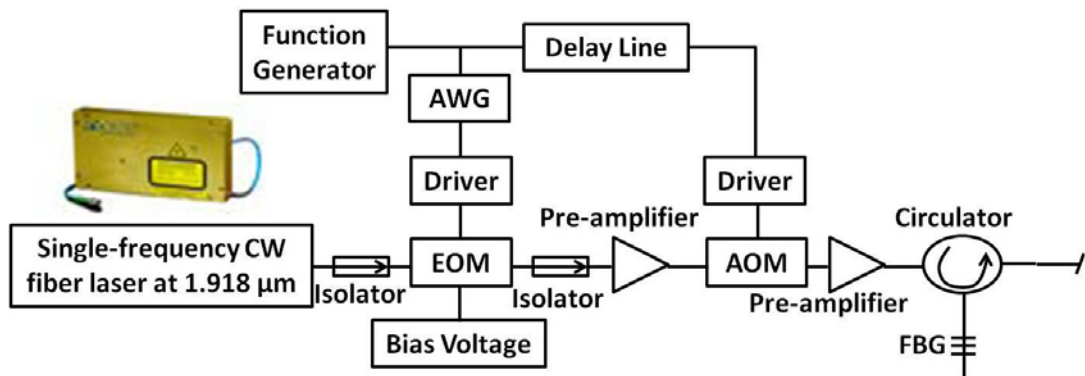


Fig. 2. 8 Diagram of 2  $\mu\text{m}$  single frequency nanosecond pulse seed system

In the fiber amplifier for ns pulses, gain depletion over the time scale of the pulse always distorts the pulse shape [148]. Fig. 2. 9 (a) shows this pulse distortion with an initial rectangular pulse after the EOM and its amplified version (after the filter shown in Fig. 2. 8). To mitigate this, an arbitrary waveform generator (AWG) was used to drive the EOM to pre-shape the pulses and make its leading edge gently sloped to limit its gain or steepening (see Fig. 2. 9 (b)). In addition, the pulse duration and repetition rate can be freely adjusted in our system. The shortest pulse duration is  $\sim 2$  ns, which is limited by the speed of the EOM. Fig. 2. 10 demonstrates several pulses with different pulse duration at the output of the nanosecond pulse system. These pulses keep good pulse shape and have large signal to noise ratio ( $>40$  dB) in spectral domain, which makes them suitable seed sources for power and energy scaling.

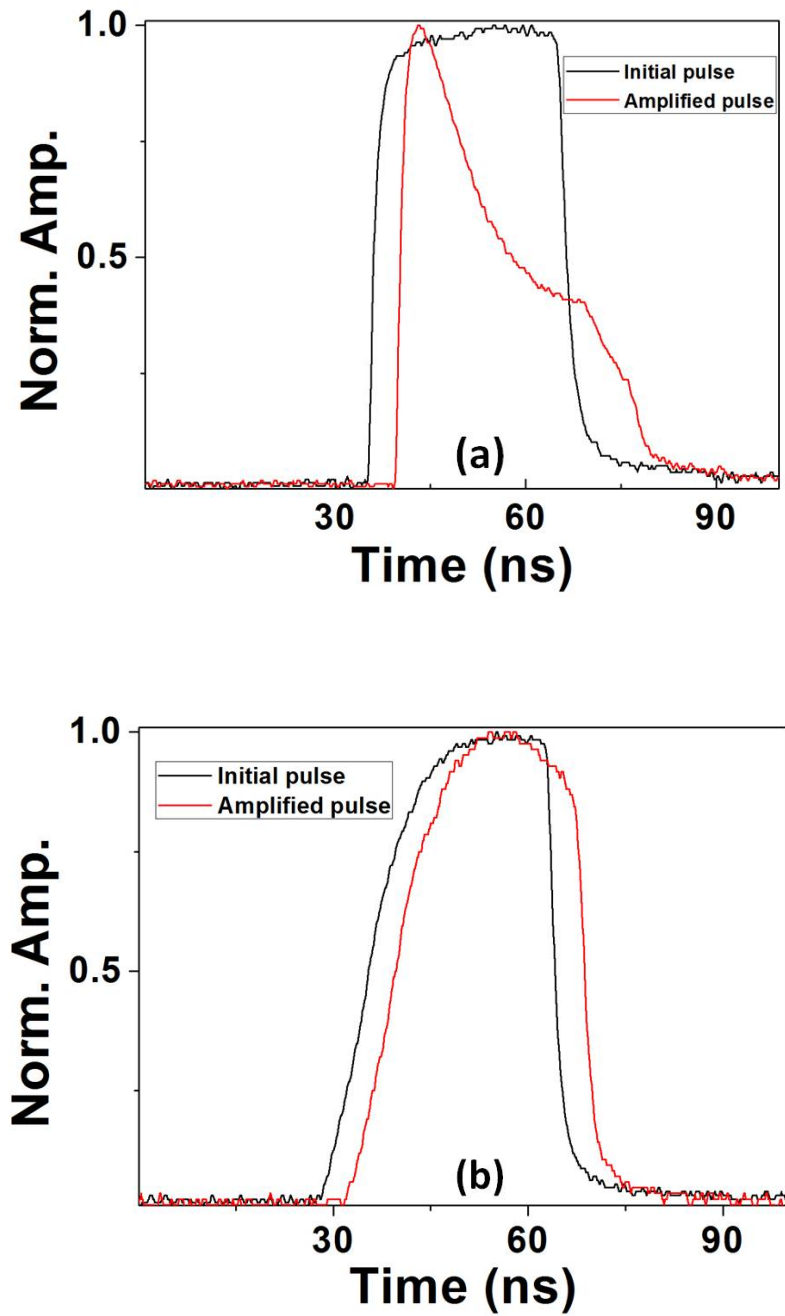


Fig. 2. 9 (a) Initial and amplified pulses (after the filter) for 30 ns (a) rectangular pulse, (b) pre-shaped pulse.

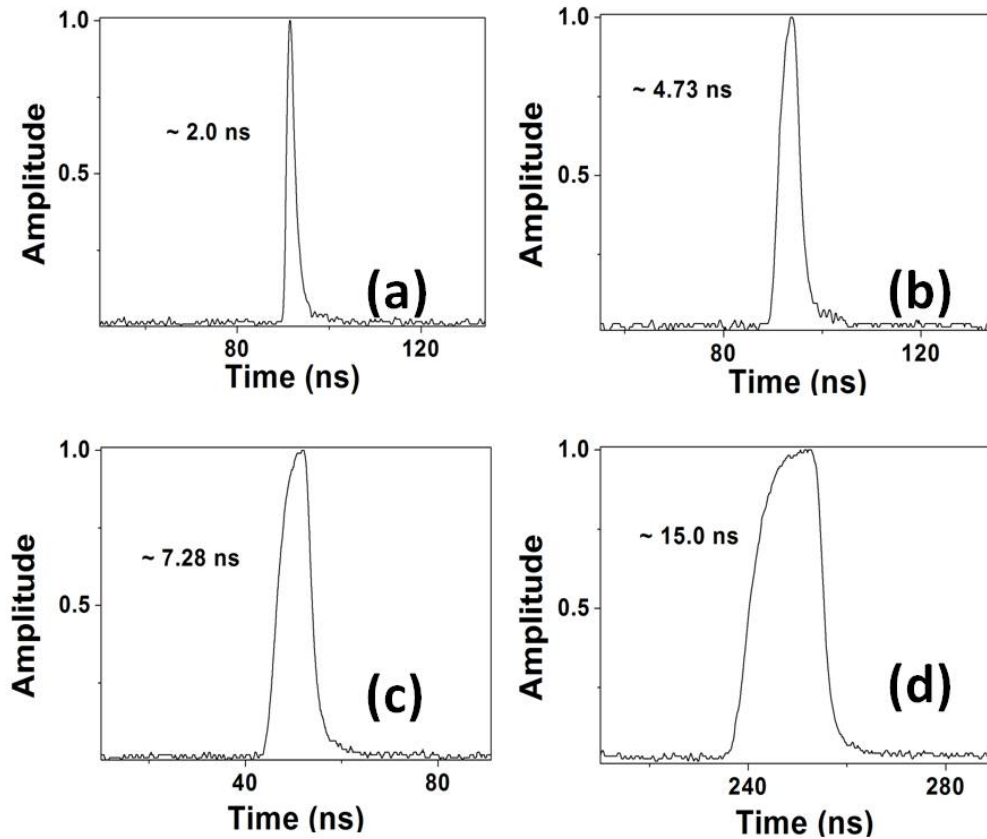


Fig. 2. 10 output pulses of pulse generation system shown in Fig. 2. 8 with different pulse duration.

## 2.5 Road-blocks for energy and power scaling of the single frequency nanosecond laser pulses in fiber amplifier

As mentioned above, high energy and high power single frequency nanosecond laser pulses have a myriad of applications, such as nonlinear frequency conversion,

LIDAR, etc. Such kind of pulses are usually achieved by amplifying one single frequency pulsed oscillator based on the MOPA configuration. The challenge with energy and power scaling is to preserve the desired seed laser properties during the amplification process in the face of the various deleterious effect including nonlinearities, gain saturation and thermal beam distortions, etc. Furthermore, it is also required to avoid all-fiber and components damage mechanisms. Several limits for power and energy scaling will be discussed in this section.

#### 2.5.1 Gain depletion over nanosecond period

As mentioned above, gain depletion over the time scale of the pulse always distorts the pulse shape in the fiber amplifier for ns pulses (see Fig. 2. 9 (a)) [145]. This will limit the further scaling of the pulse energy or average power.

#### 2.5.2 Nonlinearities

In a pulsed fiber amplifier, the pulse energy will transfer to other wavelengths by inelastic scattering due to either SRS or SBS when the peak power increases to certain level. And the linewidth of the laser may be broadened due to the nonlinear phase shift induced by self-phase modulation (SPM).

For the amplification of the narrow linewidth nanosecond pulses, the SBS is the main limit, which has lower threshold than SRS and SPM. The SBS was first observed in 1964 and has been studied extensively. On one hand, it is a deleterious effect in amplifier or optical transmission system. On the other hand, SBS can be utilized to build SBS lasers with ultra-narrow linewidth. SBS manifests through the generation of a Stokes wave

whose frequency is downshifted from that of the incident light by an amount set by the nonlinear medium. The spectral width of the SBS gain spectrum is very small ( $\sim 10$  MHz) because it is related to the damping time of acoustic waves related to the phonon lifetime [149].

The SBS threshold in the fiber is defined by Eq. 2.2,

$$P_t = \frac{21A_{eff}}{g_B L_{eff}} \quad (2.2)$$

where,  $A_{eff}$  is the effective mode field,  $L_{eff}$  is the effective length of the fiber,  $g_B$  is the peak value of the Brillouin gain given by Eq. 2.3,

$$g_B = \frac{8\pi^2 \gamma_e^2}{n_p \lambda_p^2 \rho_0 c \nu_A \Gamma_B} \quad (2.3)$$

where  $\gamma_e$  and  $\rho_0$  are the electrostrictive constant and the density of the material forming the core of the fiber, The full width at half maximum (FWHM) of the gain spectrum is related to  $\Gamma_B$  as  $\Delta\nu_B = \Gamma_B / (2\pi)$ . The phonon lifetime,  $T_B = \Gamma_B^{-1}$ , is typically  $< 10$  ns,  $n_p$  is the effective refractive index of the fiber,  $\lambda_p$  is the pump wavelength,  $c$  is the speed of light.  $g_B$  is in the range 3 to  $5 \times 10^{-11}$  m/W for silica fibers [146]. From Eq. (2.2), the threshold can be increased by increasing the mode-field area and decreasing the fiber length. So in our experiment, one large-core highly thulium doped germanate fiber was used to boost the pulse energy and average power.

### 2.5.3 Optical damage limit

When the peak power or pulse energy increase to certain level, fiber will be damaged. Stuart et al. investigated and defined bulk damage limits for pure fused silica [150]. In this paper, the bulk damage threshold  $P_{\max}$  for pulses with a duration  $\tau$  between 50 ps and 100 ns can be estimated via the following equation,

$$P_{\max} = I_{th} A_{eff} = \frac{XA_{eff}}{\sqrt{\tau}} \quad (2.4)$$

where  $X=150 \text{ GW ns}^{0.5}/\text{cm}^2=1.5 \text{ kW ns}^{0.5}/\mu\text{m}^2$ , and  $\tau$  is expressed in nanoseconds. This measurement was made at a wavelength of 1.06  $\mu\text{m}$ . For pulses longer than 10 ps, the damage is thermal in origin, with a limiting rate determined by heat diffusion from conduction band electrons to the lattice.

## 2.6 Energy scaling of the 2 $\mu\text{m}$ single frequency nanosecond pulses using large-core highly thulium-doped germanate fiber amplifier

Fig. 2. 11 demonstrates the diagram of the whole laser system based on the MOPA configuration including the pulse generation system (shown in Fig. 2. 8), one double-cladding fiber amplifier and one final power amplifier. The setup in the lab is shown in Fig. 2. 12.

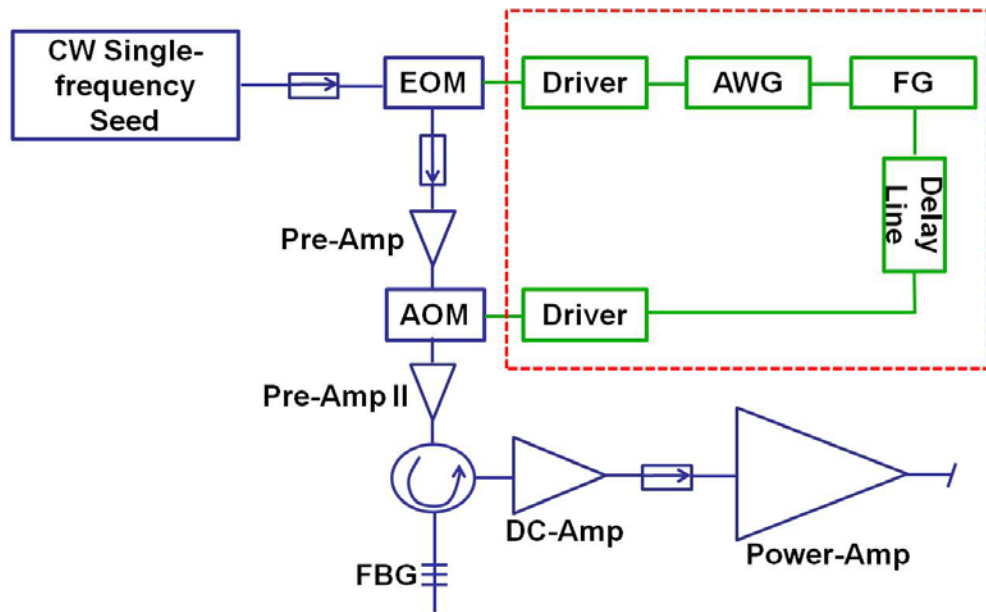


Figure 2. 11: Schematic of the pulsed MOPA-based system. AWG, arbitrary wave generator; FG, function generator.

~ 15 ns pulses are chosen to do the energy scaling. These pulses, output from the pulse generation system (shown in Fig. 2. 8), are put into an all-fiber chain of two double-cladding amplifier stages separated by inter-stage commercial fiber based PM isolator (provided by AFR). The first stage utilizes 2 meter commercial Tm-doped double-cladding fiber (from Nufern Inc.) with a ~10/130  $\mu\text{m}$  core/cladding. The pump are commercial fiber-pigtailed multimode diodes (from DILAS Inc.) at ~793 nm. The amplified pulses output from this double-cladding fiber amplifier are put into the final power amplifier using a piece of large core highly thulium doped germanate fiber. One commercial PM (6+1) $\times$ 1 signal pump combiner was used to combine the 2  $\mu\text{m}$  laser signal and the ~793 nm multimode pump. The output fiber of the combiner has 25/250

$\mu\text{m}$  core/cladding sizes. One end of the LC-TGF was fusion spliced to the output fiber of the combiner based on an asymmetric fusion splicing technique. The refractive index of the germanate glass in this wavelength is  $\sim 1.62$  and thus the reflection from the interface between the silica fiber and the germanate fiber can be calculated to be 0.3%. However, one isolator was spliced between the first-stage double-cladding fiber amplifier and the final germanate fiber amplifier to block any reflections. The fusion splice joint and the whole LC-TGF were fixed in a v-groove in a copper plate (see Fig. 2. 13) under fans for air cooling . A low index polymer was coated around the stripped fiber near fusion splice joint to confine the pump power in the inner cladding. The output end was angle-cleaved to reduce the feedback. The LC-TGF fiber was pumped from the input end with multimode diodes.

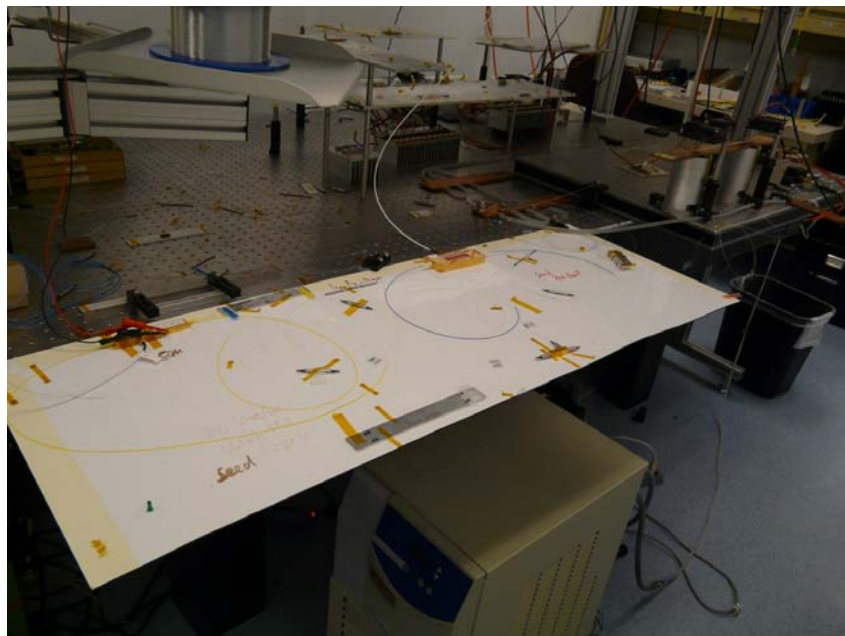


Fig. 2. 12 Laser system in the lab.

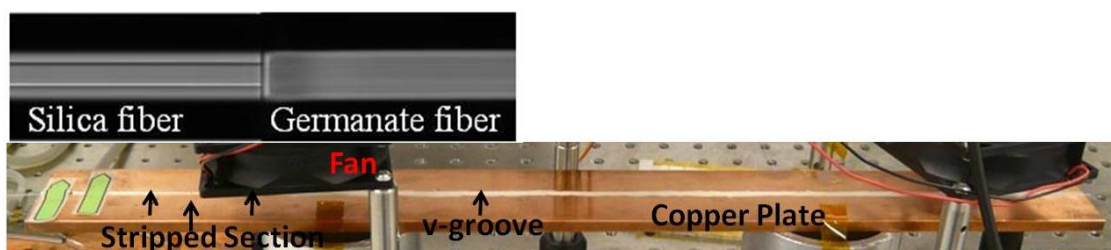


Fig. 2. 13 Large-core highly thulium-doped germanate fiber fixed in a copper plate. The inset shows the splice joint between the silica fiber and the germanate fiber.

~30 cm 25/250 $\mu$ m core/cladding highly Tm-doped germanate fiber was used in the final power amplifier to scale the pulse energy. In order to achieve the high pulse energy for the implemented MOPA-based system in Fig. 2. 11, firstly, we fixed the pump power as ~8 W and measured the pulse energy and average power at different repetition rate (from 10 Hz to 400 kHz) as shown in Fig. 2. 14. We used an Ophir PE9F-SH pyroelectric energy meter to measure the energy of the pulses with repetition rate up to 20 kHz. This pulse energy meter is insensitive to the ASE background and CW signal component. When the repetition rate of the pulses is higher than 20 kHz, the average power was measured. For pulses with such high repetition rates, the seed power is high enough to depress the ASE in the amplifier and thus the pulse energy can be calculated based on the measured average power. From Fig. 2. 14, one can see that the pulse energy does not change much when the repetition rate is increased from 10Hz to 500 Hz and the maximum pulse energy is achieved at 300Hz. After that, the pulse energy decreases inversely with the increase in the repetition rate. Correspondingly, the average power increases with the increase of the repetition rate, and then tends to become relatively

constant (saturation of the amplifier). When we changed the repetition rate and measured the pulse energies, the pulse shape was monitored at all repetition rates and the pulse duration kept at  $\sim 15$  ns. Although the lower repetition rate can get higher energy, the average power of the signal is small and thus may induce large backward ASE in the final amplifier stage under large pump level, which is detrimental to the multimode  $\sim 793$  nm laser diodes. So 5 kHz repetition rate pulses were chosen to scale the energy and peak power.

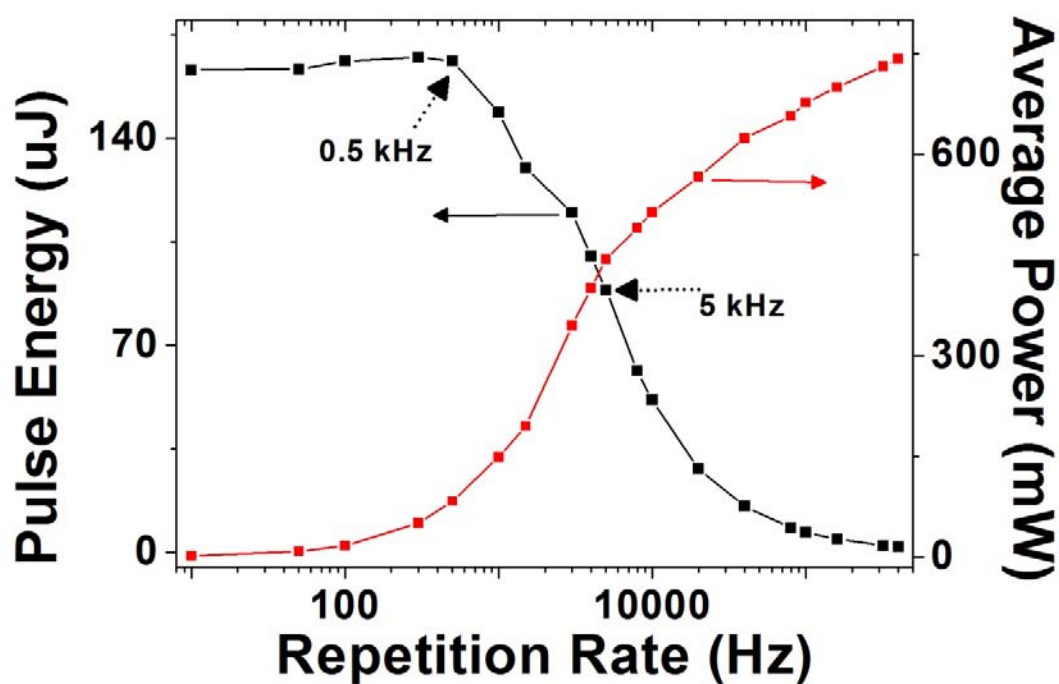


Fig. 2. 14 Pulse energy and average power versus repetition rate when the pump is fixed at  $\sim 8$  W.

Fig. 2. 15 shows the pulse energy and pulse peak power output from the final amplifier stage under different pump level for 5 kHz, ~15 ns pulses. One can see that the maximum pulse energy can be up to > 0.5 mJ, which is the reported highest pulse energy for a single frequency all fiber-based ~ 2  $\mu$ m fiber laser pulses, to the best of our knowledge. The highest average power is measured to be ~2.5 W. The pump power shown in Fig. 2. 15 is the power after the combiner. And the power conversion efficiency for the power amplifier stage is ~14.3%, which can be improved by optimizing the seed pulse condition and the length of the LC-TGF in the amplifier.

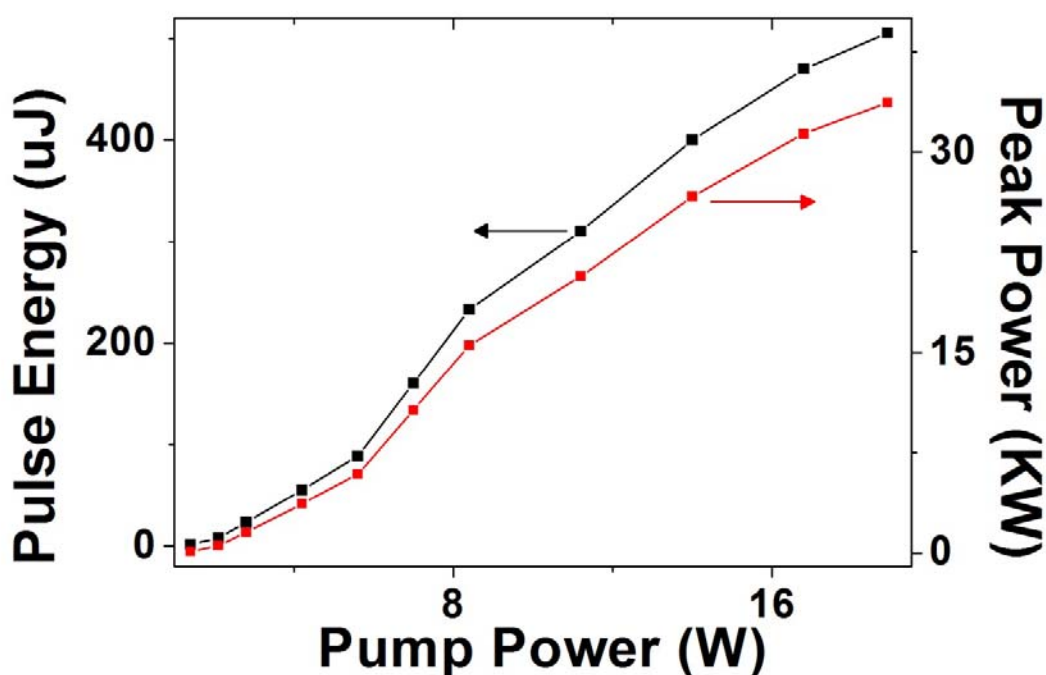


Fig. 2. 15 Measured pulse energy and peak power for the final power amplifier at different pump level when the repetition rate is fixed at 5kHz. The pump power shown here is the power after the combiner.

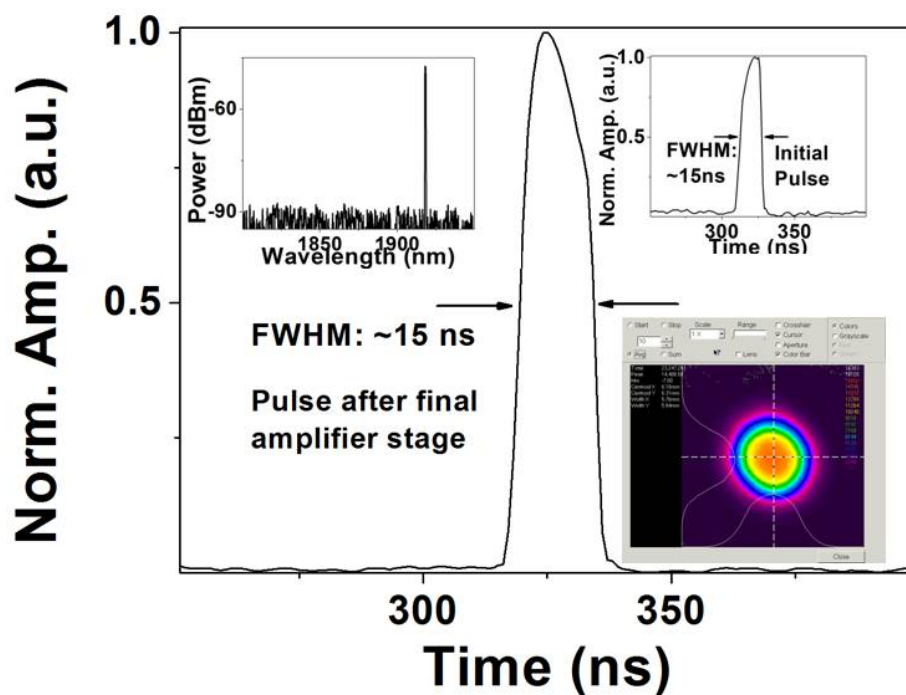


Fig. 2. 16. The typical pulse shape of the amplified pulses after the final amplifier. Insets: Initial pulse (EOM Modulated) shape; spectrum and the beam profile of the final amplified pulses.

The typical pulse shape for the high energy pulses ( $> 0.3$  mJ) from the final output is recorded by a fast detector and oscilloscope as shown in Fig. 2. 16. One inset of Fig. 2. 16 also shows the initial pulse shape before any amplification (after EOM). The front edge of the optical pulse is tailored to mitigate the effect of dynamic gain saturation due to the seriously steepening of the front edge. One can see that the pulse shape, compared with the initial pulse shape, has been controlled very well and still keeps a

good pulse shape after the final power amplifier stage owing to the effectively pre-shaping of the modulated pulses using the AWG. The pulse duration is still kept at  $\sim 15$  ns. So the maximum peak power is calculated to be  $>33$  kW (See Fig. 2. 15), which is 10 times more than the value of the reported single frequency transform-limited ns pulses in  $2\mu\text{m}$  region [77]. For the amplified pulses, the spectrum was measured using a modified optical spectrum analyzer (OSA) as shown in one inset of Fig. 2. 16. One can see that the signal to noise ratio is  $> 40$  dB from the spectrum. We also measured the  $M^2$  of the output pulses. The beam maintained single mode output, with an  $M^2$  of  $\sim 1.2$ . Output beam profile was also measured by using a Spiricon Pyrocam III (see inset in Fig. 2. 16). The pulses are linearly polarized and the extinction ratio was measured to be  $>13$  dB.

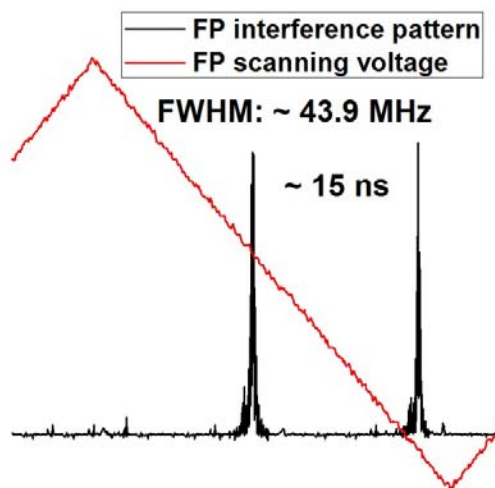


Fig. 2. 17 Interference pattern for high energy  $\sim 15$  ns pulses ( $> 300 \mu\text{J}$ ).

The linewidth of the amplified single frequency pulses was measured using a home-made scanning FP cavity. The setup of this FP cavity is shown in Fig. 2. 6 and described in Sec. 2. 3. The typical interference pattern of high energy  $\sim 15$  ns pulses ( $> 300 \mu\text{J}$ ) is shown in Fig. 2. 17. The linewidth was measured to be  $\sim 43.9$  MHz. So the linewidth of the  $\sim 15$  ns pulses does not change in the process of amplification and the amplified pulses are transform-limited.

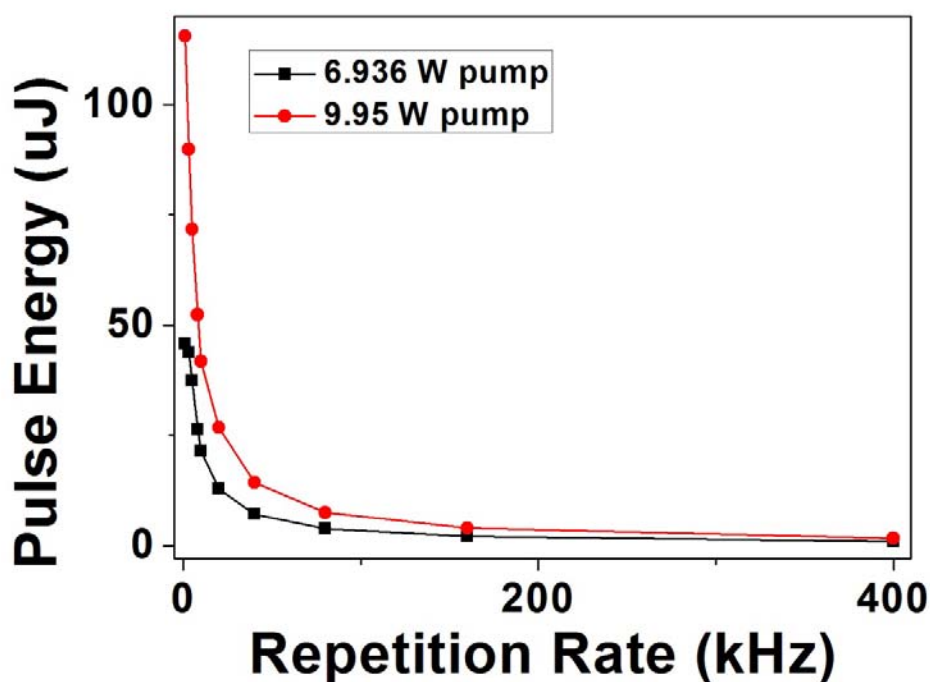


Fig. 2. 18 Pulse energy at different repetition rate when the pump power is fixed at 6.936 W pump and fixed at 9.95 W, respectively.

We also utilized  $\sim 41$  cm 30/300  $\mu\text{m}$  core/cladding thulium-doped germanate fiber in the final power amplifier to scale the energy of  $\sim 15$  ns pulses. The pulse energy at

different repetition rate was also investigated and shown in Fig. 2. 18. The pulse energy increases with the decrease of repetition rate. This time, we choose pulses at 1 kHz repetition rate to do the energy scaling. Because we do not care about the ASE this time and just want to boost the pulse energy as much as possible. Nearly  $\sim 1$  mJ pulse energy was achieved as shown in Fig. 2. 19. The energy was measured by an Ophir PE9F-SH pyroelectric energy meter with repetition rate up to 10 kHz.

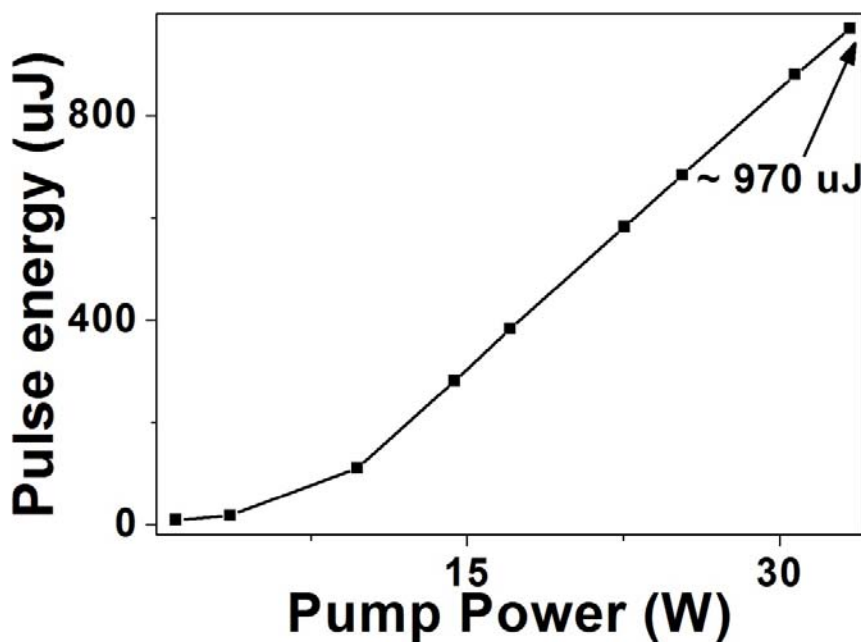


Fig. 2. 19 Pulse energy at different pump level for  $\sim 15$  ns pulses at 1 kHz repetition rate.

### 2.7 Power scaling of the $2 \mu\text{m}$ single frequency nanosecond pulses.

In the power scaling, we used  $\sim 41$  cm  $30/300 \mu\text{m}$  core/cladding thulium-doped germanate fiber in the final power amplifier. In order to get the high power and high peak

power at the same time, we choose to amplify the shortest generated pulse ( $\sim 2.0$  ns shown in Fig. 2. 10) at high repetition rate (100 kHz to 500 kHz). This high repetition rate enables enough power (9.2 mW @ 100 kHz, 19.3 mW @ 300 kHz, 25.7 mW @ 500 kHz), output from the pulse generation system (shown in Fig. 2. 8), to seed the first DC-amplifier. After the first DC-amplifier, the power was amplified to  $\sim 350$  mW,  $\sim 420$  mW,  $\sim 450$  mW for 100 kHz, 300 kHz, 500 kHz repetition rate, respectively and no nonlinearities were observed from their spectrum.

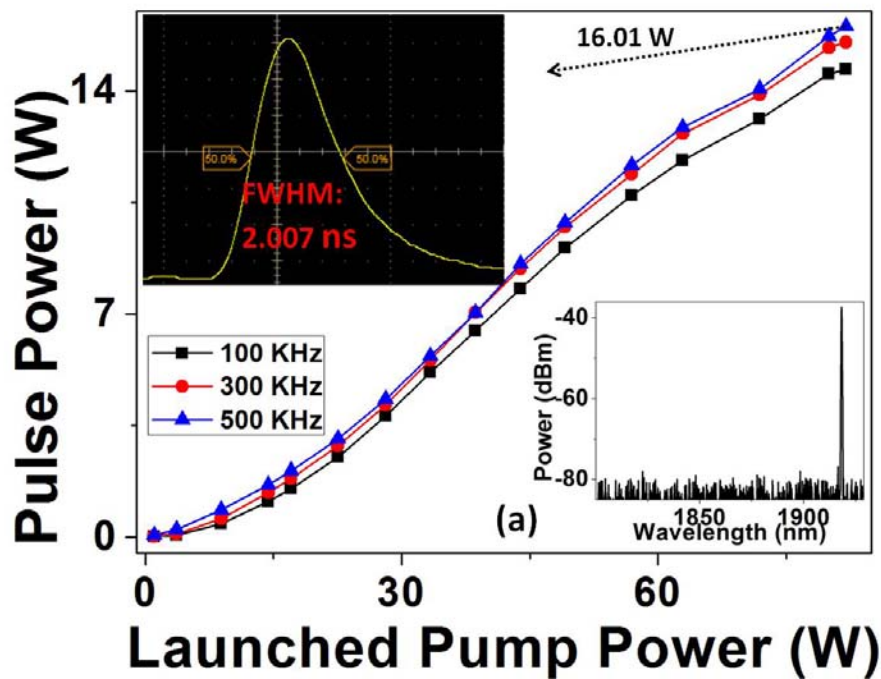


Fig. 2. 20 (a) Average power of the pulse under different pump level. Inset: Pulse shape and spectrum when the power is  $\sim 16.01$  W.

Fig. 2. 20 (a) shows the output power of the final large-core Tm-doped germanate fiber amplifier under different pump levels at three different repetition rates. The maximum average power of 16.01 W was achieved at 500 kHz repetition rate. This is the highest average power for all fiber based single frequency nanosecond pulses in the 2  $\mu\text{m}$  regime. There is no big difference for pulses at the three repetition rates (100 kHz, 300 kHz and 500 kHz), which means the seed has already saturate the power amplifier. The pump power shown in Fig. 2. 20 (a) is the power after the combiner. The power conversion efficiency for the power amplifier stage is  $\sim 17.1\%$  in respect to the launched pump power (after the combiner). The pulse shape for the high power pulses (at  $\sim 16.01$  W) from the final output is recorded by a fast detector and one oscilloscope as shown in Fig. 2. 20 (a). The pulse keeps a good shape and the pulse duration is  $\sim 2.0$  ns. For the amplified pulses, the spectrum was measured using a modified optical spectrum analyzer (OSA) as shown in one inset of Fig. 2. 20 (a). One can see that the signal to noise ratio (SNR) is  $> 40$  dB from the spectrum. The good pulse shape and  $>40$  dB SNR in spectrum domain ensure that the peak power can be calculated using average power and repetition rate shown in Fig. 2. 20 (b), which was calibrated by a fast pulse energy meter when the repetition rate was below 20 kHz. The maximum of  $\sim 73.1$  kW peak power was achieved, which is also the reported highest peak power of all fiber single frequency laser source in the 2  $\mu\text{m}$  regime. The scanning Fabry-Perot interferometer was utilized to measure the spectra of our single frequency laser pulses at high power regime. The inset in Fig. 2. 20 (b) shows the typical Fabry-Perot scanning spectra of the  $\sim 2$  ns pulses with over 10 W average power. The linewidth was measured to be  $\sim 277$  MHz and thus these pulses are

transform limited. Fig. 2. 20 (c) demonstrates the  $M^2$  measurement and the beam profile measured by using a Spiricon Pyrocam III. The beam maintained single mode output, with an  $M^2$  of  $\sim 1.29$  in x-axis and 1.48 in y-axis, which depends on the splice.

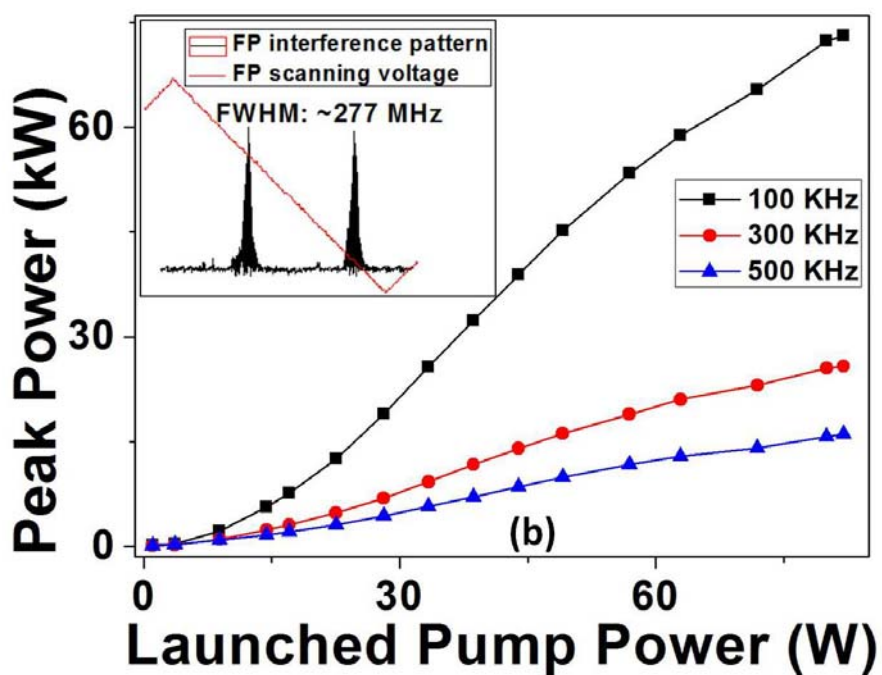


Fig. 2. 20 (b) Peak power of the pulse under different pump level. Inset: Fabry-Perot scanning spectra of the  $\sim 2$  ns pulses (over 10 W average power).

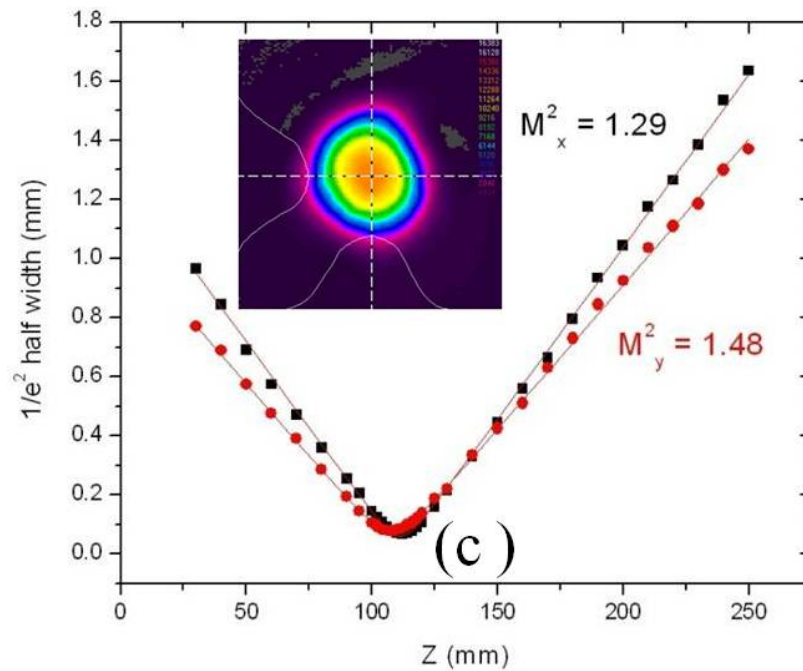


Fig. 2. 20 (C)  $M^2$  measurement and beam profile for amplified output pulses.

## 2.8 Modeling the pulsed double-cladding thulium doped germanate fiber amplifier

Here we present a numerical model for the pulsed large core thulium-doped germanate double cladding fiber amplifier (LC-TG-DC-FA). Through this model, we can calculate pump and signal evolution, pulse shape evolution, stored energy, ASE dependence on the pump power, seed power, repetition rate, etc. These results can give us guidance to optimize the amplifier to extract maximum pulse energy and pulse average power.

### 2.8.1 Rate equations and Propagation equations

Fig. 2. 21 shows the energy level diagram of  $\text{Tm}^{3+}$  in germanate glass [144]. The  ${}^3H_6-{}^3H_4$  transition corresponds to the 793-nm pump band and the  ${}^3F_4-{}^3H_6$  transition corresponds to the signal band near 2  $\mu\text{m}$ . The well-known  ${}^3H_4-{}^3F_4$  cross-relaxation effect [144] and the inverse cross-relaxation effect were taken into account in the presented model. The core of the model routines are a set of rate equations and propagation equations for laser signal, ASE and pump [151] as shown in the following,

$$\frac{\partial N_3}{\partial t} = W_{03}N_0 - \frac{1}{\tau_{31}}N_3 - K_{3011}N_3N_0 + K_{1130}N_1^2 \quad (1)$$

$$\frac{\partial N_1}{\partial t} = W_{01}N_0 - W_{10}N_1 - \frac{1}{\tau_{10}}N_1 + \frac{1}{\tau_{31}}N_3 + 2K_{3011}N_3N_0 - 2K_{1130}N_1^2 \quad (2)$$

$$\frac{\partial N_0}{\partial t} = -W_{03}N_0 - W_{01}N_0 + W_{10}N_1 + \frac{1}{\tau_{10}}N_1 - K_{3011}N_3N_0 + K_{1130}N_1^2 \quad (3)$$

$$\left(\frac{1}{V_s} \frac{\partial}{\partial t} + \frac{\partial}{\partial z}\right) P_s(z, t) = \{\Gamma_s[\sigma_{10}(v_s)N_1(z, t) - \sigma_{01}(v_s)N_0(z, t)] - \alpha_{\text{loss-signal}}\} P_s(z, t) \quad (4)$$

$$\left(\frac{1}{V_{\text{ASE}}} \frac{\partial}{\partial t} + \frac{\partial}{\partial z}\right) P_{\text{ASE}}^{(+,-)}(v_i, z, t) = \{\Gamma_s[\sigma_{10}(v_i)N_1(z, t) - \sigma_{01}(v_i)N_0(z, t)] - \alpha_{\text{loss-signal}}\} P_{\text{ASE}}^{(+,-)}(v_i, z, t) + \Gamma_s \sigma_{10}(v_i)N_1(z, t)P_0 \quad (5)$$

$$\left(\frac{1}{V_p} \frac{\partial}{\partial t} + \frac{\partial}{\partial z}\right) P_p(z, t) = [-\sigma_{03}(v_p)N_0(z, t) - \alpha_{\text{loss-pump}}] P_p(z, t) \quad (6)$$

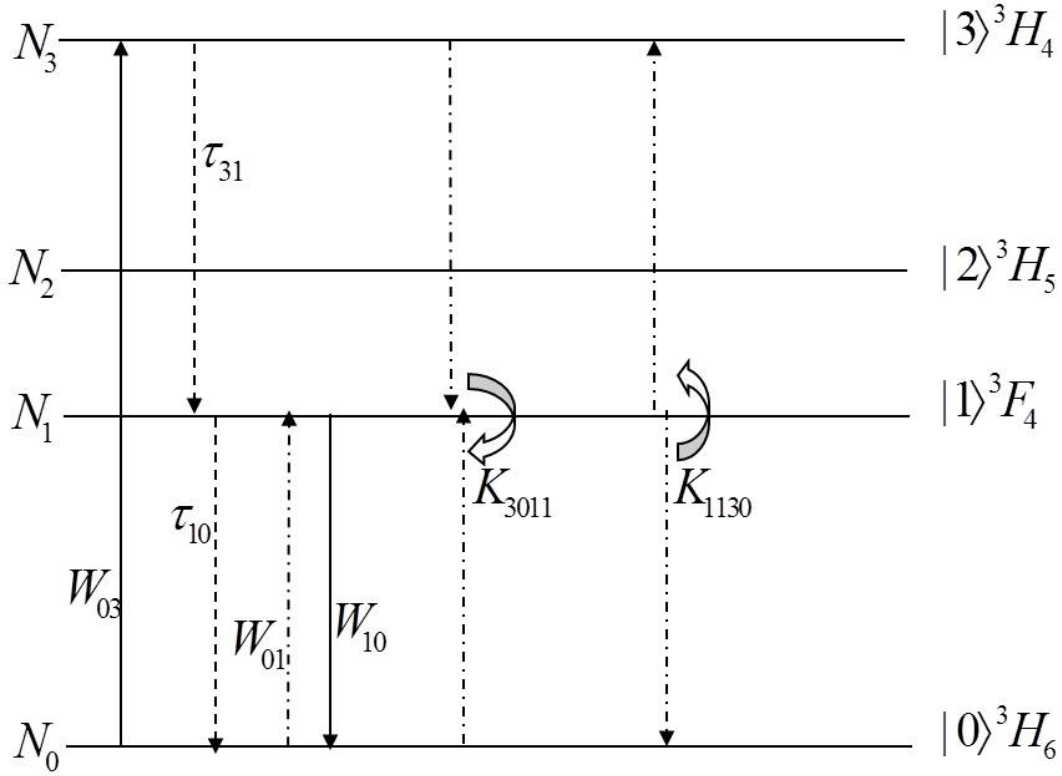


Fig. 2. 21 Energy levels and transitions taken into account in the presented model for  $\text{Tm}^{3+}$  in germanate glass.

Here,  $N_j$  is the population of the  $j$ th level in the energy diagram shown in Fig. 2. 21.  $\tau_{31}$  and  $\tau_{10}$  are the lifetime of the thulium ions.  $K_{3011}$  and  $K_{1130}$  are cross relaxation rate and inverse cross relaxation rate, respectively.  $\Gamma_s$  is the overlap factor of the single-mode signal field and is assumed to be the same for all signal ASEs.  $\Gamma_p$  is the overlap factor of the multi-mode pump field.  $V_s$ ,  $V_p$  and  $V_{\text{ASE}}$  are group velocity of laser signal, pump and ASE.  $\sigma_{01}$  and  $\sigma_{10}$  are the absorption and emission cross sections of thulium

ions from the first  ${}^3\text{H}_6$  level to the second  ${}^3\text{F}_4$  level (see Fig. 2. 21).  $\sigma_{03}$  is the absorption cross section of thulium ions from the first  ${}^3\text{H}_6$  level to the fourth  ${}^3\text{H}_4$  level (see Fig. 2. 21). These spectroscopic parameters (cross sections, life time, etc.) of the thulium ions in germanate glass are obtained from ref. [144].  $\alpha_{loss-signal}$  is the propagation loss of the laser signal in the Tm-doped germanate fiber and was measured to be  $\sim 5$  dB/m.  $\alpha_{loss-pump}$  is the pump propagation loss in the fiber and was estimated to be  $\sim 5$  dB/m. The propagation loss of the ASE (1600nm to 2000 nm) is assumed to be same with that of the laser signal.  $P_0(\lambda) = 2hc^2 / \lambda^3$  represents the contribution of the spontaneous emission into the mode.  $W_{01}$ ,  $W_{10}$  and  $W_{03}$  are light-induced transition rates for laser signal and pump and can be given as follows [148],

$$W_{01} = \Gamma_s \left\{ \frac{\sigma_{01}(\nu_s) P_s(z, t)}{h \nu_s A} + \sum_i \frac{\sigma_{01}(\nu_i) [P_{ASE}^{(+)}(\nu_i, z, t) + P_{ASE}^{(-)}(\nu_i, z, t)]}{h \nu_i A} \right\} \quad (7)$$

$$W_{10} = \Gamma_s \left\{ \frac{\sigma_{10}(\nu_s) P_s(z, t)}{h \nu_s A} + \sum_i \frac{\sigma_{10}(\nu_i) [P_{ASE}^{(+)}(\nu_i, z, t) + P_{ASE}^{(-)}(\nu_i, z, t)]}{h \nu_i A} \right\} \quad (8)$$

$$W_{03} = \Gamma_p \frac{\sigma_{03}(\nu_p) P_p(z, t)}{h \nu_p A} \quad (9)$$

One program was developed based on these equations mainly using 4th order Runge-Kutta method and split step Fourier method (SSFM) [146]. It should be noted that pulses with Gaussian shape were utilized in this model. Some important parameters are listed in Table 2.1. The life time for  ${}^3\text{F}_4$  energy level was measured [144]. The measured life time for  ${}^3\text{H}_4$  energy level was estimated to be  $\sim 0.06$ ms according to the measured related data in tellurite [144] and ZBLAN glass [152]. And the cross-relaxation Rate can be calculated through Eq. 2. 5 [149],

$$\frac{1}{\tau_{\text{measured}}} = \frac{1}{\tau_{\text{intrinsic}}} + K_{3011}N_0 \quad (2.5)$$

Where  $\tau_{\text{measured}}$ ,  $\tau_{\text{intrinsic}}$  are the measured and the intrinsic lifetime of the thulium ions in  ${}^3\text{H}_4$ .

Parameters	Value
Thulium Ions Concentration (/m <sup>3</sup> )	5.2*10 <sup>26</sup>
Life time for ${}^3\text{F}_4$ energy level (ms)	2.5
Intrinsic Life time for ${}^3\text{H}_4$ energy level (ms)	0.36
Measured Life time for ${}^3\text{H}_4$ energy level (ms)	0.06
Cross-relaxation Rate (m <sup>3</sup> /s)	26.7094*10 <sup>-24</sup>
Core-size ( $\mu\text{m}$ )	25 or 30
Cladding- size ( $\mu\text{m}$ )	250 or 300
Numerical Aperture	0.054

Table 2.1 Parameters used in modeling for LC-TG-DC-FA.

### 2.8.2 Pulse energy and average power calculation in the LC-TG-DC-FA

In the process of simulation, the signal pulse is a Gaussian pulse with a 15ns width (full-width at half-maximum). When a signal pulse passes through the large-core thulium-doped germanate fiber, it will consume the upper-level ( ${}^3\text{F}_4$  shown in Fig. 2. 21) population, grow along the fiber and finally become a giant pulse. A portion of the energy stored in the gain fiber is extracted out during this process, while the pump continuously supplies the stored energy.

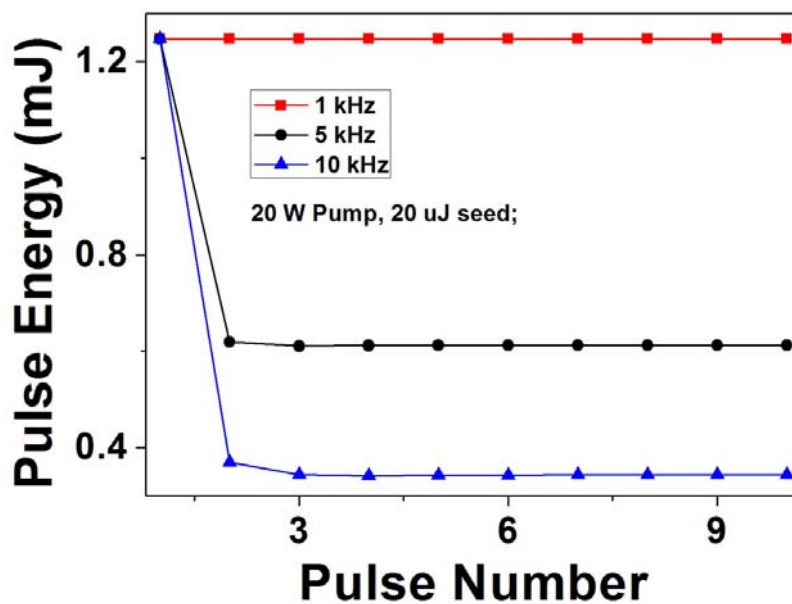


Fig. 2. 22 Output pulse energy from the fiber amplifier for the first entering ten pulses.

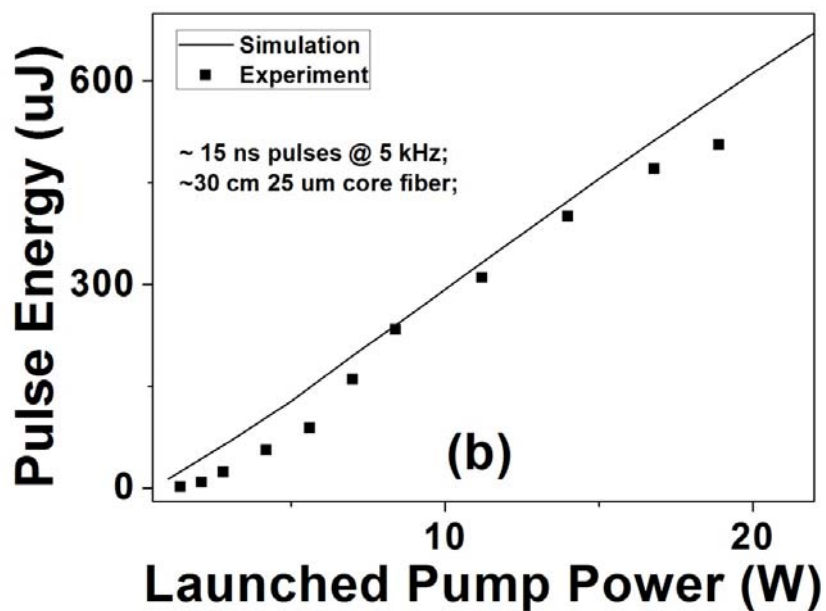


Fig. 2. 23 Calculated and measured pulse energy

Fig. 2. 22 shows the output pulse energy of the first ten entering pulses under 20 W pump. Note that the pulse energy of the seed entering the amplifier is 20  $\mu\text{J}$ . The active fiber used here is  $\sim 30\text{cm}$  25/250  $\mu\text{m}$  core/cladding Tm-doped germanate fiber. From Fig. 2. 22, we could find that the calculated energy for the first pulse is obviously higher than that of the following pulses. It is because that a lot of ions are excited to the upper laser level by the pump and huge population inversion is achieved before the first pulse entering the amplifier. So the first pulse experiences huge gain. However, the pulse energy becomes stable soon with more pulses entering the amplifier.

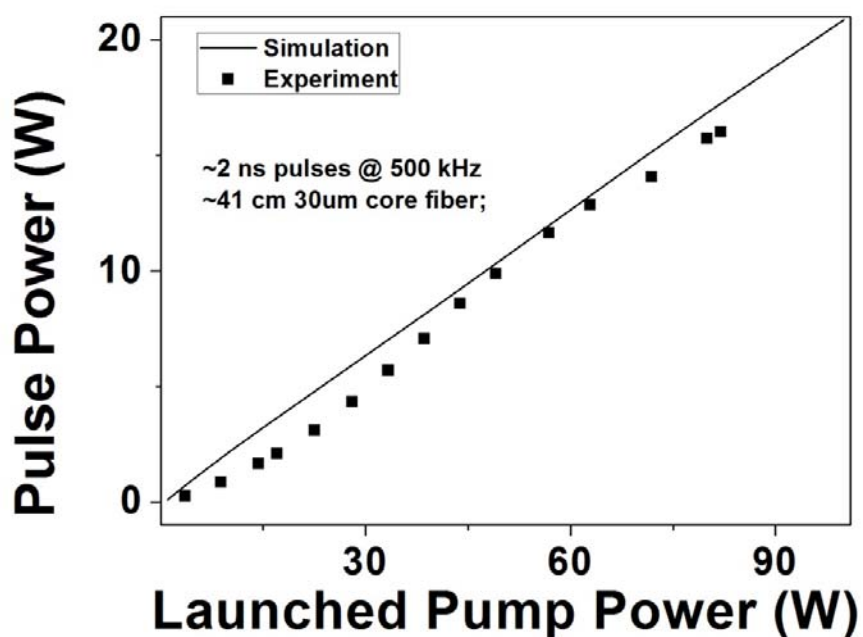


Fig. 2. 24 The measured and calculated average power of 2 ns pulses at 500 KHz repetition rate.

Then we calculated the output pulse energy from the amplifier under different pump level for 20  $\mu\text{J}$  ~ 15 ns pulses at 5 KHz repetition rate. As shown in Fig. 2. 23, a good agreement between the calculated and measured data is achieved. We also calculated the average power of the 2 ns pulses at 500 repetition rate and compared with the measured data as shown in Fig. 2. 24. They also matched very well. These results verify the validity of our model.

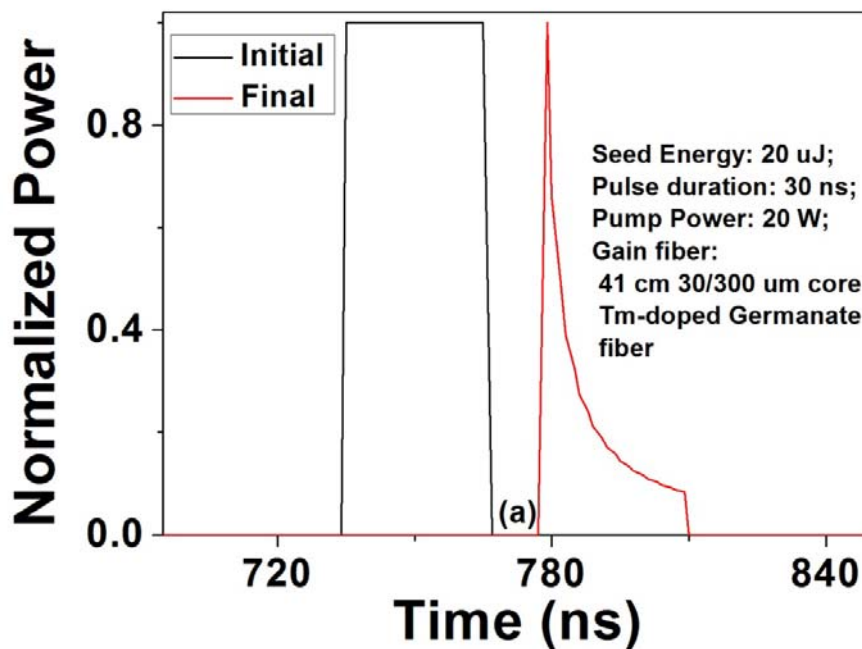


Fig. 25 (a) Pulse evolution in the amplifier for rectangular pulse.

### 2.8.3 Pulse shape evolution in the LC-TG-DC-FA

As mentioned in Sec. 2.4, the pulse distortion will be induced due to the gain depletion in the process of amplifying nanosecond pulses. Here, using the model, we theoretically calculate the pulse evolution for different pulse shapes in the amplifier. Fig. 2. 25 demonstrates the initial and amplified pulse shapes for rectangular and gaussian pulse. We can find that heavy pulse distortion happens for rectangular pulse. However, gaussian pulse keeps a good shape. The model can be utilized to design the initial pulse shape to get certain kind of pulse shape after the amplifier. For example, Fig. 2. 25 (c) shows a kind of rectangular pulse output from the amplifier by designing the shape of the input pulse.

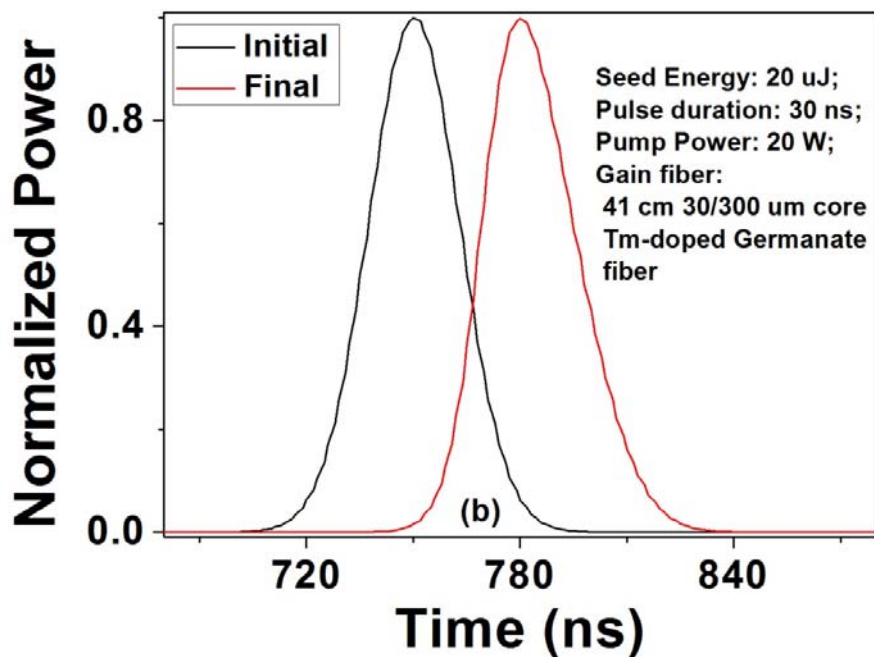


Fig. 25 (b) Pulse evolution in the amplifier for gaussian pulse.

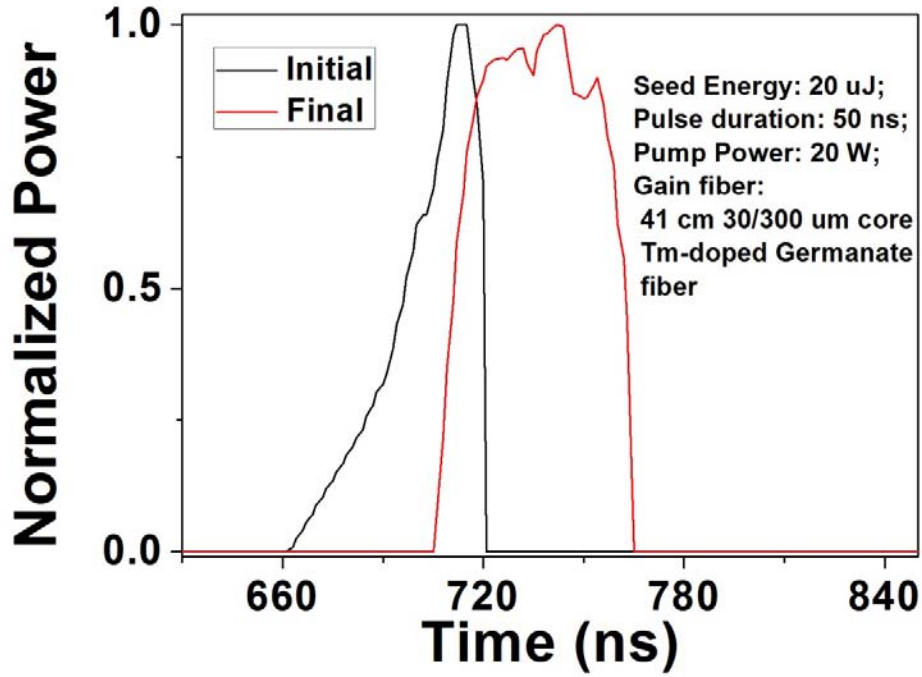


Fig. 2. 25 (c) Rectangular pulse output from the amplifier.

#### 2.8.4 Stored energy in the LC-TG-DC-FA

Using this model, we investigate how to extract more pulse energy from a piece of active fiber. We calculate the stored pulse energy in the thulium-doped germanate fiber defined by

$$E_s(t) = h\nu_s A \int_0^L N_1(z, t) dz \quad (10)$$

where  $\nu_s$  is the frequency of the laser signal,  $A$  is the core area and  $L$  is the length of the active fiber. Fig. 2. 26 (a), (b) demonstrates the stored pulse energy in a ~41 cm LC-TGF

with a 30  $\mu\text{m}$ -diameter core at different repetition rate under 20 W and 35 W pump, respectively. Note that the seed pulse was  $\sim 15$  ns Gaussian pulse with 20  $\mu\text{J}$  pulse energy.

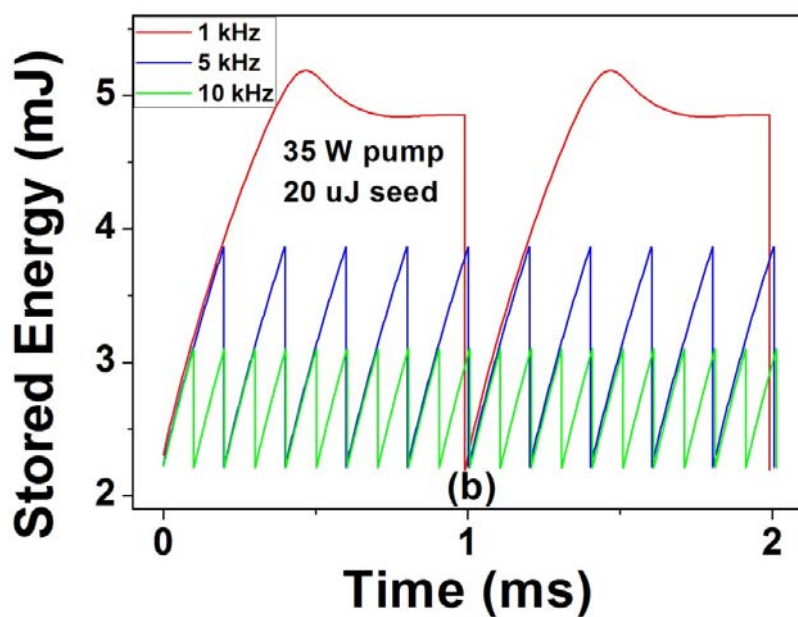
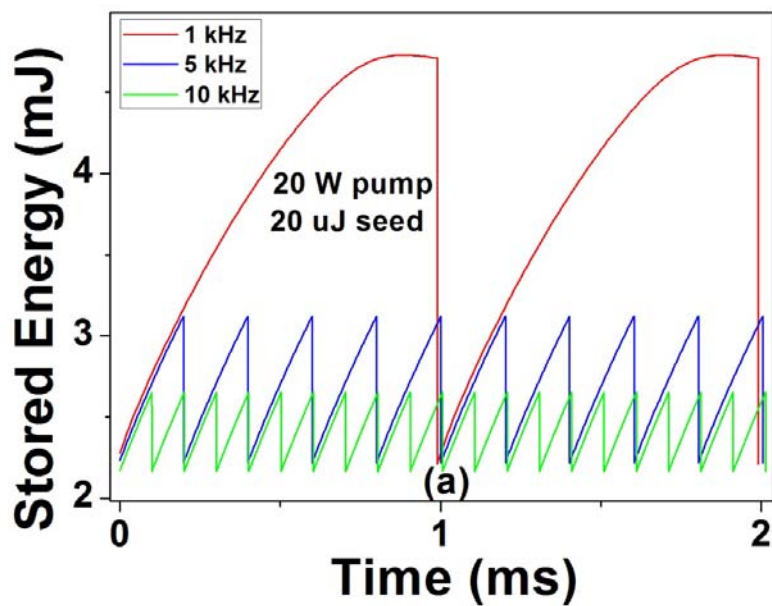


Fig. 2. 26 The stored energy in the active fiber for seed pulses at different repetition rate under (a) 20 W and (b) 35 W pump when the seed energy is fixed at 20  $\mu$ J.

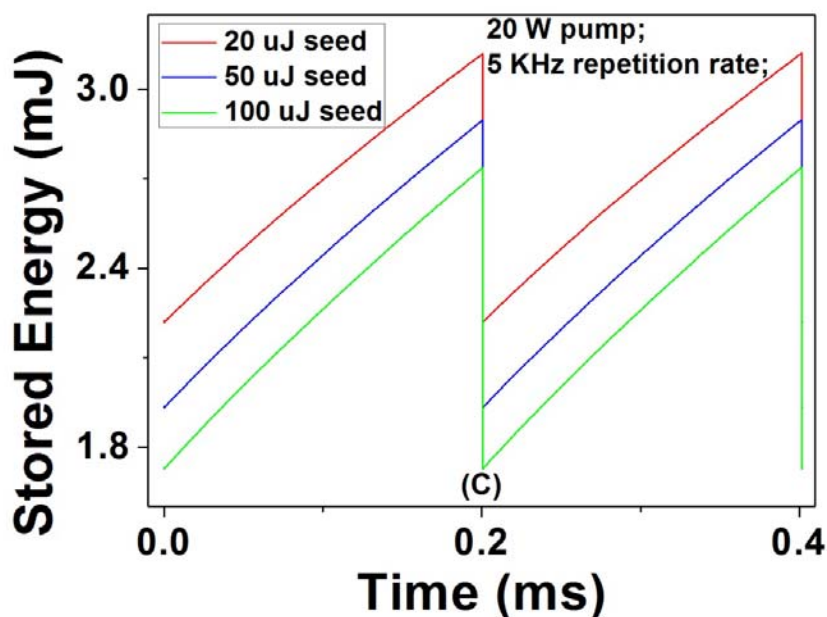


Fig. 2. 26 (c) Stored pulse energy in the active fiber for different seed energy when the pump and repetition rate are fixed at 20 W and 5 KHz, respectively.

Fig. 2. 26 (c) shows the dependence of stored energy on the seed energy. The pump and repetition rate are fixed at 20 W and 5 KHz, respectively. When the pump was launched into the active fiber, the electrons in the ground state will be excited into the upper laser energy level and thus the energy will be stored there. When a pulse propagates through the active fiber, the stored energy was extracted by the pulse and thus drops to its minimum, then starts to grow almost linearly with the time and the slope is dependent on the pump power and almost independent of repetition rate. The sharp

energy drop, shown in Fig. 2. 26, is the theoretically extracted pulse energy. It depends on repetition rate, pump power and seed energy. Specifically, when pump power and seed energy are fixed, lower repetition rate leads to more stored energy and more extracted energy; When repetition rate and seed energy are fixed, higher pump power enables more stored energy and more extracted energy; when repetition rate and pump power are fixed, higher seed energy leads to less stored energy but more extracted energy. It should be noted that, when the repetition rate was lowered to certain value under high pump level, some stored energy will be lost to the induced ASE ( the rolling over of the stored energy shown in Fig. 2. 26 (b) for 1 kHz cases).

We also investigate the dependence of the stored energy on the pulse duration. Fig. 2. 26 (d) shows the stored energy for 1 $\mu$ s and 15ns seed pulse and their seed energy are 20  $\mu$ J. We could find that the stored energy is dependent on the seed energy rather than the pulse duration.

These calculation on the stored energy can provide guidance to choose suitable pump power, seed energy and repetition rate to achieve higher pulse energy given a piece of active fiber.

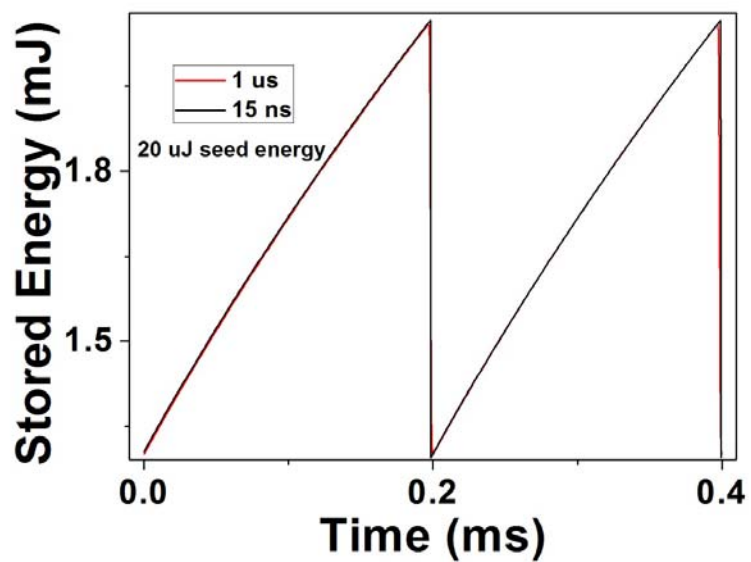


Fig. 2. 26 (d) The stored energy for 1us and 15 ns seed pulses with 20 μJ pulse energy.

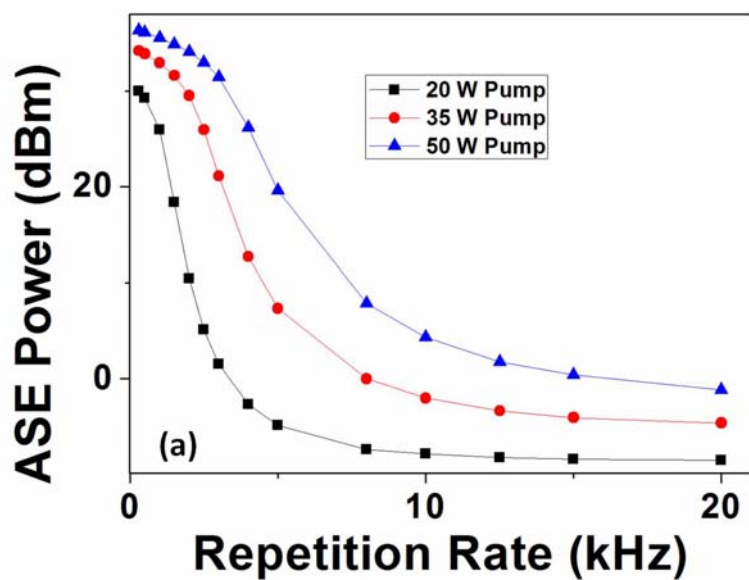


Fig. 2. 27 (a) ASE for pulses at different repetition rate.

### 2.8.5 ASE power dependence on the pump power, seed power and repetition rate

Then we investigate the ASE dependence on repetition rate, pump power and seed power as shown in Fig. 2. 27. Fig. 2. 27 (a) shows the ASE power at different repetition rate when the seed power is fixed at 100 mw for 15ns pulse at 5 kHz repetition rate. We can find that there is a critical repetition rate where the ASE significantly drops. (At the lower repetition rate, the ASE power becomes very large and tends to saturate. This saturation may result from the depletion of the gain). These results can help us to design and estimate the performance of a pulsed fiber amplifier. For example, if our goal is to achieve highest pulse energy, we should choose a low repetition rate and simultaneously consider the highest pump level we can apply without heavy ASE at such a low repetition rate. From Fig. 2. 27, compared with seed power, pump power and repetition rate have more significant affect on the ASE.

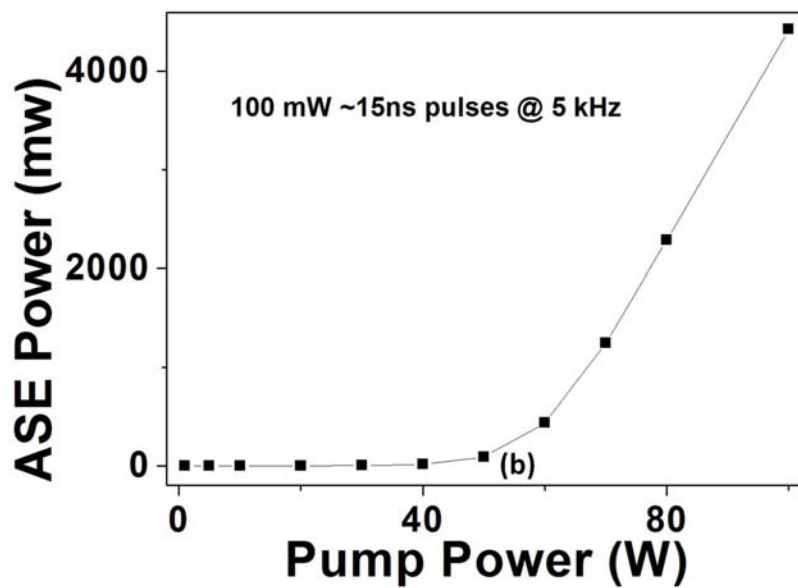


Fig. 2. 27 (b) ASE at different pump level.

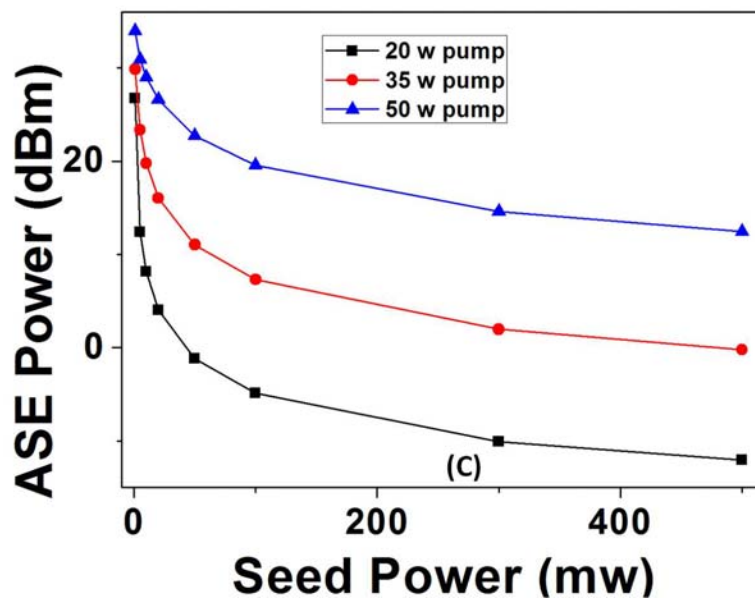


Fig. 2. 27 (c) ASE for different seed power.

## 2.9 Summary

In this chapter, the basics of the thulium ions doped in germanate glass and the theory of the cross-relaxation are reviewed. Then we describe a high power and high energy all-fiber-based single frequency nanosecond pulsed laser system operating at 2  $\mu\text{m}$ . This system can produce:

1. Half-mJ single frequency transform-limited  $\sim 15$  ns pulses at 5 kHz repetition rate by using 25/250  $\mu\text{m}$  core/cladding Tm-doped germanate fiber.
2. Nearly one mJ single frequency transform-limited  $\sim 15$  ns pulses at 1 kHz repetition rate by using 30/300  $\mu\text{m}$  core/cladding Tm-doped germanate fiber;
3. Single frequency transform-limited  $\sim 2$  ns pulses with over 16 W average power for 500 kHz repetition rate case and with 73.1 kW peak power for 100 kHz repetition rate case by using 30/300  $\mu\text{m}$  core/cladding Tm-doped germanate fiber.

One model is also developed to simulate the pulsed thulium doped double-cladding germanate fiber amplifier. The model can be utilized to calculate the pulse energy, average power, stored energy in the active fiber, the ASE dependence on the pump power, repetition rate and seed energy, etc. A good agreement is achieved between the calculated and measured data. The model can provide us guidance to design and optimize the pulsed highly thulium doped double-cladding germanate fiber amplifier.

## CHAPTER 3

### TERAHERTZ GENERATION USING 2 $\mu\text{m}$ HIGH POWER AND HIGH ENERGY SINGLE FREQUENCY NANOSECOND PULSES

#### 3.1 Introduction

In this chapter, we will report a coherent terahertz source generated by mixing two 2  $\mu\text{m}$  high energy single frequency transform-limited nanosecond pulses, output from two large-core highly thulium-doped germanate fiber amplifier, in a quasi-phase-matched gallium-arsenide (GaAs).

We also built a model for a collinear terahertz parametric oscillator (TPO), using the quasi-phase-matched GaAs in the cavity as the nonlinear medium, which was pumped by 2  $\mu\text{m}$  high energy single frequency transform-limited nanosecond pulses. The threshold of this TPO was investigated for different length of the crystal.

At last, we proposed a TPO pumped by a cavity enhanced 2  $\mu\text{m}$  high energy single frequency transform-limited nanosecond pulses. The enhancement factor of pulses in the cavity was numerically investigated.

#### 3.2 Gallium Arsenide (GaAs) crystal

Vodopyanov developed a figure of merit (FOM) based on THz loss, nonlinear coefficient and the index of refraction at the pump frequency to help to choose a nonlinear crystal for THz generation [153]. The FOM is given by  $\text{FOM} = (d_{\text{eff}}^2/n_{\text{opt}}^2)/\alpha_{\text{THz}}$ , where  $d_{\text{eff}}$ ,  $n_{\text{opt}}$  and  $\alpha_{\text{THz}}$  are nonlinear coefficient, the optical pump refraction index and THz loss, respectively. In Table 3.1, we list the linear optical properties, nonlinear optical properties, and figures of merit (normalized to  $\text{LiNbO}_3$ ) of several popular crystals used

for THz generation [153]. We can find that LiNbO<sub>3</sub> has highest nonlinear coefficient but it has very high loss for THz wave. In contrast, GaAs has very low THz absorption and thus it has comparable FOM with that of the LiNbO<sub>3</sub>. And compared with other crystal, GaAs has highest FOM. So in our experiment, GaAs is chosen as the nonlinear medium for THz generation.

Crystal	GaAs	GaP	ZGP	GaSe	LiNbO <sub>3</sub>
Optical Wavelength ( $\mu\text{m}$ )	2.1	1.06	2.1	1.06	1.06
$n_{\text{opt}}$	3.33	3.11	3.15	2.8	2.16
$\alpha_{\text{THz}} (\text{cm}^{-1})$	1	3.3	1	2.5	21.7
Nonlinear coefficient ( $\text{pm/V}$ )	46.1	21.7	39.4	24.3	152.4
FOM	0.83	0.06	0.68	0.13	1

Table 3.1 linear, nonlinear optical properties, and figures of merit (normalized to LiNbO<sub>3</sub>) of several popular crystals

Gallium arsenide (GaAs) is a III/V semiconductor and a compound of the elements gallium and arsenic. It is very attractive for THz generation due to its properties listed as follows: it has large nonlinear coefficient ( $d_{14}=46.1 \text{ pm/V}$  [154]); compared with lithium niobate, GaAs has small THz absorption coefficient ( $0.5\text{-}4.5 \text{ cm}^{-1}$  at 1-3 THz

[155]); Its large thermal conductivity (52 W/m.K [156]) helps to decrease thermo-optic index perturbations under high pump level; the difference between the THz phase index and optical group index is very small, which reduces the mismatch between the propagation velocities of the THz wave and the optical wave inside it.

QPM is a technique for phase matching nonlinear optical interactions in which the relative phase is periodically corrected using structural periodicity (see Fig. 3.1) built into the nonlinear medium. The phase velocity difference is compensated by shifting the phase relative to one another over a coherence distance through inverting the sign of the nonlinear coefficient. Fig. 3. 1 demonstrates the concept of the QPM technique.  $\Lambda$  represents the period of the nonlinear coefficient modulation and is twice of the coherent length. The momentum induced by this modulation is defined as follows:  $K_m=2\pi/\Lambda$ . This momentum will balance the mismatch between the momentum of interaction waves in the parametric process (for example,  $K_p=K_s+K_i+K_m$ , where p, s, i demonstrates the pump, signal, and idler, respectively).

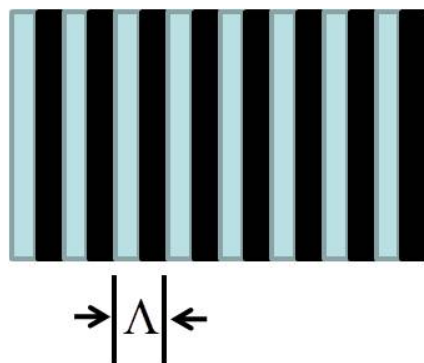


Fig. 3. 1. Concept of quasi-phase-matching technique.

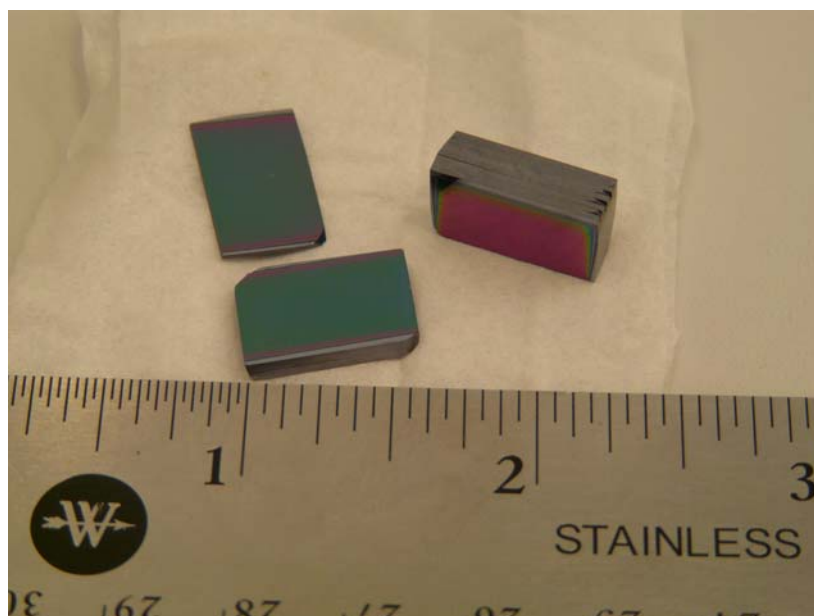


Fig. 3. 2 Pictures of the QPM-GaAs with different periods (1, 2, 5 periods).

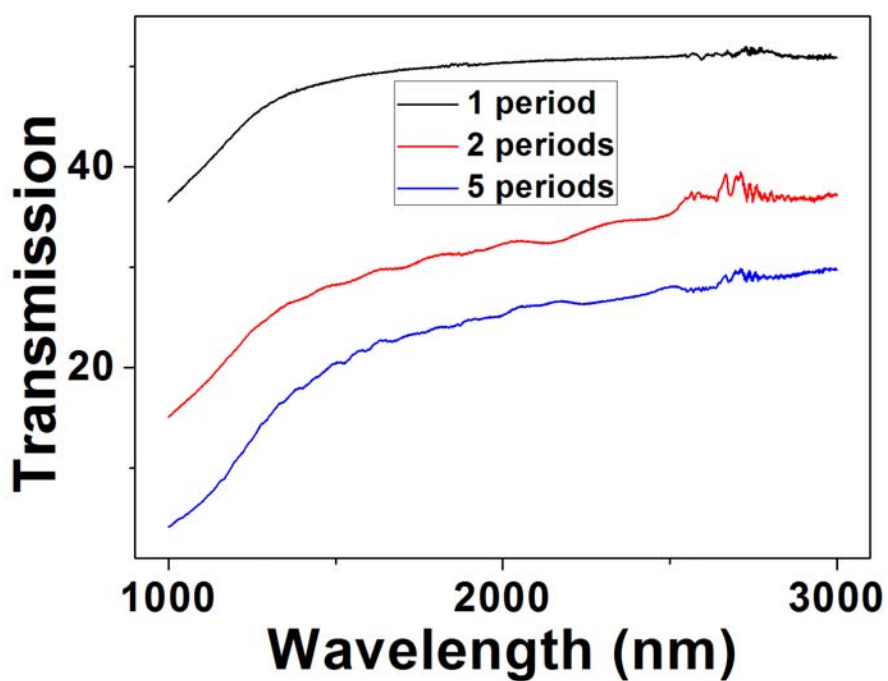


Fig. 3. 3 Transmission spectra of the QPM-GaAs with different periods.

In our experiment, we used diffusion-bonded QPM-GaAs with different number of periods. Fig. 3. 2 shows the picture of the QPM-GaAs used in our experiment. The transmission spectra of the QPM-GaAs with different periods were also measured by using a spectrometer (see Fig. 3. 3). The refractive index of the GaAs at this wavelength region is  $\sim 3.34$  and thus the reflection from the interface between the air and the GaAs can be calculated to be  $\sim 30\%$ . For the GaAs with several periods, the quality of the bonding is not that good that there are several interface between the air and the GaAs. That is the reason for the low transmission as shown in Fig. 3. 3.

### 3.3 Terahertz generation using difference frequency generation (DFG)

Fig. 3. 4 shows the diagram of the two all fiber single frequency nanosecond pulsed laser systems operating at 1918 nm, 1937 nm, respectively. Both of the laser systems are based on MOPA configuration and can produce the transform-limited  $\sim 15$  ns pulses with hundreds of micro-joule energy dependent on the repetition rate.

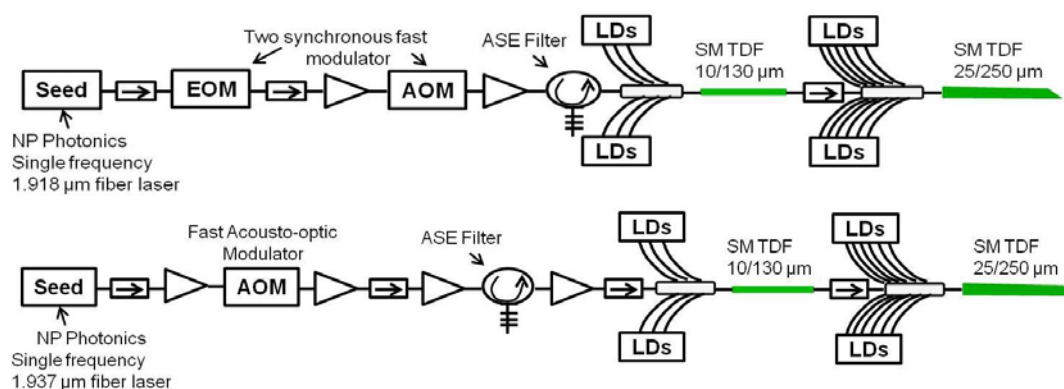


Fig. 3. 4 Diagram of the two all fiber nanosecond pulsed laser system. EOM: electro-optical modulator; AOM: acousto-optical modulator; LDs: Laser diodes; SM TDF: single mode thulium doped fiber.

Fig. 3. 5 demonstrates the diagram of the terahertz wave generation by mixing two high energy nanosecond pulses in the QPM-GaAs. The two laser pulses were collimated and were spatially combined by a polarization beam combiner (PBC) working together with two  $\lambda/2$  wave-plates. The two pulses were made overlapped in time domain by adjusting the time delay between the two laser chains. Then the laser beams were focused onto the QPM-GaAs and the generated terahertz wave were collected and focused into a liquid-helium cooled Bolometer by two parabolic mirrors. The residual 2  $\mu\text{m}$  laser leaked from a hole made in the center of the parabolic mirror and were further blocked by a home-made filter.

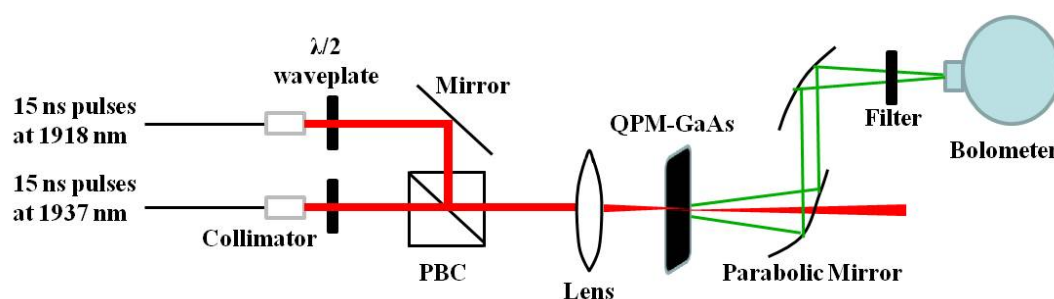


Fig. 3. 5 Terahertz generation using DFG in QPM-GaAs. PBC: polarization beam combiner; QPM-GaAs: quasi-phase-matched gallium arsenide.

The power of the generated THz wave under different pump for QPM-GaAs with different periods are shown in Fig. 3. 6. Compared with 1 period and 5 periods QPM-

GaAs, 2 periods QPM-GaAs achieved higher power THz waves. The maximum average power and peak power of the generated THz waves are  $\sim 5.4 \mu\text{W}$  and 18 mW, respectively. The conversion efficiency is  $\sim 3.89 \times 10^{-6}$ , which can be improved by using QPM-GaAs with low loss.

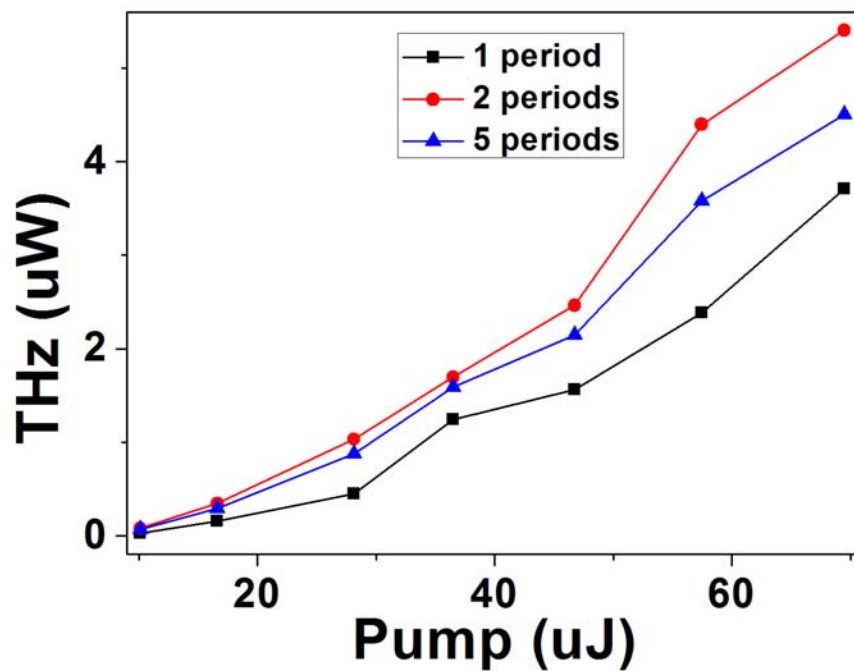


Fig. 3. 6 Power of the THz wave for different QPM-GaAs under different pump level.

### 3.4 Modeling a collinear singly resonated parametric terahertz oscillator

We modeled a collinear singly resonated THz parametric oscillator (TPO).

Through the modeling, we obtain the threshold of the THz OPO and the THz output energy under different pump level.

Fig. 3. 7 shows the configuration of the singly resonated TPO. It is pumped by a nanosecond pulse in 2  $\mu\text{m}$  regime and the signal (also in 2  $\mu\text{m}$  regime) is resonated in the oscillator. The idler is in THz regime and it is extracted out of the oscillator by a off-axis parabolic mirror (M<sub>5</sub>). The nonlinear medium is a QPM-GAs. M<sub>1</sub> and M<sub>4</sub> are two coupler which have high transmission for pump and high reflection for signal (100% in our simulation). M<sub>2</sub> and M<sub>3</sub> have high reflectivity for both pump and signal wave (100% in our simulation).

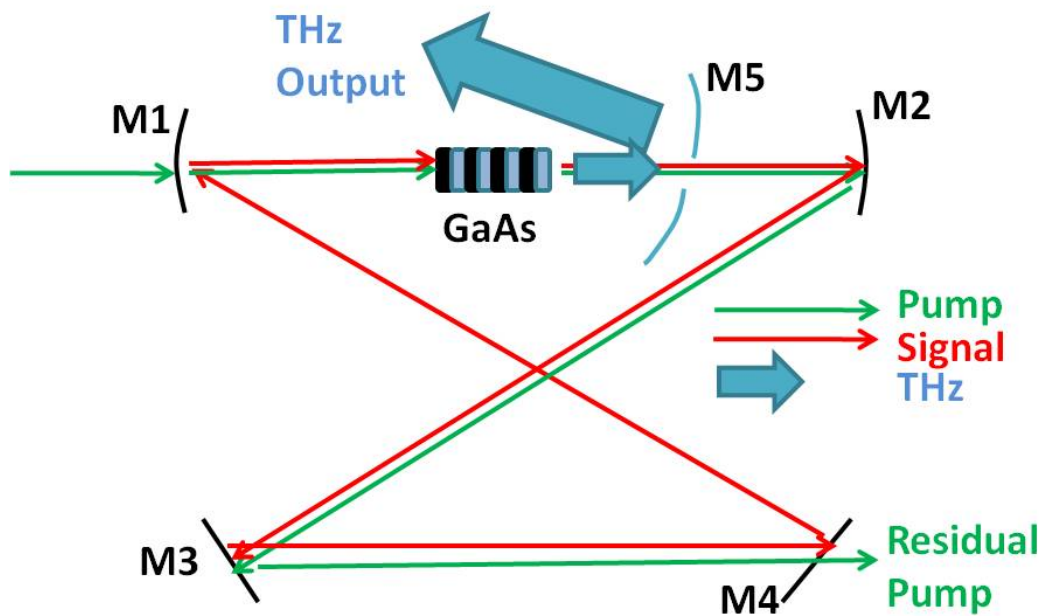


Fig. 3. 7 Configuration of the singly resonated THz parametric oscillator.

We have already built a high power and high energy nanosecond laser source at 1918.4 nm. So pump wavelength is fixed at 1918.4 nm. We would like to achieve THz wave at two wavelengths: Case I: 200  $\mu\text{m}$  and Case II: 118  $\mu\text{m}$ .

The process of the parametric mixing in the QPM-GaAs can be described by the three-wave parametric mixing equations which can be reduced in the plane-wave limit to

$$\left(\frac{\partial}{\partial z} + \frac{1}{v_s} \frac{\partial}{\partial t} + \frac{\alpha_s}{2}\right) \varepsilon_s(t, z) = \frac{i\omega_s d_{eff}}{n_s c} \varepsilon_p(t, z) \varepsilon_i^*(t, z) \exp(i\Delta kz)$$

$$\left(\frac{\partial}{\partial z} + \frac{1}{v_i} \frac{\partial}{\partial t} + \frac{\alpha_i}{2}\right) \varepsilon_i(t, z) = \frac{i\omega_i d_{eff}}{n_i c} \varepsilon_p(t, z) \varepsilon_s^*(t, z) \exp(i\Delta kz)$$

$$\left(\frac{\partial}{\partial z} + \frac{1}{v_p} \frac{\partial}{\partial t} + \frac{\alpha_p}{2}\right) \varepsilon_p(t, z) = \frac{i\omega_p d_{eff}}{n_p c} \varepsilon_s(t, z) \varepsilon_i(t, z) \exp(-i\Delta kz)$$

where  $v_x$  ( $x=i, s, p$ ),  $\alpha_x$  ( $x=i, s, p$ ),  $\omega_x$  ( $x=i, s, p$ ),  $n_x$  ( $x=i, s, p$ ),  $d_{eff}$  and  $\Delta k$  are the group velocity, linear absorption, angular frequency, refractive index, effective nonlinear coefficient and the phase velocity mismatch in the crystal. The important parameters used in the simulation are listed in Table 3.2.

Parameters	Value
Pump wavelength ( $\mu\text{m}$ )	1.9184
Signal wavelength ( $\mu\text{m}$ )	Case I: 1.937; Case II: 1.9501
Idler wavelength ( $\mu\text{m}$ )	Case I: 200; Case II: 118
Linear absorption ( $\text{cm}^{-1}$ )	0.5
Effective nonlinear coefficient (pm/v)	108.55 [157]
Phase velocity mismatch	0
Beam diameter ( $\mu\text{m}$ )	300

Table 3.2. Important parameters used in the simulation for singly resonated THz parametric oscillator.

Based on the parametric mixing equations, the THz OPO is modeled using Split Step Fourier Method in Matlab. Firstly, the threshold of this THz OPO is calculated for different length of crystal as shown in Fig. 3. 8. The threshold is defined by pump peak power. When the crystal is short, the THz OPO needs more pump power to induce enough gain. With the increase of the crystal length, the threshold decreases. However,

longer crystal, on one hand, provides more gain. On the other hand it introduces more linear loss. So when the crystal length is increased to certain value, the threshold starts to increase (see Fig 3. 8). We could find that when the crystal length is  $\sim 30$ mm, the minimum threshold (Case I: 23 kW; Case II: 13.8 kW ) is achieved.

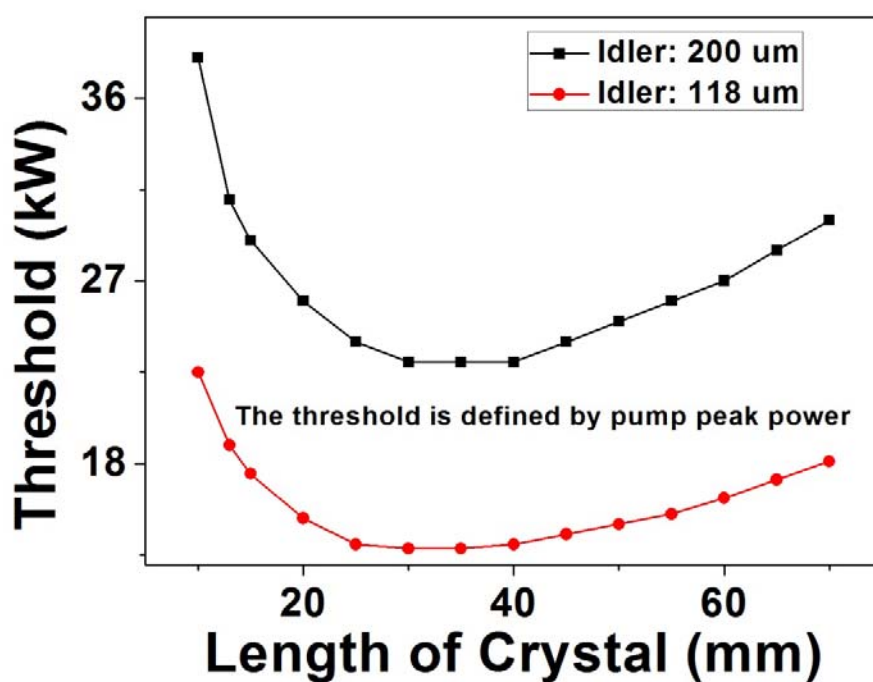


Fig. 3. 8 Threshold of THz OPO for different length of crystal

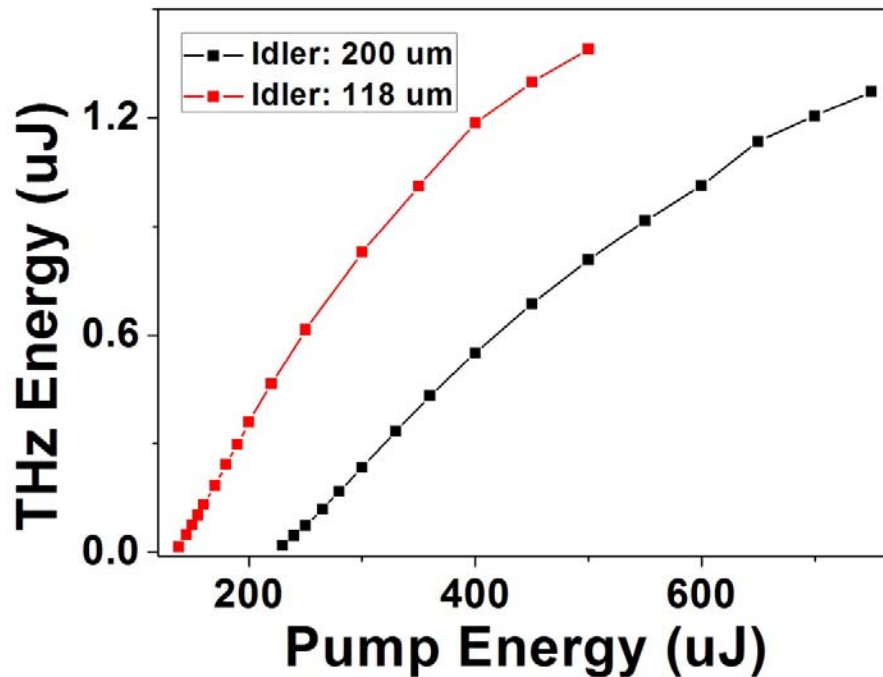
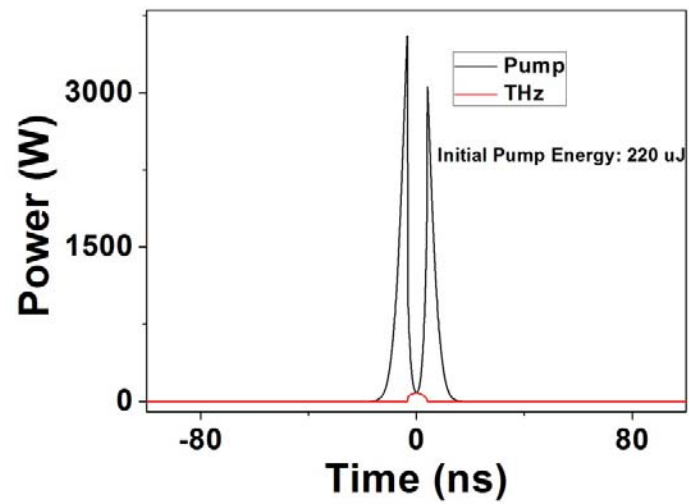
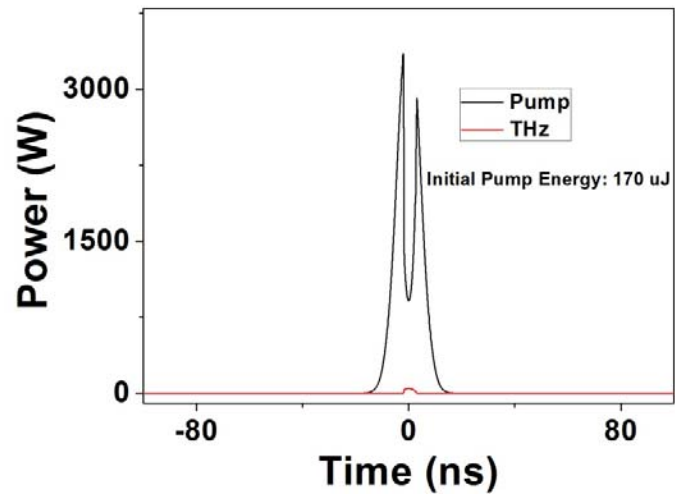


Fig. 3. 9 Generated THz energy under different pump level.

Then the crystal length is fixed as 30 mm and the generated THz energy is calculated under different pump level which is shown in Fig. 3. 9. The efficiency at the maximum output is calculated to be 0.17% and 0.278% for Case I (200 um idler) , II (118 um idler) respectively. Both curves show the saturation trend with the increase of the pump energy. Fig. 3. 10 shows typical pulse shape for residual pump and extracted idler (THz wave). These pulse shape evolution explains the saturation trend shown in Fig. 3. 9 to some extent. From Fig. 3. 10, we could find that the pump is depleted in the region where the idler temporally overlaps with the pump. This depletion (the decrease of the peak power) results in the decrease of the efficiency of the nonlinear energy transfer. And with the increase of the initial pump, this depletion becomes more and more severe. And

the idler energy start to transfer back to pump when the initial pump is increased to certain value.



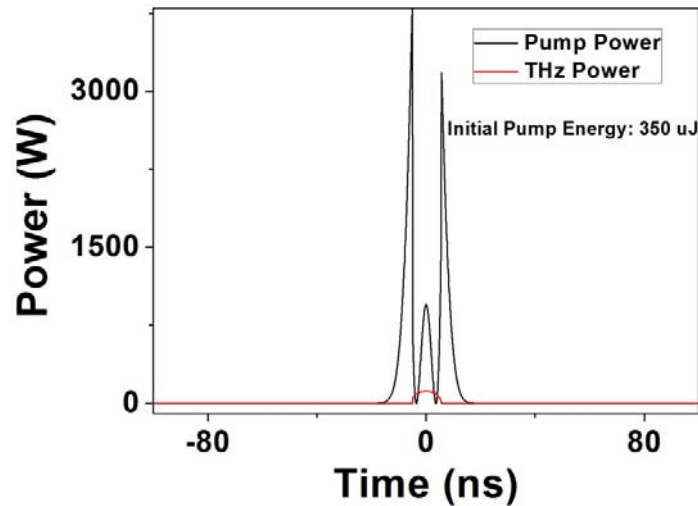


Fig. 3. 10 Pulse shapes of residual pump and extracted Idler wave (THz) for different initial pump.

For undoped GaAs, the threshold of laser induced damage in nanosecond regime is  $\sim 0.9 \text{ J/cm}^2$  [158]. In our simulation, the beam diameter is set as  $\sim 300 \text{ }\mu\text{m}$ . So the damage threshold defined by energy is  $\sim 0.636 \text{ mJ}$ . If 10 ns pulses are chosen, the damage threshold defined by peak power is  $\sim 63.6 \text{ kW}$  which is above the THz threshold. Based on these simulation, it should be expected to build such a collinear THz OPO pumped by nanosecond pulse with high peak power in  $2 \text{ }\mu\text{m}$  regime. The most difficult thing of experimentally implementing such a THz OPO is to get a very good edge coupler ( $M_1$ ), shown in Fig. 7, which should have high transmission for pump but high reflectivity for signal. In order to get THz wave (idler), the wavelength difference between the pump and the signal is only twenty or thirty nanometers. So such a edge coupler is hard to get at  $2 \text{ }\mu\text{m}$  region. The most difficult thing is to get a very good edge coupler ( $M_1$ ), shown in Fig.

7, which should have high transmission for pump but high reflectivity for signal. In order to get THz wave (idler), the wavelength difference between the pump and the signal is only twenty or thirty nanometers. So such a edge coupler is hard to get at 2  $\mu\text{m}$  region.

### 3.5 THz parametric oscillator pumped by cavity enhanced 2 $\mu\text{m}$ nanosecond pulses

#### 3.5.1 Design

We also proposed a THz parametric oscillator pumped by cavity enhanced 2  $\mu\text{m}$  nanosecond pulses, whose configuration is shown in Fig. 3. 11. A high energy nanosecond pulsed fiber laser operating at 2  $\mu\text{m}$  regime is used as the pump and it is enhanced in a four-mirror bow-tie cavity, which serves at the same time as the TPO cavity. A quasi-phase-matching GaAs is anti-reflection coated for the pump wave and then works as the nonlinear medium. Both concave mirrors ( $M_2$ ,  $M_3$ ) and one plane mirror ( $M_4$ ) of the cavity are high reflection coated for the pump and signal wave. The other plane mirror ( $M_1$ ) has a transmission for the pump and signal wave to allow optimal coupling of the pump laser. The pump laser beam out of the fiber need to be adjusted. Specifically, one lens is used to collimating the pulse out of the fiber and then the beam size is adjusted using a telescope. Then two plane mirrors are utilized to couple the pulse into the cavity.

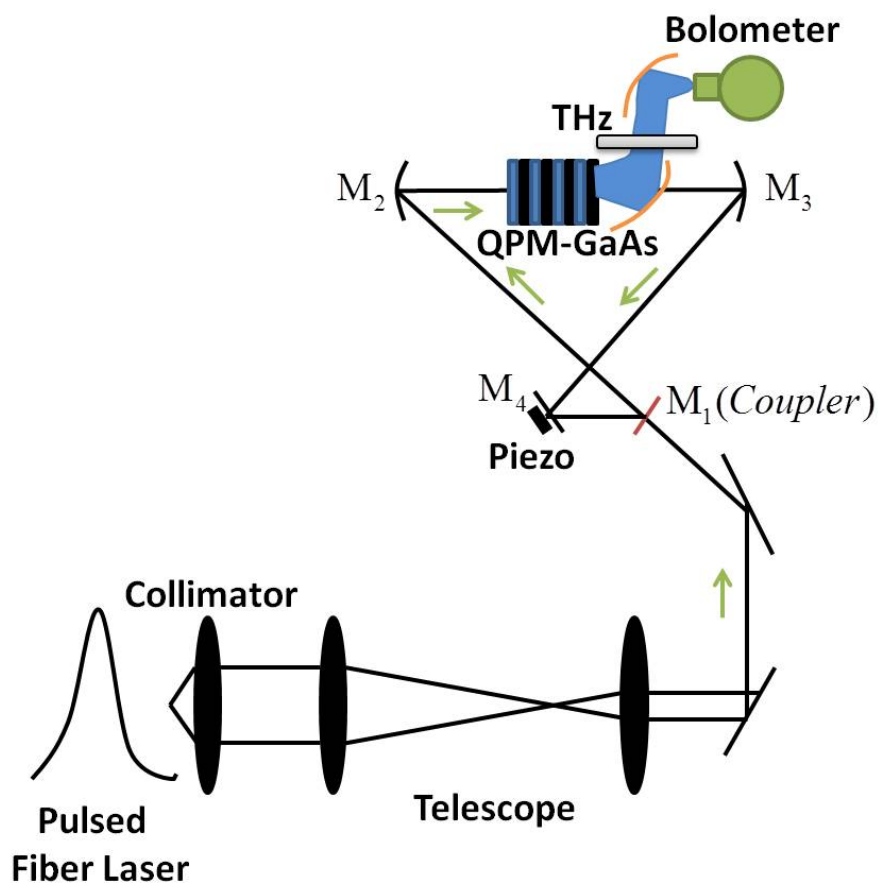


Fig. 3. 11 Configuration of the pump enhanced THz parametric oscillator.

### 3.5.2 Bow-tie cavity stability condition

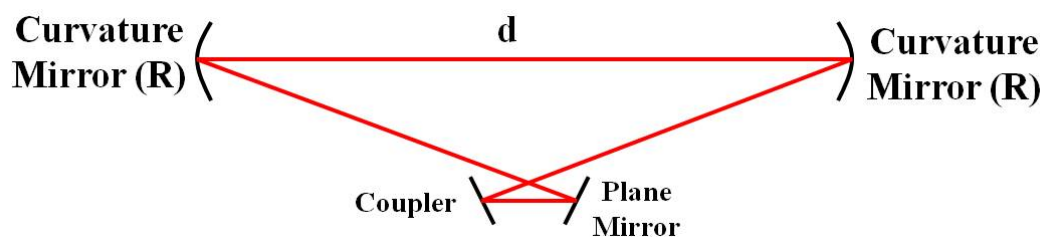


Fig. 3. 12 Diagram of the bow-tie ring cavity.  $R$  is the radius of the curvature mirror;  $d$  is the distance between the two curvature mirrors.

Fig. 3. 12 shows the diagram of the bow-tie ring cavity. It consists a plane mirror, a plane coupler and two curvature mirrors. R is the radius of the curvature mirror. d is the distance between the two curvature mirrors. And L is defined to be the total length of the cavity.

Firstly, we investigate the stability condition of the bow-tie ring cavity using the ABCD matrices method. ABCD matrices are multiplied together starting at the dashed line as shown in Eq. 3. 2:

$$\begin{pmatrix} A & B \\ C & D \end{pmatrix} = \begin{pmatrix} 1 & \frac{L-d}{2} \\ 0 & 1 \end{pmatrix} \begin{pmatrix} 1 & 0 \\ -\frac{2}{R} & 1 \end{pmatrix} \begin{pmatrix} 1 & d \\ 0 & 1 \end{pmatrix} \begin{pmatrix} 1 & 0 \\ -\frac{2}{R} & 1 \end{pmatrix} \begin{pmatrix} 1 & \frac{L-d}{2} \\ 0 & 1 \end{pmatrix} \quad \text{Eq. (3.2)}$$

The stability condition is  $|A+D| < 2$ , which leads to Eq. (3. 3) [159],

$$0 < \frac{L}{R} - \frac{dL}{R^2} + \frac{d^2}{R^2} < 1 \quad \text{Eq. (3.3)}$$

Another extra condition is that the cavity length (L) should be larger than twice of the distance between the two curvature mirrors (2d). The radius of the curvature mirrors (R) is fixed as 0.25 m. So the stability condition for different cavity length as a function of distance between the two curvature mirrors based on Eq. 3. 3 is calculated and shown in Fig. 3. 13. The red curves violate  $L > 2d$  and thus are not physical. So the blue curves, located between 0 and 1 region, represent the stable cavity. Based on this calculation, we choose  $L=75$  cm and  $d=30$  cm and build a stable bow-tie cavity.

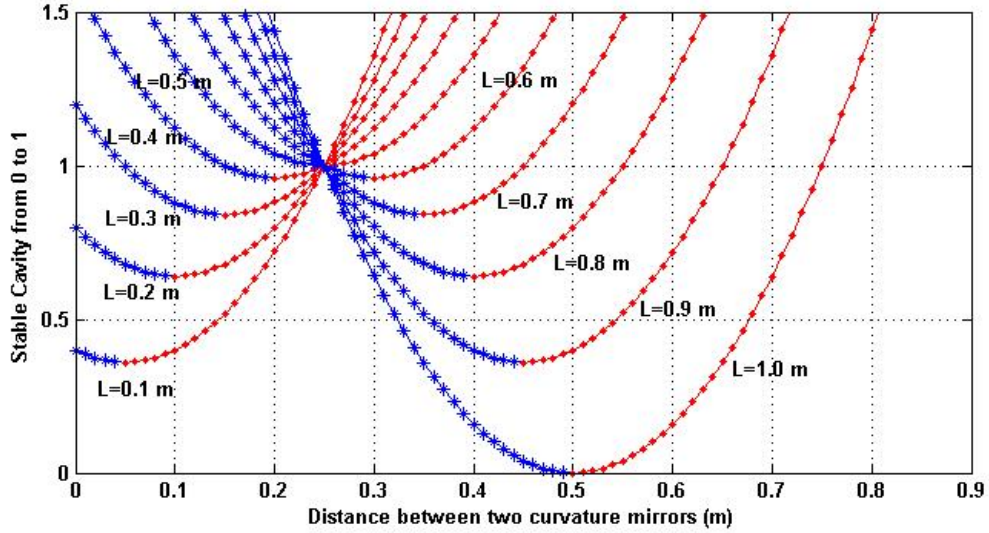


Fig. 3. 13 Stability condition as a function of distance between the two curvature mirrors for different cavity length. The red curves violate  $L > 2d$  and are not physical.

### 3.5.3 Pulse enhancement in the bow-tie cavity

R. Tanaka et. al. investigated the Stable confinement of nanosecond laser pulses in an enhancement cavity [160]. E. Petersen et. al also calculated the pulses enhancement factor in a bow-tie cavity for nanosecond pulses. The equation they utilized is listed as Eq. 3. 4 [161],

$$E_{\text{cavity}} = \sqrt{T} \sum_{n=0}^{\infty} \sqrt{1-l}^n E\left(t' - \frac{Ln}{c}\right) \text{Exp}\left[l\left(w\left(t' - \frac{Ln}{c}\right) - kz\right)\right] \quad \text{Eq. (3. 4)}$$

where  $E$  is the pulse envelope,  $T$  is the transmission at  $M_1$ ,  $l$  is the round trip power loss,  $L$  is the cavity length,  $c$  is the speed of the light,  $k$  is the wave number, Based on this equation, we investigate the enhancement factor of the pulses in the cavity dependent on the pulse duration, the cavity length and the transmission of the coupler.

Fig. 3. 14 demonstrates the pulse enhancement as a function of the pulse duration for different cavity length. The transmission of the coupler is fixed as 3% to impedance matching the cavity loss (3%). We could find that the enhancement factor increases as the increase of the pulse duration and then tend to be a constant. For the same pulse duration, the enhancement factor decreases as the increaser of the length of the cavity.

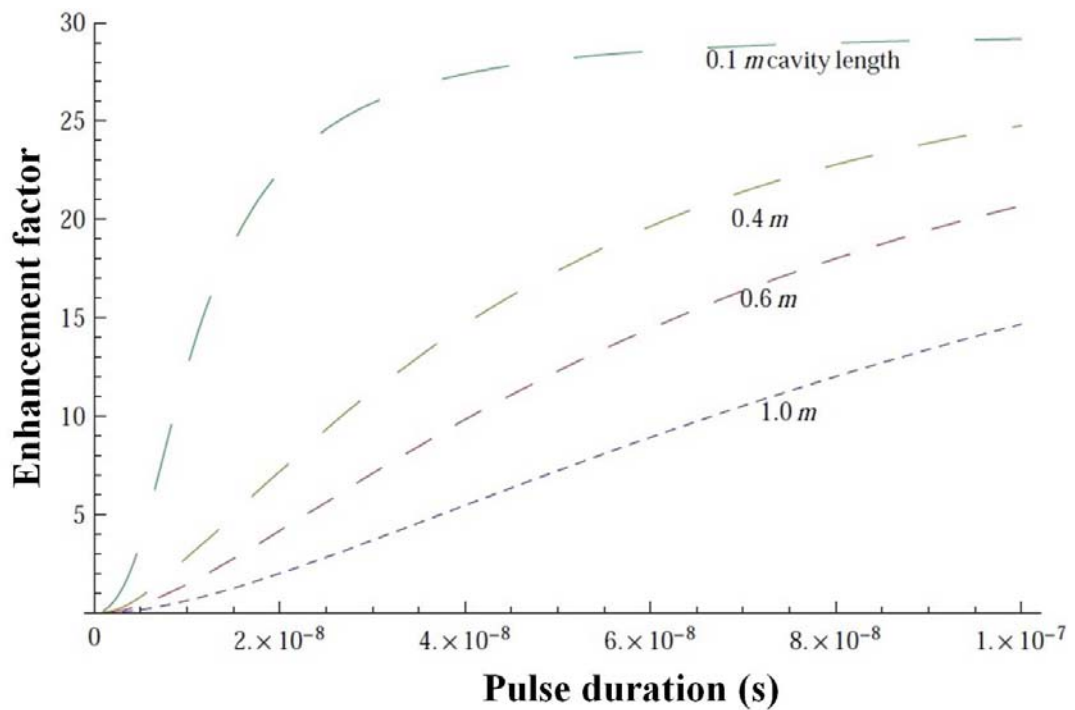


Fig. 3. 14 Enhancement factor as a function of the pulse duration for different cavity length.

For short pulses, it is better to use over-impedance-matching, which means that transmission of the coupler is higher than the cavity loss. It is verified by the simulation results shown in Fig.3. 15.

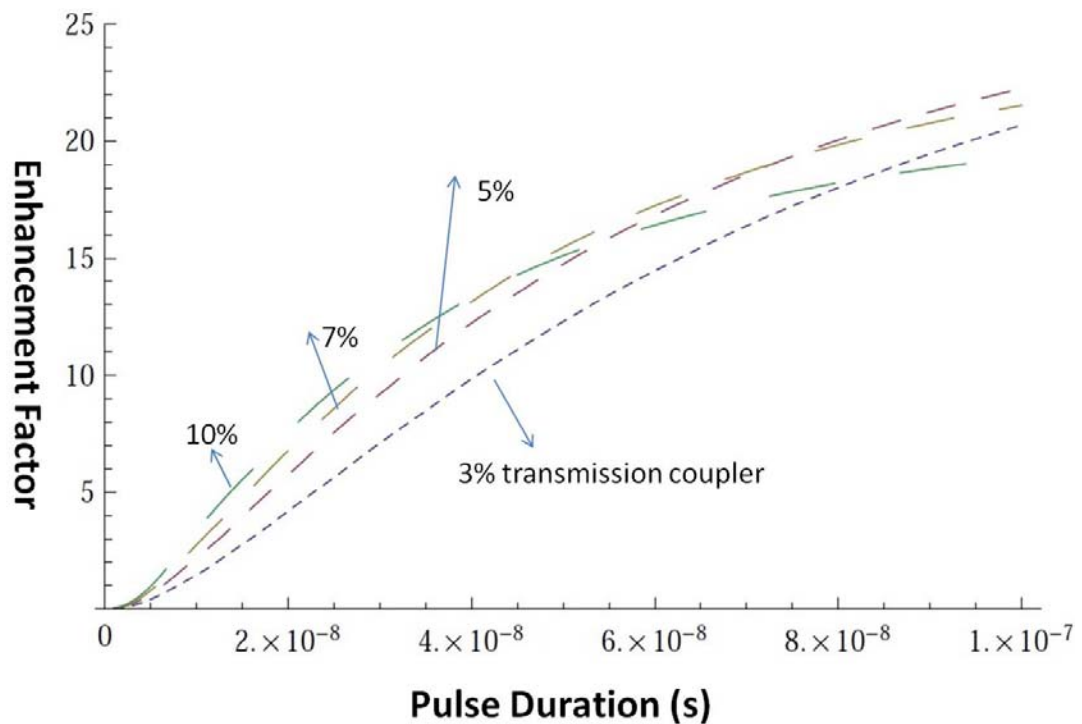


Fig. 3. 15 Enhancement factor as a function of the pulse duration for different transmission of the coupler.

#### 3.5.4 Implementation of the pulse enhancement in the bow-tie cavity

Based on the design mentioned above, we build a bow-tie cavity as shown in Fig. 3. 16.  $M_1$  is the coupler.  $M_2$  is a plane mirror with high reflectivity (99%) and is fixed on a piezo.  $M_3$  and  $M_4$  are two curvature mirrors with radius of 25 cm. The piezo is utilized to move the  $M_2$  to change the cavity length periodically.

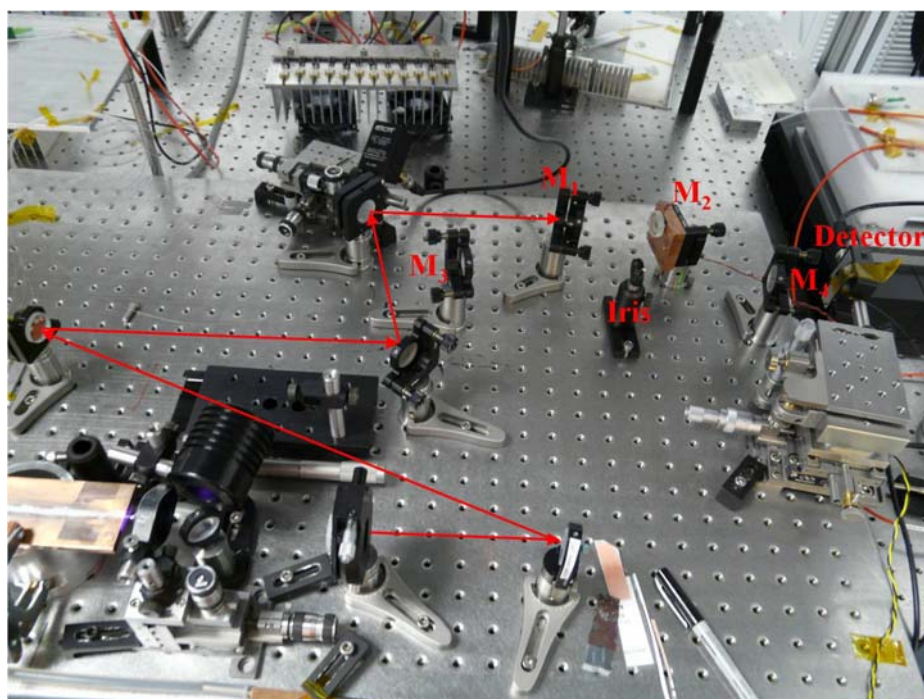
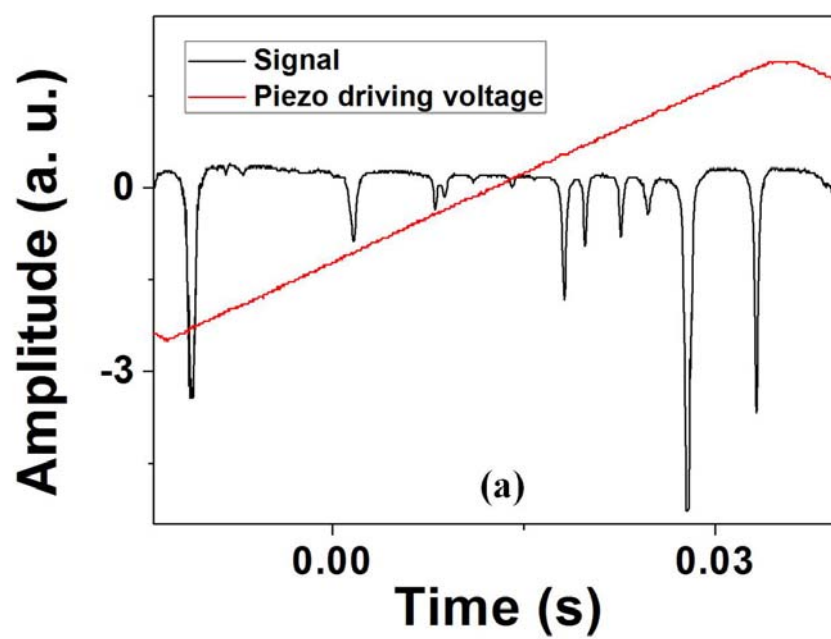


Fig. 3. 16 Bow-tie ring cavity in the lab.



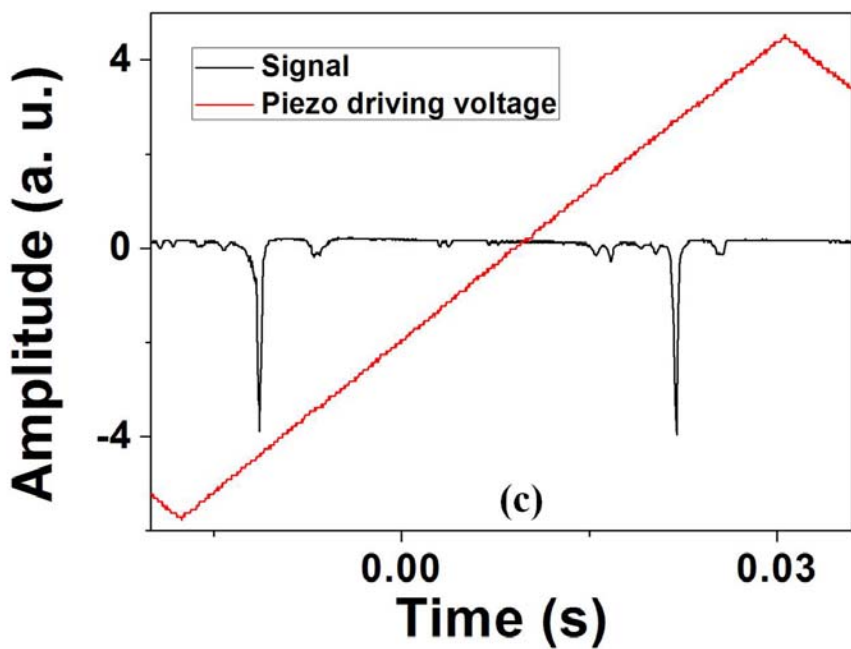
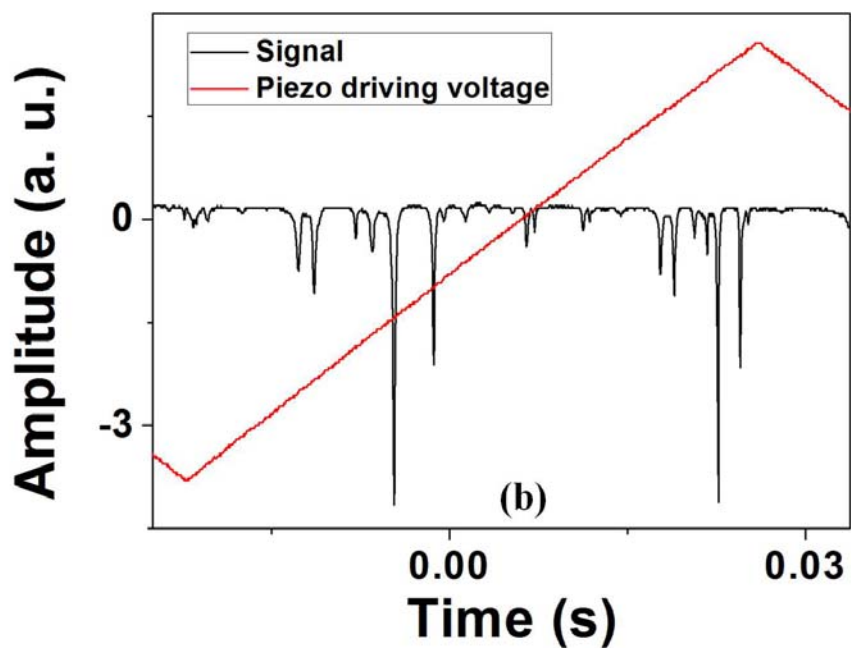


Fig. 3. 17 Laser resonances in the bow-tie cavity when its length is adjusted by a piezo.

Fig. 3. 17 shows the resonances of the laser in the cavity when the piezo is used to change the cavity length periodically. The alignment was optimized by monitoring the resonance spectra (for example, from Fig. 3. 17 (a) to Fig. 3. 17 (c)). But the enhancement factor was measured only 3 to 5 for continuous laser. The other problem is that the jitter is so big that the cavity cannot be locked. The big jitter may come from laser system itself and the environment vibrations.

## CHAPTER 4

### ALL FIBER WAVELENGTH TUNABLE MODE-LOCKED LASER OPERATING IN 2 $\mu\text{m}$ REGIME

#### 4.1 Introduction

Ultrafast fiber sources have seen rapid developments over the past decade due to their numerous potential applications in bio-imaging, spectroscopy and telecommunications. Compared with conventional ‘bulk’ solid-state lasers, ultrafast fiber sources have significant advantages including compactness, low cost, and simple thermal management. In addition, the performance (in term of output power, wavelength coverage and pulse duration) of ultrafast fiber lasers has been improving, which allows them to compete directly with traditional solid state laser sources.

Fiber lasers based on Er-doped and Yb-doped materials typically operate near 1550nm and 1030nm, respectively. Fiber sources based on Thulium (Tm) and Holmium (Ho) doped glasses that operate in the 2  $\mu\text{m}$  region have shown average powers up to 100 W with 68% efficiency [24, 140, 162, 163]. The broad and smooth gain spectrum of thulium-doped silica fiber makes it a well-suited gain medium for generation of ultrashort optical pulses and broad wavelength tunability. To date, a few examples of ultrafast Tm-doped fiber oscillators have been reported [164-170]. The performance of these oscillators is quite modest compared to mode-locked lasers based on Er-doped and Yb-doped materials. Regarding wavelength tunability of fiber lasers near 2 micron wavelength, there are only two published works so far [164, 166]. The previous lasers were built with bulk optical components which required alignment and adjustment. In

this work, we report the construction and characteristics of a Tm-doped all-fiber tunable mode-locked oscillator. Tuning range of  $> 50\text{nm}$  is achieved using FTCNT SA and a fiber format tunable filter.

#### 4.2 Configuration of the mode-locked laser

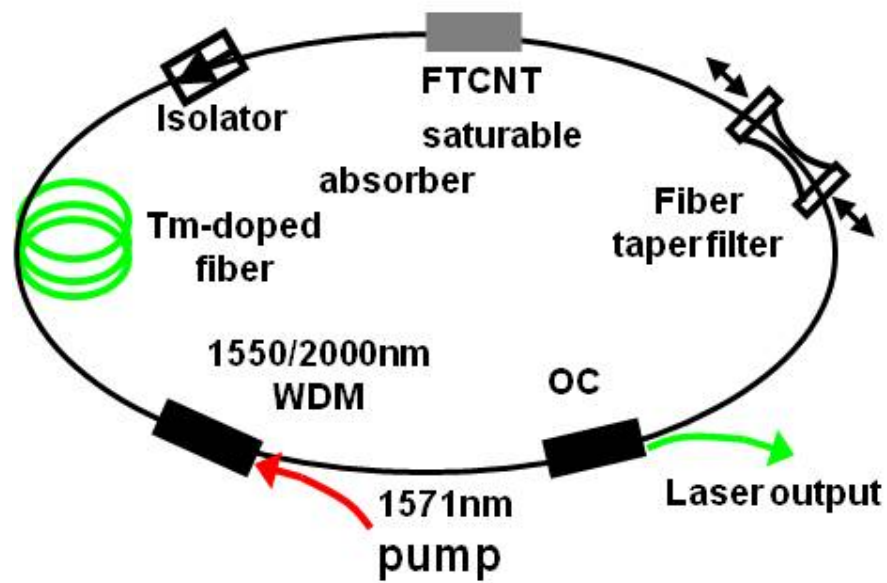


Fig. 4. 1 Schematic diagram of the all-fiber mode-locked tunable ring laser.

The schematic diagram of our laser is shown in Fig. 4. 1. The ring laser contains  $\sim 2.2\text{-m}$  of Tm-Ho co-doped fiber with  $9\text{-}\mu\text{m}$  core diameter. The absorption at  $1571\text{ nm}$  is  $\sim 23.1\text{ dB/m}$ . The pump laser is a diode laser operating near  $1571\text{ nm}$ , which is amplified to  $\sim 500\text{ mW}$  average power using a home-built cladding pumped Er/Yb codoped fiber amplifier. The  $1571\text{ nm}$  pump laser is launched into the ring cavity through a  $1550/2000\text{ nm}$  WDM fiber coupler to pump the Tm-Ho co-doped fiber in the core. We use a FTCNT SA similar to the one we reported in Ref. 169 as the mode-locking element. Compared to

traditional mode-locking techniques, SA based on CNT avoids the complexity and environmental instability of NPE while providing much more operating spectral coverage compared to SESAM [171]. The linear loss of the SA was measured to be  $\sim 30\%$ . A fused fiber output coupler is used to extract  $\sim 60\%$  of the circulating light out of the resonator. For stable unidirectional operation a fiber-coupled isolator is incorporated into the cavity. The loss of the isolator was measured at  $\sim 5$  dB, which is quite high and needs improvement. Nevertheless, stable mode-locking is observed at a wide range of laser parameters (cavity lengths, pump powers and central wavelengths).

#### 4.3 Wavelength tuning element

Wavelength tunability is achieved by incorporating a fiber taper filter into the cavity. This in-house made fiber taper has a spectral response that is different from the one used in the SA. The taper in the SA was pulled adiabatically to ensure a flat spectral response [172]. The taper used for tuning, on the other hand, was pulled un-adiabatically to introduce mode coupling. The spectral response of the taper is close to a sinusoidal function as the result of modal interference. We have demonstrated previously the tuning of CW fiber laser using this type of device [173]. The fiber taper is fixed using a pair of fiber holders that could be moved separately to stretch or unstretch the taper and thus to tune the central wavelength of the mode-locked laser. The use of the FTCNT SA and the fiber taper tunable filter has enabled the construction of an all-fiber format wavelength tunable laser oscillator where no alignment is needed.

The spectral response of the fiber taper-based tunable filter was measured using an ASE source based on the Tm-Ho co-doped gain fiber. The taper has an excess loss of

$\sim 0.5$  dB, a modulation depth of  $\sim 7.5$  dB and a free spectral range (FSR, the peak-to-peak distance in the spectral response) of  $\sim 60$  nm. Furthermore, the full width at half maximum (FWHM) of the transmission curve of the filter is  $\sim 30$  nm. It acts as a good bandpass filter for the laser and it does not limit the bandwidth of the mode-locked pulses. The taper is fixed at two optical stages as shown in Fig. 4. 2. The spectral response is blue-shifted when the taper is mechanically stretched after being pulled using a flame (see Fig. 4. 3). We could tune the filter response by one FSR by stretching the taper about 200 micron. The effect is elastic in nature so that the location of the peaks or dips could be recovered by unstretching the taper by the same amount. The process is repeatable and controllable making the taper advantageous for tuning the wavelength of the mode locked laser.

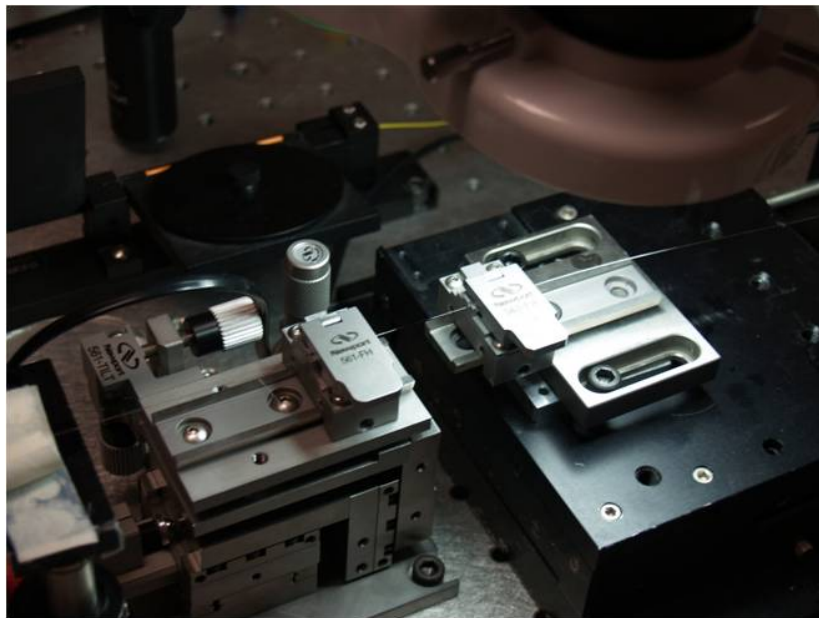


Fig. 4. 2 The fiber taper was fixed at two stages used for wavelength tuning element.

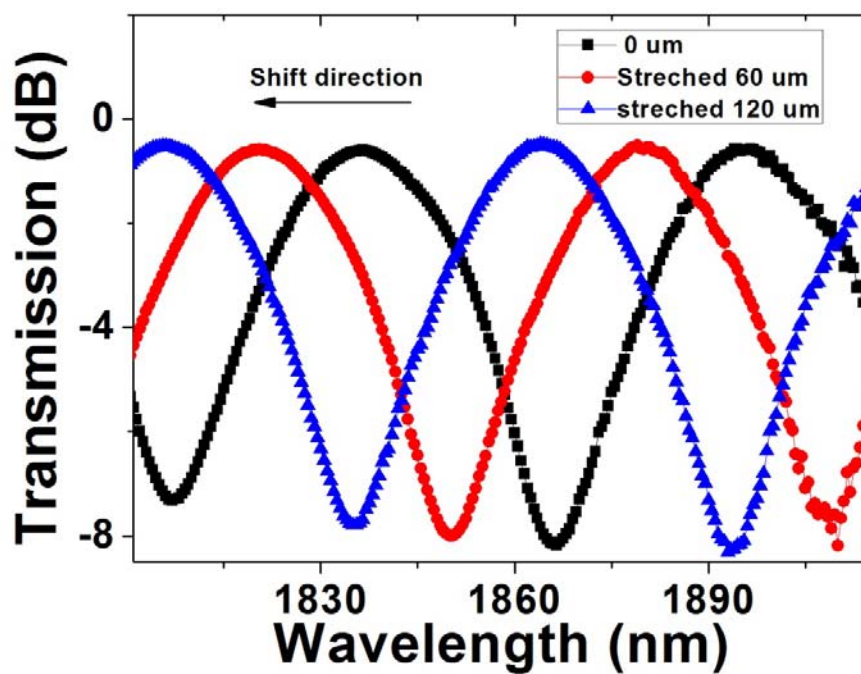
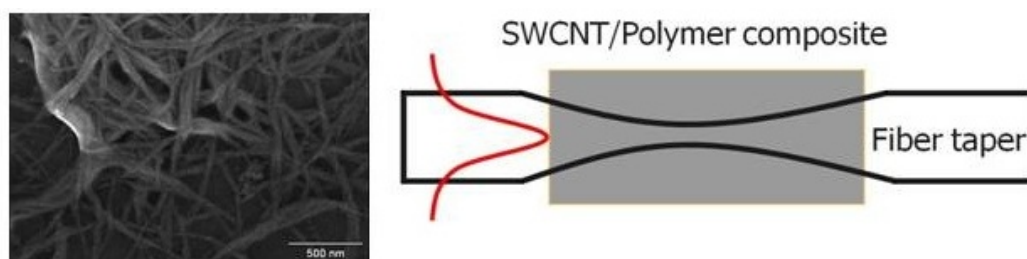


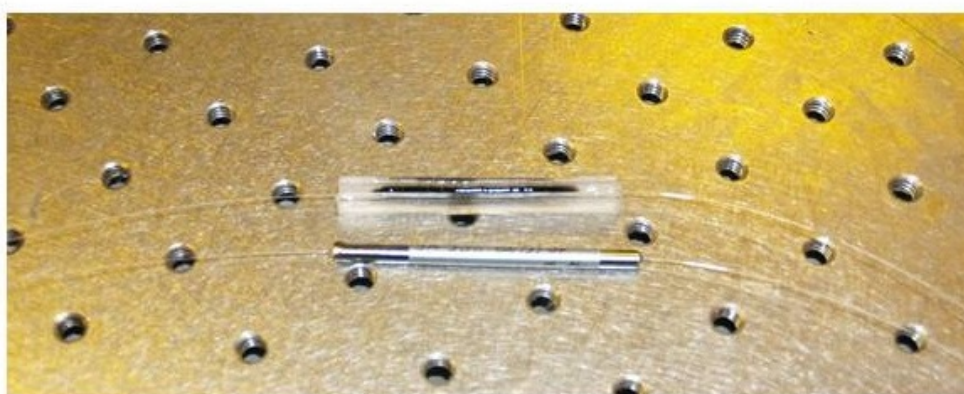
Fig. 4. 3 Spectral response of the fiber taper filter and its shift upon stretching.

#### 4.4 Mode-locking element

An adiabatic fiber taper embedded in single-wall carbon nanotube (SWCNT) polymer composite works as the saturable absorber in the laser cavity to enable mode locking [172]. Fig. 4. 4 demonstrates the picture of the absorber fabricated in Kphotonics Inc.



SEM picture of SWCNTs      The interaction is through the evanescent field



## Packaged Absorber

Fig. 4. 4 The CNT based absorber (from [www.kphotonics.com](http://www.kphotonics.com)).

### 4.5 Results

At the initial position of the taper tunable filter, the laser was mode-locked at 1891.1 nm when the pump power was  $\sim 365$  mW. Mode-locking was self-starting without any adjustment of the laser cavity. The tuning range is  $\sim 50$  nm, covering the wavelength range from 1866.3 nm to 1916.4 nm through shifting the tunable filter by one FSR (Fig. 4. 5). The laser remained mode-locked within the entire tuning process. At some positions

of the tunable filter we observed small CW break-through on the output spectrum. When this happened, the pump laser was adjusted slightly to remove the CW break-through.

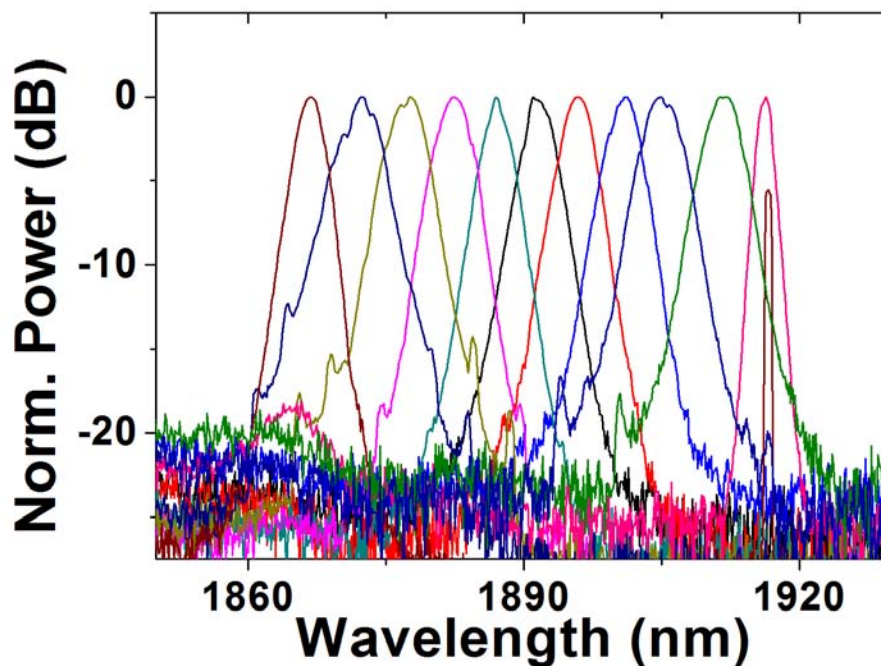


Fig. 4. 5 Tuning characteristic of the mode-locked ring laser using an intracavity fiber taper tunable filter.

The duration of the output pulses was measured using an home-built interferometric autocorrelator. The result of this measurement is shown in Fig. 4. 6. We demonstrated pulse duration of  $\sim 1$  ps over most of the tuning range. The average output power was also measured for each wavelength and the result is shown in Fig. 4. 6. The repetition rate of the pulse train was measured to be  $\sim 40$  MHz.

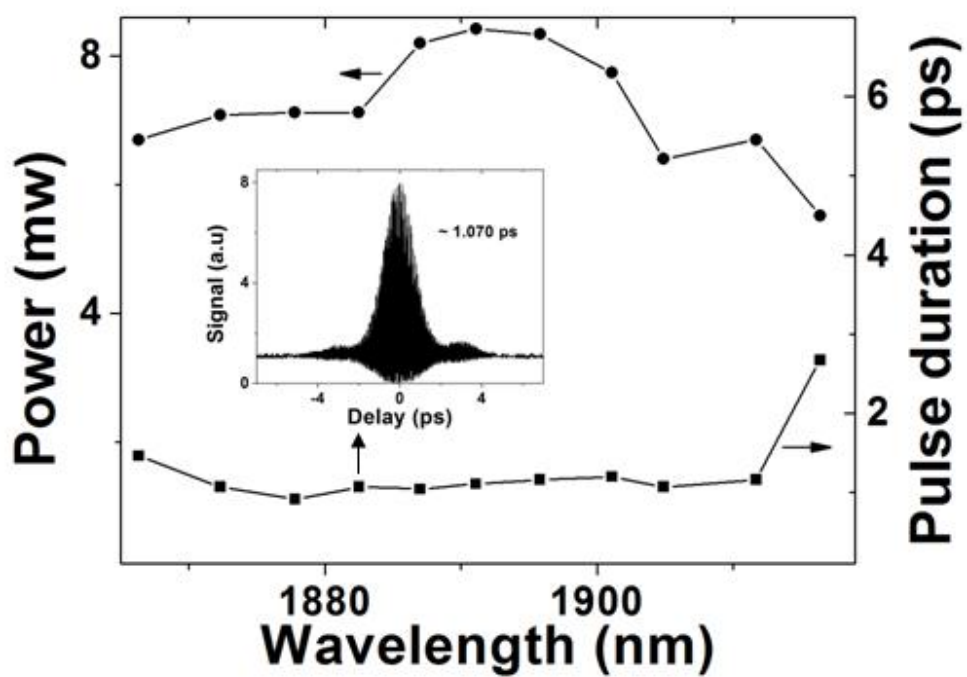


Fig. 4. 6 Output power and pulse duration versus wavelength; the inset is the interferometric autocorrelation trace when the laser wavelength is at 1882.5 nm.

#### 4.6 Summary

we demonstrated an all-fiber wavelength tunable CNT mode-locked Tm/Ho-codoped laser using a single-mode fiber taper as the spectral filter with tuning range of over 50 nm (1866.3 to 1916.4 nm).

## CHAPTER 5

### SUMMARY AND PROSPECT

#### 5.1 Summary

This dissertation research work has mainly investigated 2  $\mu\text{m}$  all-fiber based pulsed laser sources in both nanoseconds and ultrafast regime. THz wave generation, using high energy 2  $\mu\text{m}$  nanosecond pulses, has also been theoretically and experimentally investigated.

In nanosecond regimes, we built a high power and high energy monolithic single frequency pulsed laser system in MOPA configuration, producing >16 W average power, > 73 kW peak power single frequency  $\sim 2$  ns transform-limited pulses and mJ-level single frequency  $\sim 15$  ns transform-limited pulses. To our best knowledge, this is the highest average power, peak power and pulse energy for such kind of all fiber single frequency nanosecond pulsed laser source in the 2  $\mu\text{m}$  regime.

One model has been built to simulate the pulsed double-cladding highly thulium-doped germanate fiber amplifier. The model can be utilized to calculate the pulse energy, average power, stored energy in the active fiber, the ASE dependence on the pump power, repetition rate and seed energy, etc. A good agreement is achieved between the calculated and measured data. The model can provide us guidance to design and optimize the pulsed highly thulium doped double-cladding germanate fiber amplifier.

Two channel of high energy nanosecond pulses are utilized to generate THz wave in a quasi-phase-matched (QPM) gallium arsenide (GaAs) based on difference frequency generation.  $\sim 5.4$   $\mu\text{W}$  average power and  $\sim 18$  mW peak power THz wave is achieved.

One model is built to simulate a singly resonated THz parametric oscillator. The threshold, the dependent of output THz energy on pump energy was investigated through this model. One pump enhanced THz parametric oscillator has also been proposed. And the enhancement factor for nanosecond pulses in the cavity is calculated for different pulse duration, cavity length and coupler transmission. One bow-tie ring cavity was built in the lab and the laser resonances were observed by using a piezo to adjust the cavity length periodically.

In ultrafast regime, We build an all-fiber thulium-doped wavelength tunable mode-locked laser operating near 2  $\mu\text{m}$ . Reliable self-starting mode locking over a large tuning range ( $> 50$  nm) using fiber taper based carbon nanotube (FTCNT) saturable absorber (SA) is observed. Spectral tuning is achieved by stretching another home-built fiber taper. The pulse duration in the whole tuning range is around one picosecond. To the best of our knowledge, this is the first demonstration of an all-fiber wavelength tunable mode-locked laser near 2  $\mu\text{m}$ .

## 5.2 Prospect

The average power and pulse energy of the nanosecond pulses can be further scaled using another power amplifier stage using newly developed 40  $\mu\text{m}$  thulium-doped germanate fiber in NP Photonics, Inc..

The singly resonated parametric oscillator can be experimentally implemented after getting a good coupler (high transmission at 1918.4 nm and high reflectivity at 1937 nm, for example).

## REFERENCES

1. J. Hecht, "Short history of the laser development", *Opt. Engineering* **49**, 091002 (2010).
2. Theodore H. Maiman, "Stimulated optical radiation in ruby", *Nature* **187**, 493-494 (1960).
3. A. Javan, Journal of Colloid and W. R. Bennett, and D. R. Herriott, "Population inversion and continuous optical maser oscillation in a gas discharge containing a He-Ne mixture" *Phys. Rev. Lett.* **63**, 106-110 (1961).
4. L. F. Johnson, "Optical maser characteristics of  $\text{Nd}^{3+}$  in  $\text{CaF}_2$ ", *J. Appl. Phys.* **33**, 756 (1962).
5. R. N. Hall, G. E. Fenner, J. D. Kingsley, T. J. Soltys, and R. O. Carlson, "Coherent light emission from GaAs junctions", *Phys. Rev. Lett.* **9**, 366 (1962).
6. J. E. Geusic, H. M. Marcos, and L. G. Van Uitert, "Laser oscillations in Nd-doped yttrium aluminum, yttrium gallium and gadolinium garnets", *Appl. Phys. Lett.* **4**, 182 (1964).
7. C. K. N. Patel, "Continuous-wave laser action on vibrational-rotational transitions of  $\text{CO}_2$ ", *Physical Review* **136**, 1187-1193 (1964).
8. W. B. Bridges, "Laser oscillation in singly ionized argon in the visible spectrum", *Appl. Phys. Lett.* **4**, 128-130 (1964).
9. P. P. Sorokin and J. R. Lankard, "Stimulated emission observed from an organic dye, chloro-aluminum phthalocyanine", *IBM J. Res. Develop.* **10**, 162-163 (1966).

10. R. Dingle and C. H. Henry, "Quantum effects in heterostructure lasers", US Patent # 3982207 (1975).
11. P. F. Moulton, "Spectroscopic and laser characteristics of Ti:Al<sub>2</sub>O<sub>3</sub>", J. Opt. Soc. B **3**, 125-133 (1986).
12. C. J. Koester and E. Snitzer, "Amplification in a Fiber Laser", Applied Optics **3**, 1182-1186 (1964).
13. D. S. Funk, J. W. Carlson, and J. G. Eden, "Ultraviolet (381 nm), room temperature laser in neodymium-doped fluorozirconate fibre", Electron. Lett. **30**, pp. 1859-1860 (1994).
14. D. S. Funk, J. W. Carlson, and J. G. Eden, "Room-temperature fluorozirconate glass fiber laser in the violet (412 nm)", Opt. Lett. **20**, pp. 1474-1476 (1995).
15. J. Y. Allain, M. Monerie, and H. Poignant, "Blue upconversion fluorozirconate fiber laser", Electron. Lett. **26**, pp. 166-168 (1990).
16. J. Y. Allain, M. Monerie, and H. Poignant, "Room temperature CW tunable green upconversion holmium fibre laser", Electron. Lett. **26**, pp. 261-263 (1990).
17. J. Y. Allain, M. Monerie, and H. Poignant, "Tunable CW lasing around 610, 635, 695, 715, 885 and 910 nm in praseodymium-doped fluorozirconate fibre", Electron. Lett. **27**, pp. 189-191 (1991).
18. T. J. Whitley, C. A. Millar, R. Wyatt, M. C. Brierley, and D. Szebesta, "Upconversion pumped green lasing in erbium-doped fluorozirconate fibre", Electron. Lett. **27**, pp. 1785-1786 (1991).
19. J. Y. Allain, M. Monerie, and H. Poignant, "Tunable green upconversion erbium fibre laser", Electron. Lett. **28**, pp. 111-113 (1992).

20. H. Po, J. D. Cao, B. M. Laliberte, R. A. Minns, R. F. Robinson, B. H. Rockney, R. R. Tricca and Y. H. Zhang, "High power neodymium-doped single transverse mode fibre laser", *Electron. Lett.* **29**, pp. 1500-1501 (1993).
21. H. M. Pask, R. J. Carman, D. C. Hanna, A. C. Tropper, C. J. Mackechnie, P. R. Barber, J. M. Dawes, "Ytterbium-doped silica fiber lasers: versatile sources for the 1-1.2  $\mu\text{m}$  region", *IEEE J. Sel. Top. Quantum Electron.* **1**, pp.2-13 (1995).
22. R. J. Mears, L. Reekie, M. Jauncey, and D. N. Payne, "Low-noise erbium-doped fiber amplifier operating at 1.54  $\mu\text{m}$ ", *Electron. Lett.* **26**, pp. 1026 (1987).
23. E. Desurvire, J. R. Simpson, and P. C. Becker, "High-gain erbium doped traveling wave fiber amplifier", *Opt. Lett.* **12**, pp. 888-890 (1987).
24. J. Wu, S. Jiang, T. Luo, and J. Geng, N. Peyghambarian, and N. P. Barnes, "Efficient thulium-doped 2  $\mu\text{m}$  germanate fiber laser", *IEEE Photon. Technol. Lett.* **18**, pp. 234-236 (2006).
25. S. D. Jackson, "Passively Q-switched Tm-doped silica fiber lasers", *Appl. Opt.* **46**, pp. 3311-3317 (2007).
26. X. Zhu and R. Jain, "Compact 2 W wavelength-tunable Er:ZBLAN mid-infrared fiber laser", *Opt. Lett.* **32**, pp. 2381-2383 (2007).
27. X. Zhu and R. Jain, "10-W-level diode-pumped compact 2.78 ZBLAN fiber laser", *Opt. Lett.* **32**, pp. 26-28 (2007).
28. S. Foster, A. Tikhomirov, M. Milnes, J. van Velzen, and G. Hardy, "A fiber laser hydrophone", in *Proc. 17th Int. Conf. Optical Fiber Sensors*, Bruges, Belgium, 627-610 (2005).

29. P. Nash, "Review of interferometric optical fibre hydrophone technology", IEEE Proc., Radar Sonar Navig. **143** (3), pp. 204-209 (1996).
30. S. W. Henderson, P. J. M. Suni, C. P. Hale, S. M. Hannon, J. R. Magee, D. L. Bruns, and E. H. Yuen, "Coherent laser radar at 2 m using solid-state lasers," IEEE Trans. Geoscience and Remote Sensing **31**, pp.4-15 (1993).
31. R. Claps, J. Sabbaghzadeh, and M. Fink, "Raman spectroscopy with a single frequency, high power, broad-area laser diode", Appl. Spectroscopy **53**, pp. 491-496 (1999).
32. W. Shi, M. A. Leigh, J. Zong, Z. Yao, D. T. Nguyen, A. Chavez-Pirson, and N. Peyghambarian, "High power all fiber based narrow-linewidth single mode fiber laser pulses in the C-Band and frequency conversion to THz generation", IEEE. J. Sel. Top. Quantum Electron. **15**, pp. 377-384 (2009).
33. S. A. Babin, D. V. Churkin, A. E. Ismagulov, S. I. Kablukov, and M. A. Nikulin, "Single frequency single polarization DFB fiber laser", Laser Phys. Lett. **4**, pp. 428 (2007).
34. A. Schulzgen, L. Li, D. Nguyen, Ch. Spiegelberg, R. Matei Rogoian, A. Laronche, J. Albett, and N. Peyghambarian, "Distributed feedback fiber laser pumped by multimode laser diodes", Opt. Lett. **33**, pp. 614-616 (2008).
35. S. Agger, and J. H. Povlsen, "Single-frequency thulium-doped distributed-feedback fiber laser", Opt. Lett. **29**, pp. 1503-1505 (2004).
36. C. Poulsen, P. Varming, J. Pedersen, M. Beukema, and S. Lauridsen, in Conference on Lasers and Electro-Optics (CLEO), Vol. 88 of OSA Trends in Optics and Photonics Series (Optical Society of America, Washington, D. C. , 2003).
37. <http://npphotonics.com/includes/main.php?pid=49>
38. J. Geng, J. Wu, Sh. Jiang, and J. Yu, "Efficient operation of diode-pumped single-frequency thulium-doped fiber lasers near 2  $\mu\text{m}$ ," Opt. Lett. **32**, 355-357 (2007).

39. J. Geng, Q. Wang, T. Luo, Sh. Jiang, and E. Amzaierdian, "Single-frequency narrow-linewidth Tm-doped fiber laser using silicate glass fiber," *Opt. Lett.* **34**, 3493-3495 (2009).
40. K. Kieu and M. Mansuripur, "Fiber laser using a microsphere resonator as a feedback element", *Opt. Lett.* **32**, pp. 244-246 (2007).
41. M. Leigh, W. Shi, J. Zong, J. Wang, Sh. Jiang and N. Peyghambarian, "Compact, single-frequency all-fiber Q-switched laser at 1  $\mu\text{m}$ ," *Opt. Lett.* **32**, 897-899 (2007).
42. Y. Kaneda, Y. Hu, C. Spiegelberg, J. Geng, and Sh. Jiang, "Single-frequency, all-fiber Q-switched laser at 1550 nm," OSA Topical Meeting on Advanced Solid-State Photonics 2004, Postdeadline paper PD5.
43. K. T. Vu, A. Malinowshi, D. J. Richardson, F. Ghiringhelli, L. M. B. Hickey, M. N. Zervas, "Adaptive pulse shape control in a diode-seeded nanosecond fiber MOPA system," *Opt. Express* **14**, 10996-11001 (2006).
44. E. Petersen, W. Shi, A. Chavez-Pirson, and N. Peyghambarian, "High peak-power single frequency pulses using multiple stage, large core phosphate fibers and preshaped pulses," *Appl. Opt.* **51**, pp. 531-534 (2012).
45. M. E. Fermann, M. Hofer, F. Haberl, S. P. Craig-ryan, "Femtosecond fiber laser", *Electron. Lett.* **26**, pp. 1737-1738 (1990).
46. M. E. Fermann, M. Hofer, F. Haberl, M. H. Ober and A. J. Schmidt, "Additive-pulse-compression mode locking of a neodymium fiber laser", *Opt. Lett.* **16**, pp. 244-246 (1991).

47. I. Duling, "All-fiber ring soliton laser mode locked with a nonlinear mirror", *Opt. Lett.* **16**, pp. 539-541 (1991).
48. A. G. Bulushev, E. M. Dianov, and O. G. Okhotnikov, "Passive mode locking of a laser with a nonlinear fiber reflector", *Opt. Lett.* **15**, pp. 968-970 (1990).
49. U. Keller, K. J. Weingarten, F. X. Kartner, D. Kopf, B. Braun, I. D. Jung, R. Fluck, C. Honninger, N. Matuschek and J. A. D. Au, "Semiconductor saturable absorber mirrors (SESAM's) for femtosecond to nanosecond pulse generation in solid-state lasers", *IEEE J. Sel. Top. Quantum. Electron.* **2**, pp. 435-453 (1996).
50. M. Zirngibl, L. Stulz, J. Stone, J. Hugi, D. DiGiovanni, and P. Hansen, "1.2 ps pulses from passively mode-locked laser diode pumped Er-doped fibre ring laser" *Electron. Lett.* **27**, pp. 1734-1735 (1991).
51. E. De Souza, C. Soccolich, W. Pleibel, R. Stolen, J. Simpson, and D. DiGiovanni, "Saturable absorber mode locked polarisation maintaining erbium-doped fibre laser" *Electron. Lett.* **29**, pp. 447-449 (1993).
52. M. Ober, M. Hofer, U. Keller, and T. Chiu, "Self-starting diode-pumped femtosecond Nd fibre laser", *Opt. Lett.* **18**, pp. 1532-1534 (1993).
53. S. Set, H. Yaguchi, Y. Tanaka, and M. Jablonski, "Laser mode locking using a saturable absorber incorporating carbon nanotubes", *J. Lightw. Technol.* **22**, pp.51-56 (2004).
54. Z. Sun, T. Hasan, F. Torrisi, D. Popa, G. Privitera, F. Wang, F. Bonaccorso, D. M. Basko and A. C. Ferrari, "Graphene mode-locked ultrafast laser", *ACS Nano* **4**, pp. 803-810 (2010).

55. S. Yamashita, Y. Inoue, S. Maruyama, Y. Murakami, H. Yaguchi, M. Jablonski, and S. Set, "Saturable absorbers incorporating carbon nanotubes directly synthesized onto substrates and fibers and their application to mode-locked fiber lasers", *Opt. Lett.* **29**, pp. 1581-1583 (2004).
56. K. Kieu and M. Mansuripur, "Femtosecond laser pulse generation with a fiber taper embedded in carbon nanotube/polymer composite", *Opt. Lett.* **32**, pp. 2242-2244 (2007).
57. Y. C. Chen, N. R. Raravikar, L. S. Schadler, P. M. Ajayan, Y. P. Zhao, T. M. Lu, G. C. Wang, X. C. Zhang, "Ultrafast optical switching properties of single-wall carbon nanotube polymer composites at  $1.55\mu\text{m}$ ", *Appl. Phys. Lett.* **81**, pp. 975-977 (2002).
58. M. Breusing, C. Ropers and T. Elsaesser, "Ultrafast carrier dynamics in graphite", *Phys. Rev. Lett.* **102**, 086809 (2009).
59. H. Choi, F. Borondics, D. A. Siegel, S. Y. Zhou and M. C. Martin, "Broadband electromagnetic response and ultrafast dynamics of few-layer epitaxial graphene", *Appl. Phys. Lett.* **94**, 172102 (2009).
60. Z. Sun, T. Hasan, A. C. Ferrari, "Ultrafast lasers mode-locked by nanotubes and graphene", *Phys. E.*, In press (2012).
61. F. W. Wise, A. Chong, and W. H. Renninger, "High-energy femtosecond fiber lasers based on pulse propagation at normal dispersion", *Laser & Photon. Rev.* **2**, pp. 58-73 (2008).
62. J. M. Dudley, C. Finot, D. J. Richardson and G. Millot, "Self-similarity in ultrafast nonlinear optics", *Nature Physic.* **3**, pp. 597-603 (2007).

63. K. Tamura, E. P. Ippen, H. A. Haus and L. E. Nelson, "77-fs pulse generation from a stretched-pulse mode-locked all-fiber ring laser", *Opt. Lett.* **18**, pp. 1080-1082 (1993).
64. A. Chong, J. Buckley, W. Renninger and F. Wise, "All-normal-dispersion femtosecond fiber laser", *Opt. Express* **14**, pp. 10095-10100 (2006).
65. W. H. Renninger, A. Chong and F. W. Wise, "Dissipative solitons in normal-dispersion fiber lasers", *Physic. Rev. A* **77**, 023814 (2008).
66. M. E. Fermann, A. Galvanauskas, G. Sucha, and D. Harter, "Fiber-lasers for ultrafast optics", *Appl. Phys. B* **65**, pp. 259-275 (1997).
67. M. E. Fermann and I. Hartl, "Ultrafast fiber laser technology", *IEEE J. Sel. Top. Quantum Electron.* **15**, pp. 191-206 (2009).
68. E. Stiles, "New developments in IPG fiber laser technology", in proceedings of the 5th International Workshop on Fiber Lasers (2009).
69. D. J. Richardson, J. Nilsson, and W. A. Clarkson, "High power fiber lasers: current status and future perspectives", *J. Opt. Soc. Am. B* **27**, pp. 63-92 (2010).
70. J. Limpert, A. Liem, M. Reich, T. Schreiber, S. Nolte, H. Zellmer, A. Tunnermann, J. Broeng, A. Petersson, and C. Jakobsen, "Low-nonlinearity single-transverse-mode ytterbium-doped photonic crystal fiber amplifier", *Opt. Express* **12**, pp. 1313-1319 (2004).
71. C. D. Brooks and F. D. Teodoro, "Multimegawatt peak-power, single-transverse-mode operation of a 100  $\mu\text{m}$  core diameter, Yb-doped rodlike photonic crystal fiber amplifier", *Appl. Phys. Lett.* **89**, 111119 (2006).

72. F. Roser, T. Eidam, J. Rothhardt, O. Schmidt, D. N. Schimpf, J. Limpert, and A. Tunnermann, "Millijoule pulse energy high repetition rate femtosecond fiber chirped-pulse amplification system", *Opt. Lett.* **32**, pp. 3495-3497 (2007).
73. F. Stutzki, F. Jansen, A. Liem, C. Jauregui, J. Limpert, and A. Tunnermann, "26 mJ, 130 W Q-switched fiber-laser system with near-diffraction-limited beam quality", *Opt. Lett.* **37**, pp. 1073-1075 (2012).
74. M. Leigh, W. Shi, J. Zong, Z. Yao, S. Jiang and N. Peyghambarian, "High peak power single frequency pulses using a short polarization maintaining phosphate glass fiber with a large core", *Appl. Phys. Lett.* **92**, pp. 181108-181111 (2008).
75. W. Shi, E. B. Petersen, Z. Yao, D. T. Nguyen, J. Zong, M. A. Stephen, A. Chavez-Pirson, and N. Peyghambarian, "Kilowatt-level stimulated-Brillouin-scattering-threshold monolithic transform-limited 100 ns pulsed fiber laser at 1530 nm", *Opt. Lett.* **35**, pp. 2418-2420 (2010).
76. W. Shi, M. A. Leigh, J. Zong, Z. Yao, D. T. Nguyen, A. Chavez-Pirson, and N. Peyghambarian, "High-power all-fiber-based narrow-linewidth single-mode fiber laser pulses in the C-Band and frequency conversion to THz generation", *IEEE J. Sel. Top. in Quantum.* **15**, pp. 377-384 (2009).
77. W. Shi, E. B. Petersen, D. T. Nguyen, Z. Yao, A. Chavez-Pirson, N. Peyghambarian, and J. Yu, "220  $\mu$ J monolithic single-frequency Q-switched fiber laser at 2  $\mu$ m by using highly Tm-doped germanate fibers", *Opt. Lett.* **36**, pp. 3575-3577 (2011).

78. Q. Fang, W. Shi, E. Petersen, K. Kieu, A. Chavez-Pirson, N. Peyghambarian, "Half-mJ all fiber based single frequency nanosecond pulsed fiber laser at 2  $\mu\text{m}$ ", IEEE Photon. Technol. Lett. **24**, pp. 353-355 (2012).
79. W. Shi, E. Petersen, Q. Fang, K. Kieu, A. Chavez-Pirson, N. Peyghambarian, and J. Yu, "mJ-level 2  $\mu\text{m}$  transform-limited nanosecond pulses based on highly Tm-doped germanate fibers", in Lasers, Sources, and Related Photonic Devices, OSA Technical Digest (CD) (Optical Society of America, 2012), Paper FTh4A. 1.
80. O. Svelto, "Principles of lasers", Fourth Edition, Springer-Verlag GmbH, 978-0306457487, Berlin, Heidelberg.
81. W. Koechner, "Solid-state laser engineering", Springer series in optical sciences **1**, pp. 748, Springer-Verlag GmbH, 978-0-387-29094-2, Berlin, Heidelberg.
82. L. F. Johnson, J. E. Geusic, L. G. V. Uitert, "Coherent oscillation from  $\text{Tm}^{3+}$ ,  $\text{Ho}^{3+}$ ,  $\text{Yb}^{3+}$  and  $\text{Er}^{3+}$  ions in yttrium aluminum garnet", Appl. Phys. Lett. **7**, pp. 127-129 (1965).
83. J. A. Caird, L. G. DeShazer, and J. Nella, "Characteristics of room-temperature 2.3  $\mu\text{m}$  laser emission from  $\text{Tm}^{3+}$  in YAG and  $\text{YAlO}_3$ ", IEEE J. Quantum Electron. **11**, pp. 874-881 (1975).
84. S. A. Payne, L. L. Chase, L. K. Smith, W. L. Kway, and W. F. Krupke, "Infrared cross-section measurements for crystals doped with  $\text{Er}^{3+}$ ,  $\text{Tm}^{3+}$ , and  $\text{Ho}^{3+}$ ", IEEE J. of Quantum Electron. **28**, pp. 2619-2630 (1992).

85. F. S. Ermeneux, Y. Sun, R. L. Cone, R. W. Equall, R. L. Hutchenson, and R. Moncorge, "Efficient cw 2  $\mu\text{m}$   $\text{Tm}^{3+}:\text{Y}_2\text{O}_3$  Laser", *Adv. Solid-state lasers* **26**, pp. 497-502 (1999).
86. L. Fornasiero, N. Berner, B. M. Dicks, E. Mix, V. Peters, K. Petermann, and G. Huber, "Broadly tunable laser emission from  $\text{Tm}:\text{Y}_2\text{O}_3$  and  $\text{Tm}:\text{Sc}_2\text{O}_3$  at 2  $\mu\text{m}$ ", *Conference on advanced solid-state lasers, OSA Technical Digest, paper WD5* (1999).
87. K. Scholle, E. Heumann, and G. Huber, "Single mode  $\text{Tm}$  and  $\text{Tm}, \text{Ho}:\text{LuAG}$  lasers for LIDAR applications", *Laser Phys. Lett.* **1**, pp. 1-5 (2004).
88. P. Koopmann, R. Peters, K. Petermann, and G. Huber, "Hocheffizienter Laserbetrieb von  $\text{Tm}^{3+}:\text{Lu}_2\text{O}_3$  bei einer Wellenlänge von 2  $\mu\text{m}$ ", *DPG Frühjahrstagung 2009 in Hamburg, Q 8.4* (2009).
89. M. Schellhorn, A. Hirt, and C. Kieleck, "Ho:YAG laser intracavity pumped by a diode-pumped  $\text{Tm}:\text{YLF}$ ", *Opt. Lett.* **28**, pp. 1933-1935 (2003).
90. M. Schellhorn, "Performance of a Ho: YAG thin-disc laser pumped by a diode-pumped 1.9  $\mu\text{m}$  thulium laser", *Appl. Phys. B* **85**, pp. 549-552 (2006).
91. C. Caneau, A. K. Srivastava, A. G. Dentai, J. L. Zyskind, and M. A. Pollack, "Room temperature GaIn AsSb/ AlGaAsSb DH injection lasers at 2.2  $\mu\text{m}$ ", *Electron. Lett.* **21**, pp. 815 (1985).
92. H. K. Choi, S. J. Eglash, "High-power multiple-quantum-well GaInAsSb/AlGaAsSb diode lasers emitting at 2.1  $\mu\text{m}$  with low threshold current density", *Appl. Phys. Lett.* **61**, pp. 1154-1156 (1992).
93. M. Rattunde, C. Mermelstein, J. Schmitz, R. Kiefer, W. Pletschen, M. Walther, and J. Wagner,

- "Comprehensive modeling of the electro-optical-thermal behaviour of (AlGaIn)(AsSb)-based 2.0  $\mu\text{m}$  diode lasers", *Appl. Phys. Lett.* **80**, pp. 4085-4087 (2002).
94. L. Shterengas, G. L. Belenky, A. Gourevitch, D. Donetsky, J. G. Kim, R. U. Martinelli, and D. Westerfeld, "High-power 2.3- $\mu\text{m}$  GaSb-based linear laser array", *IEEE Photon. Tech. Lett.* **16**, pp. 2218-2220 (2004).
95. D. C. Hanna, I. M. Jauncey, R. M. Percival, I. R. Perry, R. G. Smart, P. J. Suni, J. E. Townsend, and A. C. Tropper, "Continuous-wave oscillation of a monomode thulium-doped fibre laser", *Electron. Lett.* **24**, pp. 1222-1223 (1988).
96. D. C. Hanna, R. M. Percival, R. G. Smart, and A. C. Tropper, "Efficient and tunable operation of a Tm-doped fibre laser", *Opt. Communications* **75**, pp. 283-286 (1990).
97. D. C. Hanna, I. R. Perry, J. R. Lincoln, and J. E. Townsend, "A 1-Watt thulium-doped cw fibre laser operating at 2  $\mu\text{m}$ ", *Opt. Communications* **80**, pp. 52-56 (1990).
98. L. E. Nelson, E. P. Ippen, and H. A. Haus, "Broadly tunable sub-500 fs pulses from an additive-pulse mode-locked thulium-doped fiber ring laser", *Appl. Phys. Lett.* **67**, pp. 19-21 (1995).
99. R. C. Sharp, D. E. Spock, N. Pan, and J. Elliot, "190-fs passively mode-locked thulium fiber laser with a low threshold", *Opt. Lett.* **21**, pp. 881-883 (1996).
100. S. D. Jackson and T. King, "High-power diode cladding-pumped Tm-doped silica fiber laser", *Opt. Lett.* **23**, pp. 1462-1464 (1998).
101. R. A. Hayward, W. A. Clarkson, P. W. Turner, J. Nilsson, A. B. Grudinin, and D. C. Hanna, "Efficient cladding-pumped Tm-doped silica fibre laser with high power single mode output at 2  $\mu\text{m}$ ", *Electron. Lett.* **36**, pp. 711-712 (2000).

102. T. Becker, R. Clausen, G. Huber, E. W. Duczynski, and P. Mitzscherich, "Spectroscopic and laser properties of thulium doped YAG at 2  $\mu\text{m}$ ", in Optical Society of America 150-153 (1989).
103. S. D. Jackson, "Cross relaxation and energy transfer upconversion processes relevant to the functioning of 2  $\mu\text{m}$   $\text{Tm}^{3+}$ -doped silica fibre lasers", *Opt. Communications* **230**, pp. 197-203 (2004).
104. S. D. Jackson and S. Mossman, "Efficiency dependence on the Tm and Al concentrations for Tm-doped silica double-clad fiber lasers", *Appl. Opt.* **42**, pp. (2003).
105. T. Ehrenreich, R. Leveille, I. Majid, K. Tankala, G. Rines, and P. F. Moulton, "1-kW, all-glass Tm: fiber laser", in *Fiber Laser VII: Technology, Systems and Applications* (2010) (Session 16: Late breaking news).
106. D. Creedon, P. A. Budni, and P. A. Ketteridge, "Pulsed Tm-doped fiber lasers for mid-IR frequency conversion", In *SPIE Photonics West* (2009).
107. W. Shi, E. Petersen, Q. Fang, K. Kieu, A. Chavez-Pirson, and N. Peyghambarian, "Efficient parametric THz generation pumped by monolithic pulsed fiber lasers at  $\sim 2 \mu\text{m}$  in MOPA configuration", *SPIE Photonics West* (2012).
108. D. H. Auston and P. R. Smith, "Generation and detection of millimeter waves by picosecond photonconductivity", *Appl. Phys. Lett.* **43**, pp. 631-633 (1983).
109. B. Ferguson, S. Wang, D. Abbott, and X. C. Zhang, "Powder detection with THz imaging", *Proc. SPIE Terahertz for Military and Security Applications*, **5070**, pp. 7-16 (2003).

110. C. Zandonella, "T-ray specs", *Nature* **424**, pp. 721-722 (2003).
111. M. Walther, B. M. Fischer, and P. U. Jepsen, "Noncovalent intermolecular forces in polycrystalline and amorphous saccharides in the far infrared", *Chem. Phys.* **288**, pp. 261-268 (2003).
112. L. B. Braly, K. Liu, M. G. Brown, F. N. Keutsch, R. S. Fellers, and R. J. Saykally, "Terahertz laser spectroscopy of the water dimer intermolecular vibrations. II. (H<sub>2</sub>O)<sub>2</sub>", *J. Chem. Phys.* **112**, pp. 10314-10326 (2000).
113. B. M. Fischer, M. Walther, and P. U. Jepsen, "Far-infrared vibrational modes of DNA components studied by terahertz time-domain spectroscopy", *Phys. Med. Biol* **47**, pp. 3807-3814 (2002).
114. H. Harde, R. Cheville, and D. Grischkowsky, "Terahertz studies of collision-broadened rotational lines", *J. Phys. Chem. A* 101, pp. 3646-3660 (1997).
115. D. M. Mittleman, R. H. Jacobsen, R. Neelamani, R. G. Baraniuk, and M. C. Nuss, "Gas sensing using terahertz time-domain spectroscopy", *Appl. Phys. B: Lasers Opt.* 67, pp. 379-390 (1998).
116. P. F. Bernath, *Spectra of Atoms and Molecules*, 2nd ed. Oxford, U. K.: Oxford University Press (2005).
117. P. Y. Han, G. C. Cho, and X. C. Zhang, "Time-domain transillumination of biological tissues with terahertz pulses", *Opt. Lett.* **25**, pp. 242-244 (2000).
118. E. Berry, "Risk perception and safety issues", *J. Biol. Phys.* **29**, pp. 263-267 (2003).
119. Hitchcock RT., "Radio-frequency and microwave radiation", 3rd Edition, Fairfax, VA: AIHA Press (2004).

120. G. M. H. Knippels, X. Yan, A. M. Macleod, W. A. Gillespie, M. Yasumoto, D. Oepts, and A. F. G. Van der Meer, "Generation and complete electric-field characterization of intense ultrashort tunable far-infrared laser pulses", *Phys. Rev. Lett.* **83**, pp. 1578-1581 (1999).
121. S. Park, A. M. Weiner, M. R. Melloch, C. W. Siders, J. L. W. Siders, and A. J. Taylor, "High-power narrow-band terahertz generation using large-aperture photoconductors", *IEEE J. Quantum Electron.* **35**, pp. 1257-1268 (1999).
122. B. S. Williams, "Terahertz quantum-cascade lasers", *Nature Photonics* **1**, pp. 517-525 (2007).
123. A. Rice, Y. Jin, X. F. Ma, X. C. Zhang, D. Bliss, J. Larkin, and M. Alexander, "Terahertz optical rectification from (110) zincblende crystals", *Appl. Phys. Lett.* **64**, pp. 1324-1326 (1994).
124. W. Shi, Y. J. Ding, N. Fernelius, and K. Vodopyanov, "Efficient, tunable, and coherent 0.18-5.27-THz source based on GaSe crystal", *Opt. Lett.* **27**, pp. 1454-1456 (2002).
125. J. Kiessling, F. Fuchs, K. Buse, and I. Breunig, "Pump-enhanced optical parametric oscillator generating continuous wave tunable terahertz radiation", *Opt. Lett.* **36**, pp. 4374-4376 (2011).
126. A. Liem, J. Limpert, H. Zellmer, and A. Tunnermann, "100 W single-frequency master-oscillator fiber power amplifier," *Opt. Lett.* **28**, pp. 1537-1539 (2003).
127. Y. Jeong, J. Nilsson, J. K. Sahu, D. B. S. Soh, C. Alegria, P. Dupriez, C. A. Codemard, D. N. Payne, R. Horley, L. M. B. Hickey, L. Wanzcyk, C. E. Chryssou,

- J. A. Alvarez-Chavez, and P. W. Turner, "Single-frequency, single-mode, plane-polarized ytterbium-doped fiber master oscillator power amplifier source with 264 W of ourput power," *Opt. Lett.* **30**, pp. 459-462 (2005).
128. Y. Jeong, J. Nilsson, J. K. Sahu, D. N. Payne, R. Horley, L. M. B. Hickey, and P. W. Turner "Power scaling of single-frequency ytterbium-doped fiber master-oscillator power-amplifier sources up to 500 W," *IEEE J. Sel. Top. Quantum Electron.* **13**, pp. 546-551 (2007).
129. G. D. Goodno, L. D. Book, and J. E. Rothenberg, "Low-phase-noise, single-frequency, single-mode 608 W thulium fiber amplifier," *Opt. Lett.* **34**, pp. 1204-1206 (2009).
130. L. Pearson, J. W. Kim, Z. Zhang, M. Ibsen, J. K. Sahu, and W. A. Clarkson, "High-power linearly-polarized single-frequency thulium-doped fiber master-oscillator power-amplifier," *Opt. Express.* **18**, pp. 1607-1212 (2010).
131. C. D. Brooks and F. D. Teodoro, "1-mJ energy, 1-MW peak-power, 10-W average power, spectrally narrow, diffraction-limited pulses from a photonic-crystal fiber amplifier" *Opt. Express.* **13**, pp. 8999-9002 (2005).
132. A. Dergachev, D. Armstrong, A. Smith, T. Drake, and M. Dubois, "3.4  $\mu\text{m}$  ZGP RISTRA nanosecond optical parametric oscillator pumped by a 2.05- $\mu\text{m}$  Ho:YLF MOPA system" *Opt. Express.* **15**, pp. 14404-14413 (2007).
133. [http://www.ipgphotonics.com/apps\\_materials\\_multi\\_yls.htm](http://www.ipgphotonics.com/apps_materials_multi_yls.htm)

134. S. D. Jackson, "The spectroscopic and energy transfer characteristics of rare earth ions used for silicate glass fibre lasers operating in the shortwave infrared", *Laser Photonics Rev.* **3**, pp. 466-482 (2009).
135. G. Frith, D. G. Lancaster, and S. D. Jackson, "85 W Tm<sup>3+</sup>-doped silica fiber laser", *Electron. Lett.* **41**, pp. 687-688 (2005).
136. G. Frith, B. samson, A. Carter, J. Farroni, and K. Tankala, "High power (110), high efficiency (55%) FBG fibre laser operating at 2  $\mu\text{m}$ ", *Proc. SPIE* **6453**, 64532B (2007).
137. T. S. McComb, R. A. Sims, C. C. C. Willis, P. Kadwani, V. Sudesh, L. Shah, and M. Richardson, "High-power widely tunable thulium fiber lasers", *Appl. Opt.* **49**, pp. 6236-6242 (2010).
138. M. Meleshkevich, N. Platonov, D. Gapontsev, A. Drozhzhin, V. Sergeev, and V. Gapontsev, "415 W single-mode CW thulium fiber laser in all-fiber format", *CLEOE-IQEC, Munich* (2007).
139. G. D. Goodno, L. Book, and J. E. Rothenberg, presented at the 11th Annual DE Symposium, Honolulu, Hawaii, Nov. 18-21 (2008).
140. J. Wu, Z. Yao, J. Zong, and S. Jiang, "Highly efficient high-power thulium-doped germanate glass fiber laser", *Opt. Lett.* **32**, pp. 638-640 (2007).
141. P. S. Golding, S. D. Jackson, P. K. Tsai, B. C. Dickinson, and T. A. King, "Efficient high power operation of a Tm-doped silica fiber laser pumped at 1.319  $\mu\text{m}$ ", *Opt. Communications* **175**, pp. 179-183 (2000).

142. T. Forster, "Zwischenmolekulare energiewanderung and fluoreszenz (Intermolecular energytransfer and fluorescence)", *Annalen der Physik* **2**, pp. 55-77 (1948).
143. A. M. Tkachuk, I. K. Razumova, M. F. Joubert, R. Moncorge, D. I. Mironov, and A. A. Nikitichev, "Self-quenching of luminescence in YLF:  $Tm^{3+}$  crystals: I. Microscopic parameters and rates of energy transfer", *Solid-state spectroscopy* **85**, pp. 885-892 (1998).
144. J. Wu, "Thulium doped microsphere laser and fiber laser," Dissertation, University of Arizona, (2005).
145. T. Furukawa, K. E. Fox, and W. B. White, "Raman spectroscopic investigation of the structure of silicate glasses. III. Raman intensities and structural units in sodium silicate glasses", *J. Chem. Phys.* **75**, pp. 3226-3237 (1981).
146. F. Gan, "Optical properties of fluoride glasses: a review", *J. of Non-Cryst. Solids*, **184**, pp. 9-20 (1995).
147. R. Reisfeld and Y. Eckstein, "Optical spectra of erbium and thulium in germanate glasses", *J. of Non-cryst. Solids*, pp. 357-376 (1973).
148. D. N. Schimpf, C. Ruchert, D. Nodop, J. Limpert, A. Tunnermann, F. Salin, "Compensation of pulse-distortion in saturated laser amplifiers," *Opt. Express* **16**, pp. 17637-17646 (2008).
149. G. P. Agrawal, *Nonlinear Fiber Optics*, Third Edition, (Academic, 2001).

150. B. C. Stuart, M. D. Feit, A. M. Rubenchik, B. W. Shore, and M. D. Perry, "Laser induced damage in dielectrics with nanosecond to subpicosecond pulses", *Phys. Rev. Lett.* **74**, pp. 2248-2251 (1995).
151. A. E. Siegman, *Lasers*, First Edition, (Academic, 1986).
152. M. Eichhorn, "Numerical modeling of Tm-doped double-clad fluoride fiber amplifier", *IEEE J. Quantum Electron.* **41**, pp. 1574-1581 (2005).
153. K. L. Vodopyanov, "Optical THz-wave generation with periodically-inverted GaAs", *Laser & Photon. Rev.* **2**, pp. 11-25 (2008).
154. K. L. Vodopyanov, "Optical generation of narrow-band terahertz packets in periodically-inverted electro-optic crystals: conversion efficiency and optimal laser pulse format", *Opt. Express* **14**, pp. 2263-2276 (2006).
155. R. H. Stolen, "Far-infrared absorption in high resistivity GaAs", *Appl. Phys. Lett.* **15**, pp. 74-75 (1969)
156. J. S. Blakemore, "Semiconducting and other major properties of gallium arsenide," *J. Appl. Phys.* **53**, pp. 132-181 (1982).
157. T. Skauli, K. L. Vodopyanov, T. J. Pinguet, A. Schober, O. Levi, L. A. Eyres, M. M. Fejer, and J. S. Harris, "Measurement of the nonlinear coefficient of orientation-patterned GaAs and demonstration of highly efficient second-harmonic generation", *Opt. Lett.* **27**, pp. 628-630 (2002).
158. H. Qi, Q. Wang, X. Zhang, Z. Liu, S. Zhang, J. Chang, W. Xia, G. Lin, "Theoretical and experimental study of laser induced damage on GaAs by nanosecond pulsed irradiation", *optics and lasers in engineering* **49**, pp. 285-291 (2011).

159. H. Kogelnik, T. Li, "Laser beams and resonators", *Appl. Opt.* **5**, pp. 1550-1567 (1966).
160. R. Tanaka, T. Matsuzawa, H. Yokota, T. Suzuki, Y. Fujii, A. Mio, M. Katsuragawa, "Stable confinement of nanosecond laser pulse in an enhancement cavity", *Opt. Express* **16**, pp. 18667-18674 (2009)
161. E. B. Petersen, W. Shi, D. T. Nguyen, Z. Yao, J. Zong, A. Chavez-Pirson, and N. Peyghambarian, "Enhanced terahertz source based on external cavity difference-frequency generation using monolithic single-frequency pulsed fiber lasers", *Opt. Lett.* **35**, pp. 2170-2172 (2010).
162. S. D. Jackson, A. Sabella, A. Hemming, S. Bennetts, and D. G. Lancaster, "High power 83 W holmium-doped silica fiber laser operating with high beam quality", *Opt. Lett.* **32**, pp. 241-243 (2007).
163. M. Eichhorn, and S. D. Jackson, "High pulse energy actively Q-switched  $Tm^{3+}$ -doped silica 2  $\mu m$  fiber laser pumped at 792 nm", *Opt. Lett.* **32**, pp. 2780-2782 (2007).
164. L. E. Nelson, E. P. Ippen and H. A. Haus, "Broadly tunable sub-500 fs pulses from an additive-pulse mode-locked thulium-doped fiber ring laser", *Appl. Phys. Lett.* **67**, pp. 19-21 (1995).
165. R. C. Sharp, D. E. Spock, N. Pan, and J. Elliot, "190 fs passively mode-locked thulium fiber laser with a low threshold", *Opt. Lett.* **21**, pp. 881-883 (1996).

166. S. Kivisto, T. Hakulinen, M. Guina, and O. G. Okhotnikov, "Tunable Raman soliton source using mode-locked Tm-Ho fiber laser," *IEEE Photon. Technol. Lett.*, **19**, pp. 934-936 (2007).
167. M. Engelbrecht, F. Haxsen, A. Ruehl, D. Wandt, and D. Kracht, "Ultrafast thulium-doped fiber oscillator with pulse energy of 4.3 nJ", *Opt. Lett.* **33**, pp. 690-692 (2008).
168. M. Solodyankin, E. Obraztsova, A. Lobach, A. Chernov, A. Tausenev, V. Konov, and E. Dianov, "1.93  $\mu\text{m}$  mode-locked thulium fiber laser with a carbon nanotube absorber," *Opt. Lett.* **33**, pp. 1336-1338 (2008).
169. K. Kieu and F. W. Wise, "Soliton Thulium-Doped Fiber Laser With Carbon Nanotube Saturable Absorber," *IEEE Photon. Technol. Lett.* **21**, pp. 128-130 (2009).
170. Q. Wang, J. Geng, T. Luo, and S. Jiang, "Mode-locked 2  $\mu\text{m}$  laser with highly thulium-doped silicate fiber," *Opt. Lett.* **34**, pp. 3616-3618 (2009).
171. F. Wang, A. G. Rozhin, V. Scardaci, Z. Sun, F. Hennrich, I. H. White, W. I. Milne and A. C. Ferrari, "Wideband-tunable, nanotube mode-locked, fibre laser", *Nature Nanotechnology* **3**, pp. 738-742 (2008).
172. J. D. Love, W. M. Henry, W. J. Stewart, R. J. Black, S. Lacroix, and F. Gonthier, "Tapered single-mode fibres and devices. Part 1 : Adiabaticity criteria," *IEEE Proceedings-J.* **138**, 343 (1991).
173. K. Kieu and M. Mansuripur, "Tuning of fiber lasers by use of a single-mode biconic fiber taper," *Opt. Lett.* **31**, pp. 2435-2437 (2006).